

A Thesis Submitted for the Degree of PhD at the University of Warwick

Permanent WRAP URL:

<http://wrap.warwick.ac.uk/165367>

Copyright and reuse:

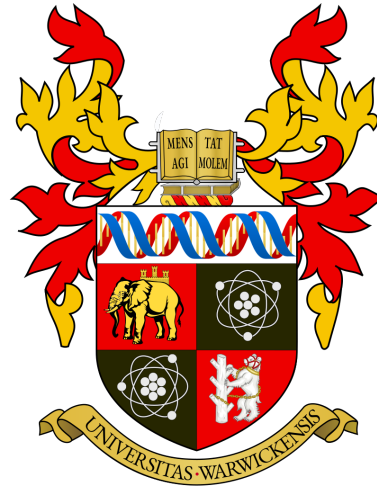
This thesis is made available online and is protected by original copyright.

Please scroll down to view the document itself.

Please refer to the repository record for this item for information to help you to cite it.

Our policy information is available from the repository home page.

For more information, please contact the WRAP Team at: wrap@warwick.ac.uk



**Employing Density Functional Theory to Model the
Thermodynamic Behaviour and Diffusion of
Nitrogen in the Iron-Nitrogen-Vacancy System**

by

Aurash Karimi

Thesis

Submitted to the University of Warwick

for the degree of

Doctor of Philosophy in Engineering

Warwick Manufacturing Group

January 2021

THE UNIVERSITY OF
WARWICK

Contents

List of Figures	iv
Acknowledgments	xi
Declarations	xii
Abstract	xiii
Chapter 1 Introduction	1
1.1 Thesis Outline	1
1.2 Motivation and Background	2
1.2.1 Allotropes of Iron	2
1.2.2 Heat Treatment of Iron Alloys	3
1.2.3 Nitriding	4
1.2.4 Objective	7
Chapter 2 Literature Review	8
2.1 Nitriding Models	8
2.2 Experimental Data	9
2.3 First Principles Modelling	10
Chapter 3 Review of Computational Methods	12
3.1 Density Functional Theory (DFT)	12
3.1.1 Theoretical Origins	12
3.1.2 Limitations of DFT	14
3.1.3 Output	15
3.1.4 DFT Models of Iron	16
3.1.5 Plane-Wave DFT	17
3.1.6 Software	21
3.1.7 Error Cancelling	22

3.1.8	Structural Relaxation	22
3.2	Thermodynamic Modelling	23
3.2.1	Vibrational Contributions	24
3.2.2	Volume	24
3.2.3	Configurational Entropy	25
3.2.4	Gibbs Free Energy	26
3.2.5	Nitrogen Reference State	28
3.3	Diffusion Modelling	29
3.3.1	Elementary Diffusion Step	29
3.3.2	Nudged Elastic Band	30
3.3.3	Kinetic Monte Carlo	32
3.3.4	Layer Growth Model	33
Chapter 4 Thermodynamic Model		35
4.1	Authors	35
4.2	Summary	35
4.3	Novel Contributions	36
4.3.1	Nitrogen-Vacancy Interactions	36
4.3.2	Accuracy of Results	37
4.3.3	Repulsion energy	37
4.3.4	Presentation	37
4.4	Methods	38
4.4.1	Atomic Scale Modelling	38
4.4.2	Thermodynamic Model	44
4.5	Results and Discussion	47
4.5.1	Atomic Scale Results	47
4.5.2	Thermodynamic Implications	51
4.6	Conclusion	57
Chapter 5 Diffusion Model		59
5.1	Authors	59
5.2	Summary	59
5.3	Novel Contributions	60
5.4	Methods	61
5.4.1	First Principles Calculations	62
5.4.2	Diffusion Model	64
5.5	Results and Discussion	67
5.5.1	First Principles Results	67

5.5.2	Diffusion Model Results	71
5.5.3	Using the Supplementary Spreadsheet	82
5.5.4	FCC 1 → 1 jump	83
5.5.5	Piecewise Log-Linear Interpolation	87
5.5.6	Simulated Diffusion Data Plots	88
5.6	Conclusion	88
Chapter 6 Nitrogen Concentration Profile		90
6.1	Methodology	91
6.2	Results and Discussion	91
Chapter 7 Conclusions and Future Work		95
7.1	Thermodynamics	95
7.1.1	Nitrogen-Vacancy Equilibrium	95
7.1.2	Modelling Crystal Imperfections with Vacancies	96
7.2	Diffusion	99
7.2.1	Thermal Expansion	99
7.2.2	Impact of Vacancies	99
7.3	Future Work	100
7.3.1	DFT Accuracy	100
7.3.2	Experimental Verification of Vacancy-Rich Model	101
7.3.3	Improvements to the Diffusion Model	101
7.3.4	Extension to Other Interstitial elements	102

List of Figures

1.1	Body-centered cubic (left) and face-centered cubic (right) crystal structure with lattice parameter a . Figure has been modified from [1].	2
1.2	Top: Micrograph showing the composition of nitride layers in iron after nitriding heat treatment (source [2]). Bottom: Stability of iron-nitride phases under a range of nitriding conditions, the right hand side diagram is commonly referred to as a Lehrer diagram (source [3]).	4
1.3	Bonding diagram of nitrogen molecules. Dots indicate lone pairs of electrons.	5
3.1	Examples of supercells with BCC (top) and FCC (bottom) crystal structures. Dashed lines indicate the boundaries of unit cells.	19
3.2	Relaxed BCC (left) and FCC (right) supercells containing a single nitrogen atom in an octahedral void. The nitrogen atom has caused local distortions in both cases which break the intrinsic symmetry of the supercells.	23
3.3	Relationship of configurational entropy with $\frac{k}{n}$, where k is the number of mobile particles in a system, and n is the number of possible candidate positions available for the particles.	26
3.4	The map of potential energy change as a nitrogen atom traverse the space between two adjacent octahedral positions (green circles) in an FCC iron lattice. The minimum energy path for the nitrogen atom is indicated by the dashed black line, and the transition state is marked by an orange circle. The contour surface ranges from the stable low energy nitrogen positions (blue) to unstable high energy positions (red).	30

3.5	Examples of nudged elastic band (NEB) calculations. The left image represents standard NEB, and the right image represents the climbing image variant [4]. ΔE denotes the energy barrier for diffusion. The orange dots are data points calculated from NEB, and the black curves are fitted to the data.	32
4.1	A two-dimensional cross section showing octahedral sites for nitrogen atoms (small circles) within α -Fe (BCC, left) and γ -Fe (FCC, right) lattices of iron atoms (large circles) in the proximity of a vacancy (yellow square). Green arrows represent the jumping directions for nitrogen atoms between sites, which are considered to happen with equal frequency if both ends of the arrow point to the same type of site (shade of blue). The small circles with the darkest shade of blue are the sites which are most influenced by the vacancy, whereas the lightest shade indicates sites which are far enough from the vacancy so that the energy barriers between them are not effected. Figure is reproduced from Karimi and Auinger [5] (2020).	42
4.2	The fraction of vacancies in idealised α (left) and γ (right) iron when nitrogen-vacancy complexes as well as lone vacancies are considered. Note that the upper limit of vacancies reached under these conditions is lower in the γ case and this is reflected in the colour bar values. Figure is reproduced from Karimi and Auinger [5] (2020).	52
4.3	Solubility of nitrogen in iron at nitrogen partial pressure $p_{N_2} = 1$ atm. Experimental values are represented by blue circles [6] and orange circles [7]. In the left image, the solubility of nitrogen in ideal crystals as calculated by DFT is depicted for α (red line) and γ (green line) iron, and DFT calculation uncertainty is represent by the grey shaded area. Excess vacancies, represented by red and green contours, are added to α and γ respectively in the right image which increases the solubility of nitrogen above the value obtained from an ideal crystal calculation. Figure is reproduced from Karimi and Auinger [5] (2020).	53

- 4.4 The calculated α - γ phase boundary in the iron-nitrogen system from first principles (blue line) and the calculation uncertainty range (grey area). Cyan dots show the same boundary calculated with estimated corrections for nitrogen repulsion. The black line is the corresponding boundary line from experimental data (sourced from the FSstel database accessed via FactSage [8]). Although in reality there are more stable iron-nitride allotropes in certain regions for the conditions featured, they are not included in this figure for conciseness. Figure is reproduced from Karimi and Auinger [5] (2020). 55
- 4.5 The concentration of excess lone vacancies required in nitrogen-containing α (red contours) and γ (green contours) iron, to shift the phase boundary and expand their respective phase within the Lehrer diagram. The edges of the contour surfaces (where they meet) represent the α - γ phase boundary for a theoretical ideal crystal, so they almost correspond (see figure 4.4) to the experimentally derived values for this boundary. All experimental data (Black lines) is sourced from the FSstel database accessed via FactSage [8]. This study was limited to the α and γ phases, but the ϵ (Fe_2N) and γ' (Fe_4N) regions are included to portray the results of this work in the wider context. Note that the colorbars between both graphs have different ranges of vacancy concentrations. Figure is reproduced from Karimi and Auinger [5] (2020). 56
- 4.6 The change of the α - γ iron phase transition temperature (ΔT) in the presence of nitrogen and an excess vacancy concentration in both phases. Each surface represents an evenly spaced (with respect to $\log_{10}r_{\text{N}}$) point on the phase boundary which is calculated for ideal crystals (see figure 4.4), which are denoted on the vertical axes. The shift is made hotter ($\Delta T > 0 \text{ }^\circ\text{C}$) by excess vacancies in α -Fe and colder ($\Delta T < 0 \text{ }^\circ\text{C}$) for γ vacancies accordingly. For $\Delta T < -250 \text{ }^\circ\text{C}$ or $\Delta T > 250 \text{ }^\circ\text{C}$ the surface is left uncoloured for better visibility. Figure is reproduced from Karimi and Auinger [5] (2020). 57

5.1	Jump paths (black arrows) and interstitial positions (blue spheres) for a nitrogen atom in nearest neighbour positions around a vacancy (grey cube) in BCC and FCC lattices. A numbering of i indicates that an interstitial position is an i 'th nearest neighbour to the vacancy. $E_{v(i \rightarrow j)}^N$ denotes the energy barrier for nitrogen to jump from an i position to a j position. Figure is reproduced from Karimi and Auinger [9] (2021).	65
5.2	Results from Nudged Elastic Band (NEB) calculations in BCC (left) and FCC (right) Fe supercells. Each filled square is an NEB data point. Top: The energy of an interstitial nitrogen atom in ferromagnetic BCC iron (left) and non-magnetic FCC iron (right) relative to a nitrogen atom in the gas state, as it transitions between octahedral positions (blue shaded circles) in the proximity of a vacancy (filled yellow square in lattice diagrams). The process used to obtain the reference energy of nitrogen gas is detailed in Karimi and Auinger [5]. Bottom: The energy of an iron atom in BCC (left) and FCC (right) Fe, as it transitions to a vacant nearest neighbour lattice position. Figure is reproduced from Karimi and Auinger [9] (2021).	69
5.3	The calculated energy barrier for nitrogen diffusion in α iron (red curve, left) and γ iron (green line, right) when the lattice parameter is varied from its equilibrium value at absolute zero temperature. Filled squares and circles are data points calculated from first principles for ferromagnetic BCC iron and non-magnetic FCC iron respectively.	70
5.4	Traces of the diffusion coefficient of interstitial nitrogen atoms from Kinetic Monte Carlo trajectories in ferromagnetic BCC iron (red) and non-magnetic FCC iron (green) supercells. The BCC supercell contained a nitrogen concentration of 0.1 at.%, and the FCC supercell contained a nitrogen concentration of 1 at.%. The supercell for each trajectory had a fixed concentration of vacant lattice positions as labelled. Figure is reproduced from Karimi and Auinger [9] (2021).	72

5.5	Nitrogen diffusion data calculated from first principles in ferromagnetic BCC iron (red lines) and non-magnetic FCC iron (green lines). Solid lines indicate that volume and vibrational contributions are incorporated into the calculation. Dashed lines indicate only volume contributions are included, while the dotted lines indicate both contributions are omitted. Experimental diffusion data for α iron [10] (red squares) and γ iron [11] (green circles) are included for comparison. Figure is reproduced from Karimi and Auinger [9] (2021).	74
5.6	The interstitial diffusion coefficient D of nitrogen in α iron (red, top) and γ iron (green, bottom) calculated with nitrogen concentrations $c_N = 0.1$ at.% and $c_N = 1.0$ at.% respectively. Experimental data points for comparison are from [10] (red squares) and [11] (green circles). The diffusion coefficients calculated in absence of vacancies are given by red and green solid lines. The contour surfaces indicate the shift in diffusion coefficient at varied vacancy concentrations. The dashed black curves on the contour surfaces indicate where the nitrogen and vacancy concentrations are equal. Figure is reproduced from Karimi and Auinger [9] (2021).	77
5.7	The contour surface which portrays the shift in the diffusion coefficient of nitrogen in α iron (red, top) and γ iron (green, bottom) at varied vacancy concentrations and temperatures. The nitrogen concentration is fixed at 0.1 at.% and 1 at.% for α and γ respectively. red and green lines on the surfaces trace the points where the diffusion coefficient has decreased (compared to vacancy-free diffusion) 2, 10 and 100-fold due to vacancies. Figure is reproduced from Karimi and Auinger [9] (2021).	78

5.8	The diffusion coefficient of nitrogen in vacancy-containing α iron (red, top) and γ iron (green, bottom). The figures on the left hand side indicate the shift in the diffusion coefficient at a range of values of the expression $\log_{10} \left(\frac{c_v^2}{100(c_v + c_N)} \right)$, where c_N is the nitrogen concentration and c_v is the vacancy concentration. The left hand side figures are calculated with interstitial nitrogen concentrations of $c_N = 0.1$ at.% and $c_N = 1$ at.% for α iron and γ iron respectively. The figures on the right hand side shows the difference between polynomial fits of the diffusion coefficient corresponding to two different nitrogen concentrations. The areas where the difference between the fits is outside of the colour bar range of the contours is coloured in black. Figure is reproduced from Karimi and Auinger [9] (2021).	81
5.9	The energy of an interstitial nitrogen atom in non-magnetic FCC iron relative to a nitrogen atom in the gas state, as it transitions between symmetrical octahedral positions which are first nearest neighbours to a vacancy. The process used to obtain the reference energy of nitrogen gas is detailed in Karimi and Auinger [5]. Figure is reproduced from Karimi and Auinger [9] (2021).	84
5.10	Traces of the mean squared displacement of nitrogen atoms over time t in non-magnetic FCC iron with a vacancy concentration of 10 at.% and interstitial nitrogen concentration of 1 at.%. Solid lines represent trajectories where first nearest neighbour jumps for nitrogen around a vacancy are included in Kinetic Monte Carlo (KMC) simulations, and dashed lines represent trajectories where such jumps are omitted. Each of the six traces shown comprise of 250000 KMC steps. The dotted lines show the theoretical contribution to the mean squared displacement from repeated first nearest neighbour jumps of nitrogen around a vacancy at equilibrium. Figure is reproduced from Karimi and Auinger [9] (2021).	85
5.11	Maximum error in the calculated diffusion coefficient of nitrogen in non-magnetic FCC iron, if first nearest neighbour jumps for nitrogen around a vacancy are omitted from Kinetic Monte Carlo simulations. The vacancy concentration of iron is denoted by c_v . The area under the dashed line shows where the error is smaller than the chosen convergence criteria for KMC simulations. Figure is reproduced from Karimi and Auinger [9] (2021).	87

5.12	The diffusion coefficient of nitrogen in α iron (red, top) and γ iron (green, bottom) with interstitial nitrogen concentrations of 0.1 at.% and 1 at.% respectively. The vacancy concentration of the iron is denoted by c_v . The data points represent converged data from Kinetic Monte Carlo simulations as detailed in the text. The grey shading indicates that the data points are extrapolated using a linear fit to the two closest calculated points. Figure is reproduced from Karimi and Auinger [9] (2021).	88
6.1	Diffusion of nitrogen into a semi-infinite bar of α -iron for 10 hours. The nitrogen concentration at the source where $x = 0$ is fixed at 0.1 at.% throughout time. The solid lines indicate that the iron is vacancy-free, whilst the dashed lines indicate a vacancy concentration of 0.1 at.%. The figures correspond to diffusion temperatures of 400°C and 600°C as labelled.	92
6.2	Diffusion of nitrogen into a semi-infinite bar of γ -iron for 100 hours. The nitrogen concentration at the source where $x = 0$ is fixed at 0.1 at.% throughout time. The solid lines indicate that the iron is vacancy-free, whilst the dashed lines indicate a vacancy concentration of 0.1 at.%. The diffusion temperature is fixed at 600°C.	93

Acknowledgments

I would like to thank:

My supervisor Michael Auinger, I could not ask for someone more kind and patient as a supervisor and mentor. Thank you for all the interesting debates and always challenging me to do better. It's been a pleasure working with you.

The staff who supported the High Performance Computing facilities at Warwick, for being so reliable, helping me get my software running, and fixing things when they broke. You were invaluable to the success of the project.

All of my coworkers in the Steels group at Warwick, for providing a thought-provoking and friendly environment to work in, its been great being a part of it.

My parents Shahriar Karimi and Shohreh Karimi, and my sister Shayda Karimi. You have always supported me and believed in me in whatever path I chose. I'm very lucky to have you.

Declarations

This thesis by is submitted to the University of Warwick in support of my (Aurash Karimi) application for the degree of Doctor of Philosophy in Engineering. It has been composed by myself and has not been submitted in any previous application for any degree. The work presented was carried out solely by me with the help and guidance of my supervisor (Michael Auinger). The novel work in this thesis is presented in journal paper format and prefacing each paper there is a summary of my contribution to the work.

Abstract

This project adopts density functional theory (DFT) in a multiscale modelling approach to study thermodynamics and diffusion in the iron-nitrogen-vacancy system. This allows for more robust models of nitriding, which is a common heat treatment process used in the global steel industry. Current models for nitriding tend to depend heavily on empirical data, and while this is satisfactory for many purposes, it does not allow for effective modelling when the empirical data is not available or difficult to obtain experimentally. DFT calculations, although they require considerable computational effort, are ideal for such scenarios. Through DFT, the formation of nitrogen-vacancy complexes are investigated in conditions that represent the nitriding process, both at thermodynamic equilibrium and metastable states where vacancies are in excess. The latter of which was found to be more reflective of real manufacturing conditions, under which the iron crystal structure is not uniform and defect-free. Further, this work quantifies the diffusion behaviour of nitrogen in vacancy-rich conditions. This has far-reaching implications, as precise models for diffusion are required to design the treatment so that a quality result is achieved. For instance, there should not be sharp changes in nitrogen content throughout the metal, or it loses a significant amount of load bearing ability.

Chapter 1

Introduction

This chapter is comprised of two sections. The first section outlines the structure of the thesis. The second section gives an overview of the context and motivation for the research which was carried out during the PhD, followed by the research objectives.

1.1 Thesis Outline

This thesis consists of three introductory chapters, three result chapters and a conclusion. The first chapter is a broad overview of the project, while the second and third discuss the existing literature and computational methods, respectively. The fourth and fifth chapters consist primarily of extracts from two published journal papers which are principally authored by the PhD candidate. The papers are connected in terms of methodology, but each are used for predicting different aspects of the metallurgical processes of interest. In their respective chapters, each paper is introduced and discussed in the context of the relevant surrounding literature and the contribution of each author is briefly described. The sixth chapter consists of an applied example which employs the models developed in chapters four and five.

A summary of publications submitted by the PhD candidate during the project are as follows:

- **Conference proceeding**, Modelling of Nitrogen Transport in Iron Lattices with Point Defects, *European Conference of Heat Treatment (2018)*, Aurash Karimi and Michael Auinger.
- **Journal Article**, Thermodynamics of the iron-nitrogen system with vacancies. From first principles to applications, *Journal of Alloys and Compounds [5] (2020)*, Aurash Karimi and Michael Auinger.

- **Journal Article**, Nitrogen diffusion in vacancy-rich ferrite and austenite, from first principles to applications, *Acta Materialia* [9] (2021), Aurash Karimi and Michael Auinger.

1.2 Motivation and Background

This section is a brief overview of the metallurgical background required to understand the goals of the PhD project. The reader is advised to review this section before proceeding to others, as the other sections assume this knowledge.

1.2.1 Allotropes of Iron

Iron and its alloys have remained the most important material in engineering and construction for thousands of years, and it has been a prevalent research topic for almost the same amount of time. Steels, which are the most prominent iron-alloy, are defined as an iron-alloy containing over 2.06 wt.% carbon. The versatility of iron-alloys means that its list of applications is endless, and accordingly, so are the potential manufacturing optimisations to purpose an iron-alloy for each of these uses. Fortunately, from a modelling perspective, one can often simplify a manufacturing process to its vital elementary components and still produce useful and predictive computational outputs. The two most important allotropes of iron, α -Fe (ferrite) and γ -Fe (austenite), are the focus of this work. In pure iron the α phase is energetically stable below 912°C, and the iron atoms form a body-centered cubic (BCC) lattice/crystal structure. Between 912°C and 1394°C the γ phase is stable, forming a face-centered cubic (FCC) lattice. Between 1394°C and the melting point at 1538°C, iron adopts a BCC crystal structure termed δ -Fe. Due to the high degree of symmetry in both crystal structures, they can be completely described by their lattice parameters. This is commonly denoted by a as shown in figure 1.1.

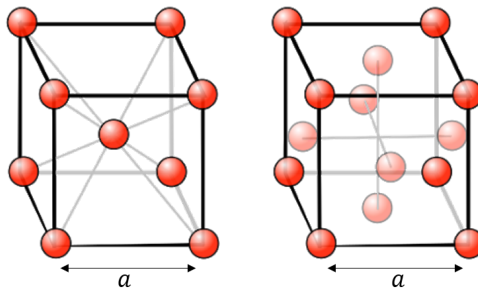


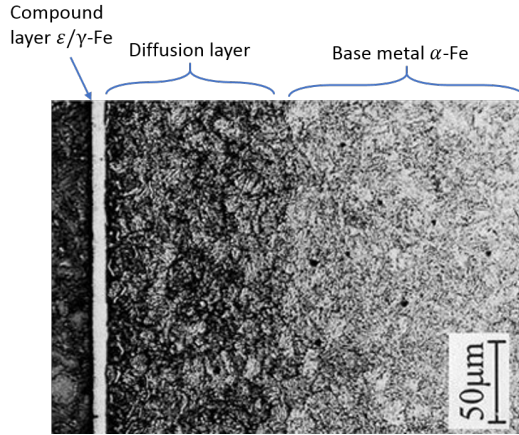
Figure 1.1: Body-centered cubic (left) and face-centered cubic (right) crystal structure with lattice parameter a . Figure has been modified from [1].

The phase transition temperatures of iron are highly dependant on the presence of *interstitial elements* such as nitrogen and carbon. α -Fe is relatively insoluble compared to γ -Fe. If the metal contains a large quantity of solutes, the γ phase becomes stable at lower temperatures, entering the so called *expanded austenite* phase. The phase transition temperatures are also dependent on the alloy composition. For instance, alloy additions such as aluminium can extend the stable temperature range of α -Fe.

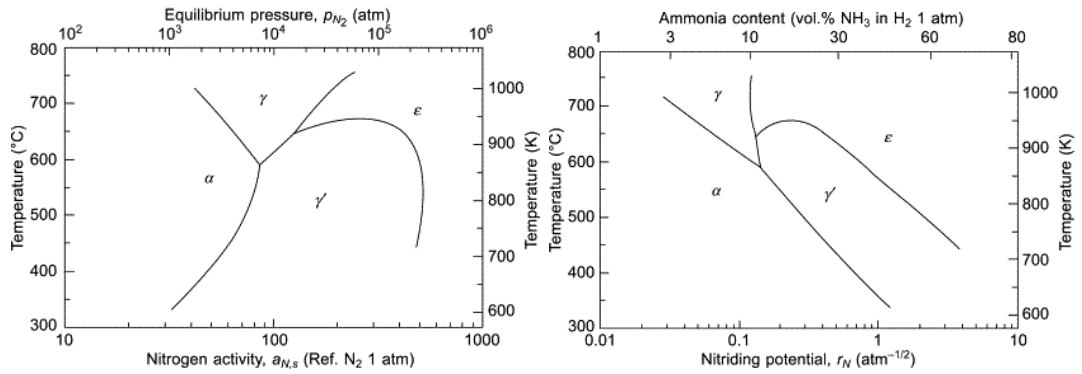
1.2.2 Heat Treatment of Iron Alloys

The essence of heat treatment is improve the resistance properties of a metal without sacrificing a significant amount of its ductility or modifying its existing crystal structure. Heat treatment is used to improve mechanical properties such as hardness, wear and fatigue resistance; and chemical properties such as corrosion resistance [12]. There is a broad range of applications for heat treatment, which includes vehicle/aircraft parts, cutting tools and gears [13]. Some applications are unconventional, for example, there are unique musical instruments named hang drums/handpans which are heat treated to fine-tune their resonance frequencies [2]. To date, the most important heat treatment processes are nitriding/nitrocarburising and carburising/carbonitriding [3]. In essence, these processes bombard the surface of the metal with nitrogen or carbon, resulting in the formation of a hard nitride/carbide layer which protects the softer core metal. The surface layer is only the tip of the proverbial iceberg. Several inner layers with sparser nitrogen/carbon concentrations need to be properly formed to create the desired material properties [14, 3, 15], resulting in a dynamic multi-phase structure as the interstitial element diffuses into the metal (see figures 1.2a and 1.2b).

If a metal is heat-treated for too long, it becomes brittle. This is because the interstitial elements fill up spaces in the iron lattice, making the structure more rigid. On the other hand, overly short heat treatments can compromise the load-bearing capabilities of a metal. Care must be taken that the treatment is long enough to ensure that there is a smooth transition in the concentration of interstitial atoms between the layers resulting from heat treatment. Otherwise, the hard surface can crack and penetrate inwards due to insufficient support from the inner metal layers. This phenomenon is analogous to an egg shell cracking with relative ease upon impact, despite its hard wear-resistant surface, and is consequently referred to as the *eggshell effect* [16, 17].



(a) Micrograph of nitrated high purity iron



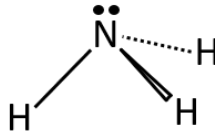
(b) Iron-nitride phases

Figure 1.2: Top: Micrograph showing the composition of nitride layers in iron after nitrating heat treatment (source [2]). Bottom: Stability of iron-nitride phases under a range of nitrating conditions, the right hand side diagram is commonly referred to as a Lehrer diagram (source [3]).

1.2.3 Nitriding

The modelling methodology outlined in this work will generalise to a multitude of applications in heat treatment and beyond. Despite this, it was deemed suitable to restrict the current scope of the research to nitriding to satisfy the time constraints of a PhD project. Nitriding is a relatively low temperature heat treatment process carried out at around 500°C. There are several variants of nitriding used in industry, with the most common of these being gas, plasma and salt bath nitriding. Salt bath nitriding has gradually fallen out of favour over time due to the toxicity of the salts used, so the gas and plasma variants are far more common.

The main difference between different nitriding processes is the way in which



(a) Ammonia NH_3



(b) Nitrogen gas N_2

Figure 1.3: Bonding diagram of nitrogen molecules. Dots indicate lone pairs of electrons.

they catalyse surface-adsorption of nitrogen on the metal. The conditions should be chosen such that the recombination of nitrogen atoms into nitrogen gas (which is released back into the atmosphere) proceeds at a much slower rate than its adsorption and diffusion into the inner metal. For instance, gas nitriding achieves this by employing the tendency of ammonia to form iron nitrides when in contact with iron. Due to the relative weakness of the single bonding in ammonia compared to the triple covalent bond in N_2 (see figure 1.3), it creates a far higher nitrogen activity under typical processing conditions than pure nitrogen gas. Nitrogen gas is abundant and stable in the atmosphere at room temperature, whereas ammonia is thermodynamically favoured to decompose into nitrogen and hydrogen gases at any temperature above 0°C [3]. Hence, at heat treatment processing temperatures, the equilibrium of



is heavily favoured towards the right hand side of the reaction. Inspecting the equilibrium suggests that it is not possible to maintain a substantial concentration of ammonia in the atmosphere for nitriding. However, as discussed, ammonia is far more *useful* in this context than nitrogen gas. Fortunately, the rate at which ammonia decomposes is relatively slow below 500°C , so the reactants of 1.1 don't reach their thermodynamic equilibrium concentrations during nitriding. The partial pressures of ammonia and hydrogen control the nitrogen activity of the nitriding process [3] by shifting the equilibrium of reaction 1.1. By controlling the flow of the two gases pumped into the nitriding chamber, one can control the nitride composition of a treated metal. This is seen through the equation

$$r_N = \frac{p_{\text{NH}_3}}{p_{\text{H}_2}^{\frac{3}{2}}} p_0^{\frac{1}{2}}, \quad (1.2)$$

where r_N is referred to as the *nitriding potential*, p_0 is the reference pressure usually set to ambient pressure $p_0 = 1$ atm, and p_{NH_3} and p_{H_2} are the partial pressures of ammonia and hydrogen gas respectively. r_N is used to control the nitriding process by parameterising the type of iron nitrides which will form at equilibrium. In fact, a plot of temperature against nitriding potential is such a frequent referential tool in this process that it has its own terminology. It is called a *Lehrer diagram* 1.2b, named after the early pioneer of nitriding E. Lehrer [18]. The phases depicted in figure 1.2b show the typical layers grown in the nitriding process (micrograph of these layers in figure 1.2a). Typically, hard but brittle Fe_2N (ϵ -Fe) and Fe_4N (γ' -Fe) form the compound/white layer on the surface which gives the treated metal its desired surface properties. This layer is polished to reduce the brittleness and give a more uniform surface. The diffusion layer which supports the hard surface is formed of progressively less nitrogen-dense α -Fe in most cases. However, recent interest in high nitrogen steels means that the diffusion layer may also constitute of γ -Fe (see [19]).

The fine control over the thickness and uniformity of each nitride phase offered by gas nitriding has allowed it to stand the test of time, it remains the most popular nitriding method despite being the oldest (first documented in 1929). This fine control is usually sacrificed in other nitriding methods in exchange for other advantages. Plasma nitriding, for instance, works by passing an electric current through a mixture of nitrogen and hydrogen [20]. Plasma nitriding is particularly suited for situations where only selected sections of the surface should be nitrided, or low treatment temperatures are required. The voltage generated in plasma nitriding plays a role analogous to ammonia in gas nitriding, generating a nitrogen activity which is far beyond atmospheric levels. However, there is not an equivalent of equation 1.2 for plasma nitriding [21]. That is, the process parameters can not easily be related to the phase diagrams of stable nitride compounds (or equivalently, the Lehrer diagram) meaning that precise control of nitride layers is far more challenging. The major distinction between nitriding methods is the interactions at the surface. The subsequent diffusion of nitrogen to the inner metal is mechanically identical for all nitriding methods, so the diffusion model in this thesis is applicable regardless of which nitriding method is used.

1.2.4 Objective

The essence of the PhD project was to enhance the understanding and modelling capability of processes like heat treatment which rely on accurate prediction of phase stability and diffusion speed under given conditions. This was achieved by making novel contributions to the understanding of the nitriding process in both theoretically ideal symmetrical crystal structures, and imperfection-rich structures. Quantitative models were developed for both situations and verified against experimental data where possible. The lattice imperfections are represented by introducing independent vacancies (missing iron atoms) into the lattice. That is, a BCC/FCC lattice with some proportion of vacancies is considered to behave similarly to a lattice with that same proportion of miscellaneous crystal defects. Within this approximation, density functional theory (DFT) was utilised to produce quantitative predictions from first (quantum-mechanical) principles.

This work aimed to build on the current DFT literature for the iron-nitrogen-vacancy system and resolve discrepancies between different sources. DFT data for the system was required at a high degree of accuracy relative to the existing literature. The DFT data was used to establish a link between first principles and metallurgical applications, through novel investigations of thermodynamic/diffusion behaviour in the system. The first principles approach was validated by identifying appropriate experimental data to compare to the calculated data. Moreover, it was investigated whether the experimental data is more accurately depicted by vacancy-rich lattices due to naturally-occurring defects.

Chapter 2

Literature Review

2.1 Nitriding Models

Models for nitriding require a combined knowledge of both the thermodynamic and diffusion qualities of the system of interest. Thermodynamic data is used to determine the nitrogen solubility and stable nitride phase (see figure 1.2b) phase at the surface, where the system quickly reaches equilibrium. Diffusion data is used to determine the rate at which nitrogen disperses into the inner metal. That is, the rate at which the inner metal reaches equilibrium with the nitrogen-rich surface. Proprietary software uses thermodynamic and diffusion databases to interpolate/extrapolate the behaviour of a system at the desired conditions. At the time of writing, the databases are almost entirely comprised of historical experimental data [8, 22]. There are several disadvantages to relying on experimental data to make predictions:

- The spread of data from different sources is sometimes large for the system and conditions of interest. It is often difficult to identify the cause of the spread and reduce the corresponding error margin it causes.
- The generalisation of the available data to new conditions requires interpolation/extrapolation. Interpolation is usually effective, provided there are not large gaps in the dataset, but both are problematic if the number of data points are not sufficient in the desired range.
- Experimental data for some systems is unattainable because the methodology is not developed/impractical. For instance, there is currently no commonly implemented experimental method to quantify the solubility of interstitial elements such as nitrogen in vacancy-rich iron.

The above limitations do not apply if the source of the data is density functional theory (DFT), because the system is solved from first principles. The data from DFT is not tied to thermodynamic variables such as temperature and volume, so it is not necessary to interpolate/extrapolate from it. The limitations of DFT are of a different nature, as discussed in section 3.1.2.

Iron alloys are typically nitrided after the sheet metal is machined/worked into the desired shape, as one of the final processing steps in a steel-making foundry. At an industrial scale, the nitriding process is predominately controlled by phenomenological knowledge of specific industrial alloy grades [3]. This is gradually changing in the digital age, with the usage of proprietary software for modelling increasing due to the business benefits they provide [8, 22]. In the current state of the art, nitriding models approximate ideality in the crystal structure of the iron [23, 24]. That is, that the layers of the iron lattice are perfectly stacked and homogeneous. However, producing an idealised sheet metal in the foundry with exactly specified compositions of alloy and interstitial elements, is far away from what is currently achievable. Numerous imperfections in the crystal structure such as grain boundaries and dislocations are observed, even in alloy grades which are processed specifically to maximise purity. Moreover, processes such as irradiation [25, 26], quenching [27], ball milling and shot peening [28] induce further deformation of the iron lattice. Hence, iron which perfectly conforms to a body centered (α -Fe) or face centered (γ -Fe) cubic lattice arrangement, is not always a valid approximation for industrial alloy grades. This is cited as one of the possible reasons that nitriding models deviate from experiment results [23, 29, 30]. Imperfections in the iron crystal structure tend to reduce the packing efficiency of iron atoms. This causes excess unoccupied volume within the crystal structure, which increases the vacancy activity [31]. There is evidence that iron alloys in nature behave as if they are far more vacancy-rich than simulated idealised lattices [32]. Thus, this work explores the case where the concentration of lone vacancies is more plentiful than would be expected at thermodynamic equilibrium.

2.2 Experimental Data

There is a vast collection of experimental thermodynamic [6, 33, 34, 35] and diffusion [10, 11] data recorded in literature for the iron-nitrogen system. In general, nitrogen and carbon interstitials are found to have similar diffusion and solubility in iron [36, 6]. This is not unexpected, nitrogen and carbon are adjacent to each other in the periodic table. Oxygen behaviour is also relatively close to the other

two interstitials [37]. Due to the importance of the system, there are frequent assessments of the available data [7, 3]. These assessments condense the historical information by fitting the data to simple expressions which are easily computed. The experimental methods improve over time which reduces the variance between different sources, leading to accordingly smaller error margins in fits to the data. There is still considerable room for improvement, because in current assessments there are error margins of at least $\pm 50^\circ\text{C}$. At industrial scales, even a temperature change of several degrees can result in a significant cost and energy reduction for the process.

Experimental methods for measuring the diffusion of interstitial atoms such as nitrogen, carbon and oxygen fall in to two main categories. Low temperature (up to around 200°C) techniques such as the *internal friction method* [38] measure interstitial diffusion indirectly, by relating it to the mechanical behaviour of the metal in low stress conditions [39]. High temperature techniques directly measure interstitial diffusion, by considering the average displacements travelled by the interstitial atoms over time [39]. Extrapolation from low temperature diffusion data to high temperature and vice versa is problematic. This is because temperature-related effects such as magnetism [10] can create significant divergence between the two data sources. This motivates a first principles approach, because it would allow the inclusion of temperature-related effects by construction. Moreover, extrapolation is not required from first principles, because the diffusion data can be calculated at any temperature on the fly.

There are currently no documented experiments which are used to directly calculate nitrogen-vacancy trapping energies. The energies are calculated indirectly by employing resistivity recovery [40] and irradiation [41]. Neither of the cited studies, which consider α -Fe, agree strongly with each other or first principles calculations. Due to the sparsity of the literature, it is not possible to conclude the reasons for the discrepancies. There have been no experimental attempts to calculate the trapping energies for γ -Fe, most probably because of its instability at low temperatures.

2.3 First Principles Modelling

In the past decade, several DFT studies which consider the iron-nitrogen system from first principles for α -Fe [42, 43, 44, 45, 46] and γ -Fe [47, 48] have been published. Two of these publications make distinct comparisons to experimental data [42, 44]. However, such comparisons are used primarily to validate the DFT calculations. It

is common in DFT literature to consider carbon and oxygen interstitials alongside nitrogen interstitials. This is because the data reaches a much broader range of applications with relatively small changes required to the modelling method. There is a consensus between DFT calculations and experimental data that the three interstitials behave similarly in iron [42, 46].

Considerable work is still required to bridge the gap between DFT calculations and thermodynamic modelling in an applied context. For instance, previous to this PhD, there have been no attempts to access the lehrer diagram from first principles (see 1.2b). Moreover, there is not a strong agreement between different sources for identical DFT calculations. Analogous to experimental studies, DFT calculations are expected to vary with the type of software (analogous to experimental methodology) used and the computing power (analogous to manpower and facilities) available.

Utilisation of DFT in higher-scale models is required to decisively determine the difference between tangible high-purity iron and the theoretical idealised iron lattice. The simplest first principles model which can be used to represent *imperfect* lattices is comprised of lone nitrogen interstitials, vacancies and nitrogen-monovacancy complexes. Where nitrogen-monovacancy complexes refer to a single vacancy in iron which has trapped some number of interstitial nitrogen atoms. It is evident from the surrounding literature that the three point defects mentioned carry large significance while maintaining simplicity. While larger multivacancy complexes may be abundant, it is reasonable to approximate these as the product of multiple monovacancy complexes [42]. Previous to the PhD study, there are no recorded attempts to quantify the effect of lattice imperfections on the behaviour of nitrogen in iron.

Chapter 3

Review of Computational Methods

3.1 Density Functional Theory (DFT)

DFT is a computationally intensive method which is used to simulate an atomic-scale sample (usually 1000 atoms or less) of a system of interest to a quantum mechanical degree of accuracy. DFT studies are a subset of what are referred to as first principles studies. This is because DFT is used to simulate atomic-scale particles within quantum mechanical theory with relatively few simplifications. What follows in this section are both a theoretical introduction to DFT and the practical considerations of applying the theory in the context of the present nitrogen-iron-vacancy study.

3.1.1 Theoretical Origins

DFT is a robust method which can be used to study the fundamental constituents of any matter in the physical world. The theory is unsurprisingly rich and was developed over many decades by highly distinguished researchers. The scope of this section is limited to the theoretical aspects of DFT which are useful to understand the work herein. For further exposition, the reader is referred to an introductory text such as [49]. Consider a system of N electrons and M atomic nuclei. The nuclei are much larger objects and move far slower than the electrons. This is the basis for the Born-Oppenheimer approximation [50], which is used in DFT to treat the nuclei and electrons as separate systems which can be simulated independently. In fact, the nuclei are considered to be large enough that they follow classical mechanics. This means that the calculation of forces between the nuclei does not pose a significant problem. The many-body simulation of the N electrons poses a far more involved

challenge, which remains an active research topic today. Although DFT is based on the Schrodinger equation which was first formulated in 1924, it was many decades before a viable method of computing electronic properties was developed. The first key development to this end was the Hohenberg–Kohn (HK) theorems [51]. Consider the many-body electron wave function, denoted $\Psi(\{r_i\})$. Here, there is an i for each of the N electrons considered and r_i is a 4 dimensional vector which contains the three Cartesian coordinates of the electron and its spin. Ψ associates each possible combination of position and spin of an electron with the probability of its existence in that combination. In particular, if the wave function is normalised, $\Psi^*(x)\Psi(x)$ is the probability that the system is in state x ; where $\Psi^*(x)$ is the complex conjugate of $\Psi(x)$. If Ψ is a known expression for a given system, the expected values of position, momentum and potential energy are calculated using the probability distribution implied by Ψ by averaging the quantity over the whole domain of space and spin states. For example, the average potential energy $\langle E \rangle$ of a system can be expressed as

$$\langle E \rangle = \int_{-\infty}^{+\infty} E(x)\Psi^*(x)\Psi(x) dx. \quad (3.1)$$

Where $E(x)$ is the potential energy of the system in state x . However, determining the functional form of Ψ is only possible in trivial systems. Ψ depends on each electron and electrons can interact with every other electron in the system as well as themselves, resulting in high complexity. The contribution of HK was to reinterpret Ψ , a function with $4N$ variables, so that the dimensions of the problem are drastically reduced. It was shown that for a given system, there is a one-to-one correspondence with the Ψ for that system and the electron density denoted $\rho(r)$. That is, for a chosen system, there is a unique function $\rho(r)$ which defines the probability that any electron in that system is in position r . $\rho(r)$ is a 3 dimensional function which is just as useful, in a practical sense, as having access to the full $4N$ -dimensional wave equation Ψ .

A key property of electron densities is that the electrical energy E of a system can be expressed as a *functional* of them. That is, E is a function of the form $E[\rho]$ which accepts an electron density function as an input and returns a scalar value - the electronic energy which corresponds to that electron density. Moreover, another important consequence of the HK theorems is that only the *ground state* electron density $\rho_0(r)$ will minimise this energy. In fact, it is this consequence that allows DFT to work at all, as there is otherwise no way to verify a candidate electron density for a given system. Rather, it is possible to follow an iterative procedure to

minimise the electrical energy with progressively better candidates for $\rho_0(r)$. The iterative procedure has a clear stopping criteria, as the true ρ_0 would minimise the value of $E[\rho_0(r)]$. In order to make the problem computable, $E[\rho(r)]$ is separated into separate contributions by the Kohn Sham (KS) equations [52]. In particular, $E[\rho(r)]$ is written in an exact form as the sum of kinetic, external potential, coulomb and *exchange-correlation* contributions. KS DFT is not an exact method to solve for $\rho_0(r)$. For instance, a universal exchange-correlation (XC) functional which applies to any system has not been found [49]. In practice, estimations of the XC functional are used, depending on the nature of the system. This is because the XC contribution is the smallest in the overall potential, and good methods of estimating it exist in practice even though its true form is not known. All calculations in this work use the Perdew–Burke–Ernzerhof (PBE) functional [53], in accordance with all other recent DFT literature examining the iron-nitrogen-vacancy system.

3.1.2 Limitations of DFT

It is clear from the discussion in section 3.1.1 that the accuracy of a KS DFT calculation is dependent on the XC functional chosen. In current practice, the XC functional is the only aspect of DFT theory which is almost certain to require an approximation. Contemporary DFT research is oriented towards improving the accuracy and versatility of XC functionals. Recent approaches which utilise advances in machine learning [54] show significant progress towards a universally accurate XC functional. KS DFT is vulnerable to self-interaction errors which arise from the hartree potential, which is used to represent the coulomb repulsion between each electron and the overall electron density. Because each electron contributes to the electron density, the hartree potential includes an unphysical repulsion between each electron and itself by construction. This is referred to as the self-interaction energy. For instance, in a single electron system such as a lone H_2^+ ion, the hartree potential in the KS formulation is nonzero [49]. In this case, the contributions from the hartree potential are entirely self-interaction error, because a single electron system does not contain electron-electron repulsion. If the XC functional is used in its exact form, the self-interaction energy cancels with the XC contributions. However, this is rarely the case in practice, because the XC functional is approximated. Self-interaction error causes electrons to over-delocalise because the electron-electron repulsion is overestimated. In particular, unpaired electrons tend to delocalise spatially to minimise their self-interaction. This is an important consideration in transition metals with strongly localised electrons, which are said to be *electron-correlated*, such as iron oxides [55]. The self interaction error is reduced

by using a *hybrid XC functional* [56], this modifies the KS formulation to reduce the self-interaction error, although the added complexity of the functional significantly increases the computational cost. A cheaper approach is DFT+U [57], which adds a simple correction term for self-interaction, although this requires the selection of an appropriate $U - J$ parameter. Iron nitrides are more electron-localised than pure iron, particularly if they are ordered such as in FeN, Fe₂N and Fe₄N. However, although the surrounding DFT literature is sparse, it appears that a self-interaction correction is not required in order for DFT calculations to show good agreement with the theoretical and experimental data for iron nitrides [58].

All-electron DFT calculations, where every electron is considered in the solution for the electron density, are rarely used in practice. This is because all-electron calculations are only computationally viable for small systems with few enough electrons. A *frozen core* approximation is required to reduce the computation time of DFT calculations. A frozen core approximation considers the core electrons of an atom which are close to the nucleus to be transferable between different systems. This allows the core electrons to be omitted from the DFT calculation, because their contribution to the electron density is calculated from parameters recorded in a database. This is a reasonable approximation because the core electrons are insensitive to the surrounding environment of the atom, relative to the outer electrons. The simplest variant of the frozen core approximation represents the electron density of the core electrons using a *pseudopotential*. Pseudopotentials which are fitted from empirical data for most atoms in the periodic table are included as a standard feature in DFT software. Calculations in this work employ the projector augmented wave (PAW) method, which is generalisation of the pseudopotential method that is more effective in strongly magnetic systems such as α -Fe [59].

3.1.3 Output

A DFT implementation allows us to calculate the ground state electron density $\rho_0(r)$ of a chosen system with high accuracy, subject to an appropriate choice of XC functional. An immediate benefit comes from recalling that $\rho_0(r)$ minimises the electrical energy functional $E[\rho]$, which is calculated as part of the DFT process. The final minimised energy value of this functional, which can be calculated to an arbitrary degree of accuracy (typically around 0.0005 eV) is combined with the energy contributions of the atomic nuclei to form the *ground state energy*. DFT can be considered from a practical perspective as a black box which outputs the ground state energy depending on a series of input parameters. The task then remains for the DFT practitioner to optimise the input parameters to give the most accurate ground state

energy possible while maintaining a feasible computational time. A crucial feature of the ground state energy, is that it is only the true energy of the system at absolute zero/zero kelvin which is around -273.15°C . Whilst the principles of quantum mechanics ensures that atomic particles are not completely motionless and static, even in absence of thermal energy, the extent of this motion is restricted to *zero-point* vibrations about the atomic equilibrium positions. Thermal energy is required to excite the system enough so that *interesting* reactions, that can be observed on a metallurgical scale, are possible. Fortunately, there are well-established models for how the energy changes dynamically as the temperature increases. Given access to ground state energies, one can determine both thermodynamic (see section 3.2) and kinetic behaviour (see section 3.3) of a system with respect to temperature. Moreover, provided that the computational resources are available, further information calculated from DFT can be used to improve the temperature-dependent models from what can be achieved with the ground state energy alone. For instance, one can account for the temperature-dependant vibrational energy (see section 3.2.1), or the effect of thermal volume expansion (see section 3.2.2).

3.1.4 DFT Models of Iron

Section 1.2.1 introduced two allotropes of iron, α -Fe and γ -Fe, which are the focus of this work. With reference to figure 1.2b, these allotropes are the only forms of bulk iron which are stable under typical nitriding conditions. In this section, it is briefly summarised how α -Fe and γ -Fe are represented as systems in the DFT formalism.

α -Fe is the stable phase of pure iron below 912°C , although this temperature upper bound decreases sharply when the iron is exposed to high activities of interstitial elements such as nitrogen and carbon. Conversely, γ -Fe is the stable phase at 912 - 1394°C , but this range will expand to lower temperatures if the solute elements are in abundance. δ -Fe is the stable allotrope at 1394°C - 1538°C , the upper bound of which is the melting point of iron. δ -Fe adopts the same BCC crystal structure as α -Fe. However, as the temperature increases, the true system will tend to diverge from the assumptions of the model employed in this work. This is due to the nature of DFT, which provides the ground state energy corresponding to absolute zero temperature. Therefore, despite the identical crystal structures, the DFT calculations in this work will be more representative of α -Fe than δ -Fe.

The magnetism of iron can be incorporated by running *spin-polarised* DFT calculations. In this instance the magnetic moment for each atom in the supercell is calculated in addition to it's electron density. Spin-polarised calculations require at least twice the computing time of non-polarised calculations, but they are essential

to model strongly magnetic materials at low temperatures with acceptable accuracy. In particular, spin-polarisation must be used for α -Fe, which is ferromagnetic below its Curie temperature of around 770°C. γ -Fe is not stable at low temperatures, so it is difficult to verify its magnetic qualities experimentally. Indeed, the magnetism of γ -Fe is a contemporary topic in literature. It is known to behave as a para-magnetic, anti-ferromagnetic [60], or ferromagnetic [61] metal under different conditions. Moreover, γ -Fe has been shown to have a spin spiral ground state [62] which is indicative of competing anti-ferromagnetic and ferromagnetic exchange interactions. Hence, the introduction of magnetism in the γ -Fe model would require multiple magnetic spin states to be calculated. This level of complexity is not unlikely to be warranted for the current work. In general, magnetic contributions tend to smaller at the high temperatures where γ -Fe is more abundant. Hence, modelling γ -Fe as non-magnetic was considered the best choice in this work.

In summary, the DFT study is carried out on two systems. BCC ferromagnetic and FCC non-magnetic iron are used to represent α -Fe and γ -Fe respectively. A BCC *unit cell*¹ contains 2 atoms, 12 tetrahedral interstitial sites and 6 octahedral interstitial sites, while a FCC unit cell contains 4 atoms, 8 tetrahedral sites and 4 octahedral sites. In both cases, octahedral sites are the lowest energy site for nitrogen interstitial atoms [5] (visualised in figure 3.2). Moreover, tetrahedral sites, which sit equidistant between neighbouring octahedral sites, are the transition sites for nitrogen to jump between the stable octahedral positions [9].

3.1.5 Plane-Wave DFT

Supercell

DFT calculations are demanding on computational resources. Even with access to high-performance computing facilities, the systems studied must usually be restricted to 1000 atoms or less. Initially, this may cause one to question how useful it is for modelling metals in an applied context on an exponentially larger scale. The answer lies in the periodicity of metallic structures. That is, a large symmetrical structure can be considered equivalent to a repeated small structure. Any symmetrical lattice defined in real space can be transformed into a *reciprocal lattice*. The size of the metal is not an obstacle in practice, because reciprocal lattices are used to represent real space lattices of arbitrary sizes. Suppose that the potential energy function of a reciprocal lattice is denoted $V(r)$, and T is any trans-

¹A unit cell is a cell which contains the minimum amount of atoms required to define the crystal structure.

lational vector of the lattice which maintains the symmetry of the location given by r . In this case, $V(r + T) = V(r)$, because the energy should not change if the positions are equivalent.

Bloch's theorem [63] states that a wave function Ψ which solves the Schrodinger equation for the choice of V can be written in the form

$$\Psi(r + T) = \Psi(r)e^{ikT} \quad (3.2)$$

where k is a positional vector in reciprocal space. This means that any wave function is equivalent under translation up to the phase factor e^{ikT} . This shows that the probability of finding an electron at a given position is invariant under translation because

$$\Psi(r + T)\Psi^*(r + T) = \Psi(r)\Psi^*(r)e^{ikT}e^{-ikT} = \Psi(r)\Psi^*(r). \quad (3.3)$$

In terms of DFT output, this means that one only needs to solve for the electron (probability) density function in the *unique* reciprocal lattice space to obtain the electron density function of the whole lattice. DFT problems can be solved more conveniently in reciprocal space/k-space in favour of real space because of Bloch's theorem. This variant of DFT is referred to as *plane-wave DFT*, and is the most common method employed for metals. In high-symmetry cases such a pure iron, it allows the calculation of some bulk metal properties using unit cells of just 2 or 4 atoms for BCC or FCC iron respectively.

Since lone point defects such as vacancies or interstitial elements such as nitrogen atoms are the topic of study, unit cells are not sufficient for the required DFT calculations. The cells are defined in reciprocal space, so the defects will be repeated with the same periodicity as the iron atoms. This means that defect-defect interactions will affect the DFT calculations, so the defect cannot be considered a lone defect. To this end a *supercell* is used, which is a periodic unit repeated some prescribed number of times in the 3 cartesian dimensions (see figure 3.1).

A supercell is chosen that is large enough that the interaction between the defect of interest with its periodic images is diluted. In essence, the supercell containing the point defect should be large enough that its electronic structure is more or less identical to the defect in single-crystalline iron. The resulting output values obtained from this supercell are then said to be accurate within the *supercell approximation*. The appropriate supercell is often not known beforehand, and must be obtained through systematic experimentation. That is, by increasing the supercell size until the energy difference between successive increases is small enough. The

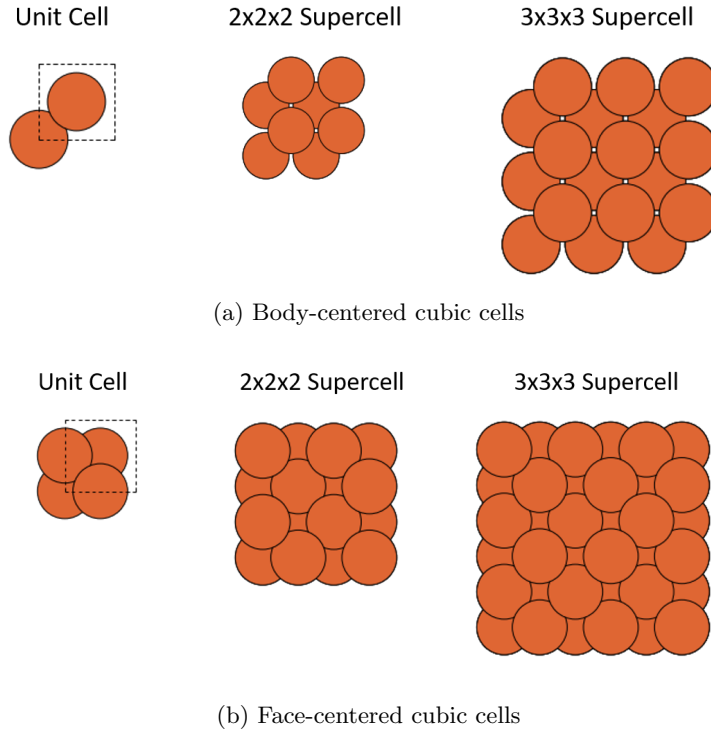


Figure 3.1: Examples of supercells with BCC (top) and FCC (bottom) crystal structures. Dashed lines indicate the boundaries of unit cells.

system is then said to be *converged* with respect to the supercell size. In general, convergence is a crucial part of carrying out DFT calculations. The first step to validating DFT results is to ensure they are well converged with respect to supercell size and other parameters. In practice, one is limited by computing resources. A fine balance must be struck between ensuring results are well converged, but also achievable with the available time and resources.

k-Points

To solve for the ground state electron density in plane-wave DFT, the density must be discretised evenly in reciprocal space. This is typically achieved algorithmically by a method such as the one outlined by [64]. The discrete points in reciprocal space are referred to as k-points. Similarly to the supercell size, the number of k-points to sample in each dimension is a sensitive parameter and should be well converged. The results will not be accurate if an insufficient number of k-points are used, but adding more k-points increases the computational cost. This means that the number of k-points should be reconsidered each time the supercell size is changed. A fortunate

consequence of working in reciprocal space is that larger cells in real space are smaller in reciprocal space. Hence, a larger supercell will generally require fewer k-points than a smaller supercell. This dynamic has the benefit of offsetting some of the cost incurred by using a larger supercell. It is further important to note that solving for the functional at each k-point is independent to other k-points. This means the calculations for each k-point can be computed in parallel. In large research-scale calculations, it is essential to use this fact in DFT software by assigning k-points across multiple computing cores. Although plane-wave DFT calculations may be parallelised at other stages, k-point parallelisation is the most efficient way to utilise multiple cores.

A final important consideration when using k-points applies specifically to metals. At the ground state there is a portion of reciprocal space which is unoccupied by electrons, separated from the occupied portion by the *Fermi surface*. The sudden discontinuity of electron occupancy at the Fermi surface causes a problem for resolving the electron density using k-points. This is because the calculation relies on numerically integrating between k-points. Numerical integration algorithms tend to perform poorly at discontinuities, unless a large number of sampling points of the electron density in k-space are used. Since computational burden is a concern when k-points are increased, several methods have been developed to make the integration more efficient. A common method is smearing, where the integration is performed on a *smoothed out* electron density rather than the true density. This will not have a significant impact on the accuracy of the results, as the smoothed electron density is engineered to have the same integral as the true density. However, the smoothed density will require far less k-points to be considered well converged. A frequently used smearing algorithm is that of Methfessel and Paxton [65].

Cut-Off Energy

The ground state density in plane-wave DFT is comprised of expressions of the form e^{iGr} , where G is a reciprocal-space vector and r is a real-space vector. In order to calculate the density; the e^{iGr} terms must be summed over all possible values of G , of which there are infinitely many. Fortunately, the majority of G values can be omitted, as they correspond to kinetic energy values which are too high to be physically relevant. This leads to an additional important parameter in plane-wave DFT, the *cutoff energy*. The cutoff energy is a constraint which ensures that only G values associated with an energy lower than its value are included in the sum. The cutoff energy is similar to supercell size and k-points in the regard that it should be well converged. In this context, converged means that it should be set

high enough that further increases do not have a significant impact on the output density. However, calculations in practice are rarely well converged with respect to the energy cutoff, due to the very large computational cost this would entail. Rather, it is ensured that the energy cutoff is kept the same in a series of calculations which involve similar systems. This allows for accurate calculations because of systematic error cancelling (see 3.1.7).

3.1.6 Software

Plane-wave DFT calculations are a series of complex mathematical operations which require tens to hundreds of thousands of lines of code to implement as software. This code will typically be written in a low level programming language such as C/C++/Fortran to allow for high efficiency and optimisation potential. Furthermore, the code should utilise multithreading/concurrency so that the computational workload can be distributed over many computing cores in parallel. In general, standard commercial desktop/laptop computers are not powerful enough to carry out DFT calculations at the level of novel research. Ideally, the researcher would have access to a high performance computing cluster, which commands 1000's of computing cores.

Writing a new implementation of plane-wave DFT would not be feasible or prudent for a PhD project, so all work in this project employs the existing open-source software GPAW [66, 67]. However, using the software in an applied setting is an involved process which requires careful tuning of parameters to optimise for computing time and accuracy (see section 3.1.5 for details). Several features of GPAW, which are also included in other popular software solutions, are utilised to increase productivity in this regard. The performance intensive C code is wrapped in Python objects so that it is easily understood, provided that one has a working knowledge of DFT. Several purpose-built file formats are used by the software to do various convenient tasks, such as save a supercell design or store intermediate calculation results. GPAW is accessed through the ASE software [68], which gives the means to employ a GPAW calculator to calculate vibrational frequencies (see 3.2.1) or optimise cell volumes (see 3.2.2). ASE also contains a GUI element to allow for convenient visualisation, which is often the first point of call to validate a system is correct, before expensive DFT calculations are run.

3.1.7 Error Cancelling

A general observation in DFT is that the absolute ground state energies are rarely calculated to a well-converged accuracy with respect to its parameters. This is often unfeasible due to computing resources. Fortunately, one is rarely interested in absolute energy values for a particular system. Far more often, the energy difference between two systems with a single elementary change is desired. This is because the equilibrium data for any elementary reaction (such as reaction 3.7) can be resolved given the energy change. Hence, the convergence of the DFT calculation can be based on the relevant energy difference for a reaction rather than the respective absolute energies. This is a great benefit to a DFT practitioner, as energy differences generally have much better convergence behaviour. The reason for this is best understood by a concrete example. Consider the process of calculating the internal energy for nitrogen in the nitrogen-iron system. This calculation involves subtracting the energy of an iron supercell E_{Fe} from the energy for the same supercell containing a single nitrogen atom E_{FeN} . Since the absolute energies from DFT calculations are rarely well converged, the actual energy values obtained will be $E_{\text{Fe}} + E_{\text{Fe}}^{\text{error}}$ and $E_{\text{FeN}} + E_{\text{FeN}}^{\text{error}}$. Where $E_{\text{Fe}}^{\text{error}}$ and $E_{\text{FeN}}^{\text{error}}$ are the respective differences between the absolute energies and their true values. In general, $E_{\text{Fe}}^{\text{error}}$ and $E_{\text{FeN}}^{\text{error}}$ would shrink as one uses a larger supercell, a finer k-point grid, or a higher energy cutoff. However, recalling section 3.1.1, the error will also be subject to the choice of XC functional and may not be completely eradicated by altering the DFT parameters.

Using the obtained DFT results to calculate the internal energy results in the equation

$$E_{\text{internal}} = E_{\text{FeN}} - E_{\text{Fe}} + E_{\text{FeN}}^{\text{error}} - E_{\text{Fe}}^{\text{error}}. \quad (3.4)$$

The two supercells in question are very similar, so provided that the same DFT parameters are used in each energy calculation, the two resulting error terms are likely to be similar too. Therefore, $E_{\text{FeN}}^{\text{error}} - E_{\text{Fe}}^{\text{error}} \approx 0$, suggesting that the value of equation 3.4 will converge to the desired value of E_{internal} more readily than the individual error terms will shrink to zero.

3.1.8 Structural Relaxation

In section 3.1.1, the Born-Oppenheimer approximation was used to treat the atomic nuclei separately from the electrons. That is, the ground state density was found by treating the heavy centers of the atoms as relatively immobile massive objects which are orbited by mobile electrons. However, there is a new ground state density

for the electrons for each different spatial arrangement of the nuclei, and only one of these represents the true ground state for the system. Thankfully, to minimise the energy with respect to the nuclei positions is a much simpler task than finding the electron density. Provided that the method is established for evaluating the ground energy of any positional configuration, it is a matter of following this energy surface to the global minimum. This is a well established optimisation problem in applied mathematics and many methods exist to do this efficiently. For instance, one of the most robust and well-known algorithms for this purpose is that of [69]. This process of minimisation is often referred to as *relaxing* a system, because the system is being arranged in its least agitated energetic state. In nature, the system is considered to fluctuate about this state while it is in equilibrium. Since most thermodynamic models assume these equilibrium mechanics, it is essential that the associated DFT calculations also correspond to equilibrium. For entirely symmetrical systems, such as perfect BCC or FCC lattices, relaxation is unnecessary because the atoms are in their ideal equilibrium positions by design. However, the addition of defects would cause local distortions and cause nearby atoms to adjust (see figure 3.2).

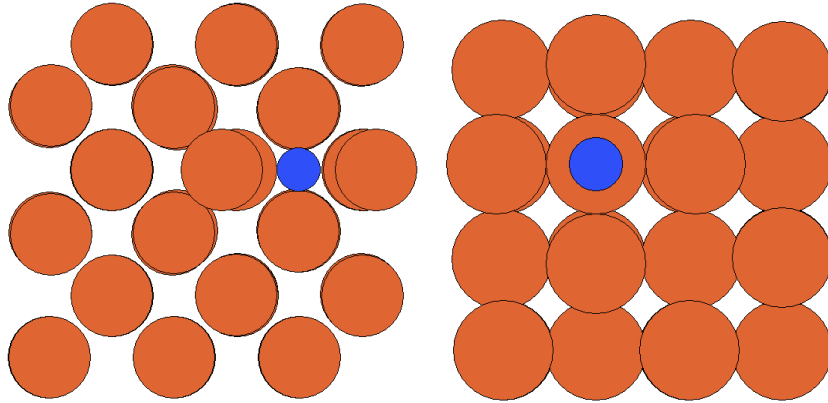


Figure 3.2: Relaxed BCC (left) and FCC (right) supercells containing a single nitrogen atom in an octahedral void. The nitrogen atom has caused local distortions in both cases which break the intrinsic symmetry of the supercells.

3.2 Thermodynamic Modelling

This section shows how, provided one has the means to carry out DFT calculations of the ground state energy as described in section 3.1, one can quantify the behaviour of the iron-nitrogen-vacancy system over a desired temperature range. It outlines the necessary theory which was required to form the novel thermodynamics study

in chapter 4.

3.2.1 Vibrational Contributions

A quantum mechanical system will always possess vibrational kinetic energy, even at absolute zero temperature where it has no thermal energy available. The kinetic energy that is present at absolute zero is referred to as the *zero-point energy*. In a regular metallic lattice, each atom tends to oscillate at the same frequency. This collective excitation is described by the *phonon density of states*, which is a probability distribution over the different vibration frequencies of the atoms. However, calculating the phonon density of states is very expensive, as it requires 6 evaluations of the ground state energy for each atom in the supercell. Nitrogen is a much lighter atom than iron, and lighter atoms tend to vibrate at higher frequencies, so the vibrations of lone nitrogen interstitials are not strongly correlated with those of the surrounding iron atoms. Therefore, it is a reasonable approximation to assume that the nitrogen contribution to the phonon density can be considered an independent vibration [70], which is a far cheaper calculation that requires only 6 energy evaluations in total. It is important, however, to note that the error margin from this assumption will increase at higher temperatures, as both vibrational and phonon contributions increase with temperature. Vibrational modes in this work are calculated using the implementation of ASE, which employs the methodology of [71].

3.2.2 Volume

The volume of both BCC and FCC cells are controlled by a single lattice parameter (see figure 1.1), which fluctuates about an optimal value when the system is in equilibrium. This optimal (energy minimising) lattice parameter at the ground state is calculated by a systematic series of energy calculations at varied lattice parameters. This data is then fitted to an *equation of state* and the minimum of the fitted function corresponds to the optimal volume. Fixing the optimised lattice parameter across the full range of calculations helps to cancel out systematic errors from DFT (see section 3.1.7). Recalling that the accuracy of DFT is limited by the chosen XC functional, this error cancelling is particularly important for this work which uses the PBE functional. This is because, particularly for γ -Fe, the discrepancy between the optimised DFT lattice parameter and the experimentally found lattice parameter is not negligible [5] when the PBE functional is used.

The optimal lattice parameter is a dynamic quality which changes with tem-

perature and pressure, leading to well-known phenomena such as thermal expansion [72]. In order to benefit from the error cancelling effect in DFT (see section 3.1.7) and reduced computational cost, it is often best practice to model the lattice parameter as a constant over a temperature range of interest. However, dynamic changes in volume may have a large impact on the quantity of interest. For example, thermal expansion increases the lattice spacing of the metal, which impacts the diffusion of nitrogen [9]. In these situations, it is prudent to perform an array of DFT calculations which represent the same system at different volumes.

Vibrational/phonon contributions (see section 3.2.1) are volume dependent. One may calculate the phonon density of states at a range of volumes, meaning that the volume-dependent phonon contributions at a range of temperatures can be readily calculated. By minimising the energy with respect to volume at each temperature in the range, one finds the optimal volume and energy at each temperature. This method is referred to as the *quasi-harmonic approximation*, and is implemented in several software packages such as phonopy [73]. It is computationally expensive to perform quasi-harmonic calculations to a high degree of accuracy. Thus, care should be taken to ensure that a simpler model, where the volume is not temperature dependent, would not suffice for the purpose at hand.

3.2.3 Configurational Entropy

Just as a system seeks to minimise its energy by finding its most stable arrangement in space, it will also simultaneously be stabilised by higher entropy. In a metal lattice with interstitial atoms *configurational entropy*, introduced by Ludwig Boltzmann, is the largest source of entropy by far. To intuitively understand why a larger configurational entropy leads to increased stability, one can consider the definition of configurational entropy for a lattice with k interstitial atoms with n interstitial spaces. It is based on the number of unique ways one can arrange the system while maintaining its energy at the minimum:

$$S_{\text{config}} = \frac{R}{N_{\text{A}}} \ln \frac{n!}{(n-k)!k!} \quad (3.5)$$

where $R = 8.314 \text{ J mol}^{-1} \text{ K}^{-1}$ is the universal gas constant and $N_{\text{A}} = 6.022 \times 10^{23} \text{ mol}^{-1}$ is Avogadro's number. Further, equation 3.5 assumes that the trajectories of interstitial atoms are random throughout the lattice. S_{config} is at its minimal value of 0 when $k = n$ (see figure 3.3), that is, when all of the candidate positions for interstitial atoms are filled up. This makes no difference to the stability of the system at absolute zero. However, as the temperature increases, the stability

of a $k = n$ system relative to a $k < n$ system decreases. The entropy in this context can be thought of as the efficiency of the system to store thermal energy as kinetic energy. The $k = n$ system is static with only one stable state, meaning that no additional kinetic energy can be stored even with an abundance of thermal energy. Conversely, the more dynamic $k < n$ system can alternate between many equivalently stable states. This relationship between entropy and temperature is seen concretely through the definition of thermodynamic variables like the Gibbs free energy. Namely, the entropy is multiplied by temperature to calculate its energy contribution.

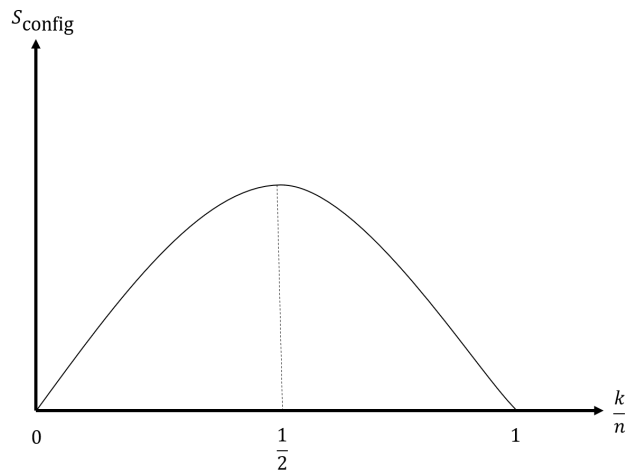


Figure 3.3: Relationship of configurational entropy with $\frac{k}{n}$, where k is the number of mobile particles in a system, and n is the number of possible candidate positions available for the particles.

In the example discussed here, only interstitial atoms such as nitrogen are considered for configurational entropy contributions. This work also seeks to model vacancies, which also contribute to configurational entropy. Moreover, nitrogen-vacancy complexes form as nitrogen atoms and vacancies interact in the lattice, which adds further complexity. The principles remain the same in all of these cases, there are just more complicated permutations of the different species to consider. This difference is captured in adjusted forms of equation 3.5 as seen in [5].

3.2.4 Gibbs Free Energy

Construction

For a reacting system at fixed temperature T and pressure p , the equation

$$G(T, p) = \sum_{i \in \text{reaction}} g^i(c_i, T, p) \quad (3.6)$$

is defined such that $\frac{\partial g}{\partial c_i} = \mu_i$, where c_i and μ_i are the concentration and the molar chemical potential of i respectively. In the context of this work, i could represent nitrogen, vacancies or a nitrogen-vacancy complex. The sum of the chemical potentials denoted ΔG is referred to as the Gibbs free energy change of reaction. The form of each g^i in equation 3.6 is dependant on i and the complexity of the model. Even rather simple forms of g^i can be highly predictive provided they are supported by accurate DFT data. For instance, $g^i = c_i E - RTS$ where E is the molar internal energy of i calculated from DFT, and S is an appropriate expression for the entropy of i such as equation 3.5. Note that the pressure dependency of g^i is lost here, which is a common simplification to make when investigating solids because of their low compressibility factor and thermal expansion when compared to gases.

This construction is not unique to DFT studies. There are vast databases of g^i available for various i which are fitted statistically to experimental data [74]. Models of this nature have been employed successfully in industry for decades. However, the DFT approach is invaluable when investigating species where systematic experimental results are difficult to obtain. For instance, in the context of this work, vacancies are far more difficult to study through physical experimentation than with DFT modelling.

Example

The power of the Gibbs free energy construction is best understood by example. Consider the principal reaction in nitriding, the dissociation and subsequent dissolution of nitrogen in iron



Here, the square brackets $[\text{N}]$ denote that the nitrogen atom is dissolved in iron as an interstitial atom. For reaction 3.7 the sum in equation 3.6 has two g^i . One corresponds to nitrogen gas on the left hand side of the equilibrium and the other to dissolved nitrogen. The reaction will be in equilibrium when G is at it's minimal value, or equivalently when the Gibbs free energy change of reaction $\Delta G = 0$. This means that, at any temperature, the *equilibrium concentration* of nitrogen on either side of the equilibrium can be calculated by minimising G with respect to that

concentration.

The phase (crystal structure) of the metal will affect the form of g^i , that is, if i refers to nitrogen dissolved in α -Fe or γ -Fe. Supposing that the equilibrium concentrations are calculated for both of these phases at the same temperature, there are two corresponding minimal values of G . As always, nature seeks to minimise energy, so the iron phase with the lower G value is the stable phase at the chosen temperature. Using this principle, one can construct a phase diagram from first principles by varying the temperature over a desired range and calculating the stable phase in each instance.

3.2.5 Nitrogen Reference State

It is necessary to have a reference energy for nitrogen gas when performing equilibrium calculations on reaction 3.7. As usual the best practice is to apply the same DFT parameters to calculate the ground state energy of nitrogen gas as were used for nitrogen in iron, to benefit from the cancellation of systematic error (see 3.4). This seems counter-intuitive, as the plane-wave DFT methodology is intended for periodically repeating structures and not gas molecules. However, one only needs to expand the calculation cell until the periodically-repeated images are far enough apart to effectively be independent molecules. Various properties of nitrogen molecules such as bond length, cohesion energy (energy required to break the triple bond) and zero-point energy are well documented, so it is straightforward to validate the DFT calculations on the nitrogen molecule by checking if these values can be closely reproduced. However, this is purely useful for validation purposes, as there are better approaches (experimentally [75] and computationally) to calculate such quantities.

Nitrogen is assumed in this work to follow the ideal gas law, meaning that its Gibbs energy expression g^{N_2} can be readily obtained at relevant nitriding temperatures. Following the methodology of [71], one only requires the ground state energy and the vibrational modes of the nitrogen molecule to be calculated by DFT. In this case g^{N_2} will also depend on the nitrogen partial pressure p_{N_2} . This isn't the physical pressure in a nitriding atmosphere, but the theoretical nitrogen activity induced at the nitrided surface, from reaction 1.1 for instance. Hence, the p_{N_2} dependence can be reduced to a nitriding potential (see equation 1.2) dependence. Concretely, p_{N_2} can be expressed as

$$p_{\text{N}_2} = p_0 \left(r_{\text{N}} e^{A - \frac{B}{T}} \right)^2 \quad (3.8)$$

where p_0 is the reference pressure, and A and B are constants determined by

empirical data [3].

3.3 Diffusion Modelling

The thermodynamic model introduced in section 3.2 unlocks the capability to calculate quantities such as the stable phase and reactant concentrations at thermodynamic equilibrium. However, the concentration profile of nitrogen in the inner metal upon nitriding is kinetically controlled. The whole metal does not reach thermodynamic equilibrium with respect to the nitriding atmosphere, otherwise the metal would be too nitride-dense, meaning that a thermodynamic model alone is not sufficient. Nitrogen will become tied to any vacancies it encounters in the iron lattice as this is heavily favoured energetically. However, the concentration of nitrogen-vacancy complexes actually formed depends on how quickly the nitrogen can diffuse to reach the vacancies [5]. Kinetic data allows one to determine the penetration depth of nitrogen with respect to time, rather than just knowing its composition when equilibrium is eventually reached. This section outlines the necessary background required to follow the novel diffusion study of the iron-nitrogen-vacancy system, which forms chapter 5 of this thesis.

3.3.1 Elementary Diffusion Step

An investigation of nitrogen diffusion requires one to search for *transition sites* for nitrogen atoms as well as stable sites. The importance of the transition site can be seen by considering the energy surface of a nitrogen atom as it vibrates about a stable octahedral position (see figure 3.4). One can intuitively select the sensible transition path of the atom between stable octahedral positions, by following the path with the smallest energy gradients. In order for an atomic jump to occur, the diffusing atom will need to vibrate far enough along the transition path from its stable position that it does not fall back down the energy well to where it started. The position that defines *far enough* in this instance is exactly the transition site, where the energy gradient is zero and the atom will favour settling in both octahedral positions with equal likelihood. It does not matter what proportion of vibrations lie on the transition path, as only those that reach the transition state will allow for a transition between octahedral sites to occur.

The proportion of vibrations which reach the transition site can be calculated with a simple but powerful empirical equation, the *Arrhenius* law.

$$D = v \exp \frac{-(E_{\text{transition}} - E_{\text{stable}})}{RT} \quad (3.9)$$

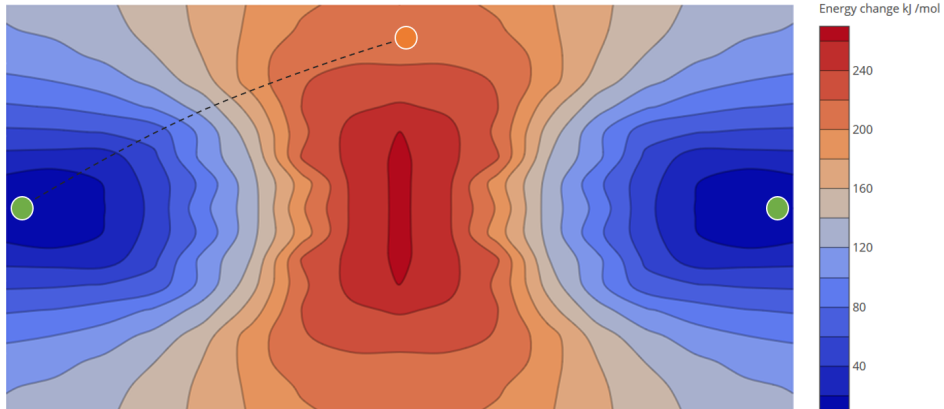


Figure 3.4: The map of potential energy change as a nitrogen atom traverse the space between two adjacent octahedral positions (green circles) in an FCC iron lattice. The minimum energy path for the nitrogen atom is indicated by the dashed black line, and the transition state is marked by an orange circle. The contour surface ranges from the stable low energy nitrogen positions (blue) to unstable high energy positions (red).

Where ν is the frequency of jump attempts, R is the universal gas constant, T is temperature and E_{stable} and $E_{\text{transition}}$ denote the energy at stable and transition states respectively. The quantity $E_{\text{transition}} - E_{\text{stable}}$ is often referred to as the *energy barrier/activation energy* for diffusion. In essence, equation 3.9 allows one to determine the jump rate of a nitrogen atom at any temperature. Both the energy barrier and ν can be calculated from DFT using well known methods. The energy barrier only requires the ground state energy at the transition state, whereas ν requires the calculation of vibration frequencies at the transition state (see section 3.2.1). In general, precisely calculating ν is far less important than precisely calculating the energy barrier. This is because it is a multiplicative factor rather than an exponential factor in equation 3.9, so it does not significantly affect the value of the jump rate over a temperature range. In solids the value of ν is does not vary significantly with the choice of atom, usually falling within the range $10^{12} \text{ Hz} < \nu < 10^{13} \text{ Hz}$ [49]. This means that it can always be reasonably approximated.

3.3.2 Nudged Elastic Band

The primary method of finding transition states and energy barriers for diffusion using DFT is by employing variations of the nudged elastic band (NEB) algorithm. NEB calculates the minimum energy path (MEP) using a series of images, where each image is a copy of the system with the jumping atom at a different point along

the path. In a MEP, the only forces acting on each image are following the path. NEB works by relaxation of a number of equally spaced images along the reaction path. The equal spacing between images are enforced by adding spring forces along the band between the images, parallel to the path of the jumping atom. The real forces which are calculated from DFT are projected to be perpendicular to the band, and these are used to progressively nudge the band into the correct path until the forces are sufficiently close to zero to consider the calculation converged. Starting locations for the images are chosen to enable the algorithm to approach the MEP. In order to obtain the correct path, the starting and ending images are fixed in their relaxed equilibrium positions throughout. Moreover, NEB converges more quickly and reliably if the initial positions of the band are close to the true MEP. Provided that the MEP follows a spatially intuitive path, such as in figure 3.4, a simple linear interpolation between the starting and ending images is usually an adequate choice for the initial positions. If required, there are relatively computationally cheap methods for improving on simple linear interpolation [76] for initial positions. The computational cost of NEB is substantial, because every image in the band; apart from the starting and ending images; is simultaneously relaxed to its ideal position on the MEP. Recent dynamic optimisation approaches have been shown to halve the number of NEB iterations [77].

The transition site for a jump between stable sites should lie on the MEP at the point of symmetry between the starting and ending images. However, there is no guarantee that one of the images from a finalised NEB calculation representing the MEP will be at the transition site. This is because a large number of images are required to discretise the reaction pathway finely enough for this to happen, which is computationally demanding. Despite this, the energy at the transition site is straightforward to interpolate. A continuous function is fitted to the NEB results, which outputs the energy at each distance along the reaction pathway. The maximum of this function is the energy at the transition site, which can be subtracted by the energy at the lowest image to obtain the energy barrier for diffusion (see figure 3.5). Alternatively, the transition site can be found explicitly by refining the calculation further with *climbing image* NEB [4] when it is close to the true minimum energy path. In the climbing image variant of NEB, the spring forces are removed from the image with the highest energy (which is therefore closest to the transition state), and it is pushed to higher energy positions until the maximum energy which maintains the band spacing is reached. One side of the NEB is compressed to achieve this, so the images are no longer symmetrical about the transition site (see figure 3.5).

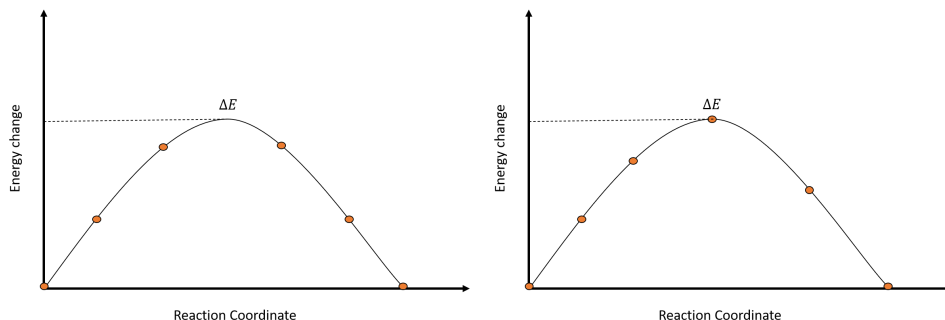


Figure 3.5: Examples of nudged elastic band (NEB) calculations. The left image represents standard NEB, and the right image represents the climbing image variant [4]. ΔE denotes the energy barrier for diffusion. The orange dots are data points calculated from NEB, and the black curves are fitted to the data.

3.3.3 Kinetic Monte Carlo

The jump rate (see equation 3.9) for an atom is closely related to the *diffusion coefficient*. In fact, if one is considering diffusion in an idealised lattice with a dilute (< 0.1 at.%) amount of jumping atoms, the diffusion coefficient and jump rate are effectively equivalent with both quantities depending only on temperature. For more complex cases, such as where the lattice has an excess of vacancies as well as interstitial nitrogen, the solution is not as straightforward. In this case, the jumping atom will diffuse at the vacancy-free rate when it is far away from a vacancy. But the rate will sharply change if it enters the proximity of a vacancy, and will further depend on whether the atom is jumping towards or away from it. To quantify this dynamic situation, kinetic monte carlo (KMC) [78] can be used to generate trajectories which incorporate the catalogue of different jump rates to find the overall diffusion coefficient under a set of conditions. Provided that one has the means to calculate all the relevant jump rates, KMC allows one to explicitly include this information in a kinetic simulation. Further, an array of KMC simulations can be performed where the conditions of interest (such as temperature and nitrogen/vacancy concentration) are varied, allowing one to fit the diffusion coefficient to these conditions [9].

The basic description of the KMC algorithm is relatively simple, although this is often improved upon in order to increase computational efficiency [79]. It requires a comprehensive catalogue of known independent jump rates as input, and will only give the correct result if these are correct. KMC works by increasing the simulation time at each step of the algorithm. In the rejection-free variant of KMC, a jump occurs at every step and the time increment is a function of the

probability that no jumping events have occurred in that increment. In essence, the time increment is the *waiting time* before each jump. While a jump is guaranteed to happen at each step, the jumps associated with slower rates are chosen less frequently than jumps with higher rates. For the purpose of investigating the effect of vacancies on nitrogen diffusion, using the rejection-free version of KMC is essential. This is because there is a large difference in the energy barrier of a nitrogen atom approaching a vacancy compared to leaving it. Due to the exponential term in 3.9, large differences between energy barriers for the various jumps will correspond to jump rates which differ by several orders of magnitude. Rejection KMC works by selecting jumping events uniformly, but only proceeding with carrying out the event with a probability proportional to its associated rate. Hence, like the rejection-free case, the jumps associated with higher rates are carried out more frequently than the jumps with smaller rates. However, if the difference in the rates are too large, the smaller-rate events will always be rejected in any reasonable amount of computation time. If a large proportion of jumps are rejected, then the convergence of the KMC simulation to the true dynamics of the system is slow.

3.3.4 Layer Growth Model

The preceding parts of section 3.3 have shown how the diffusion coefficient of a diffusing species can be obtained from first principles, which allows one to conveniently obtain the diffusion rate of the species in a range of temperatures and compositions. The final step to model surface treatment is to use the diffusion coefficient in a layer growth model, which is an instance of a class of methods referred to as *finite element models*. In the context of nitriding [30], each layer in the process will correspond with a nitride phase, and each of these need an expression for the condition-dependent diffusion coefficient. This work generates expressions for the diffusion coefficients in the α -Fe and γ -Fe phases from first principles. In contrast, diffusion coefficients are usually calculated by fitting experimental diffusion data. The goal in a layer growth model is to track the concentration of nitrogen and the size of the nitride layers as they form over time. To this end, the nitrogen concentration is defined as a function $c(x, t)$ of penetration distance perpendicular to the surface x , and elapsed time t . Given the diffusion coefficient of nitrogen $D(c(x, t), T)$, it is assumed that nitrogen atoms diffuse according to Fick's second law.

$$\frac{\partial c}{\partial t} = \frac{\partial}{\partial x} \left[D(c(x, t), T) \frac{\partial c}{\partial x} \right]. \quad (3.10)$$

In a single layer model where the diffusion coefficient is not dependent on

the concentration of the solute, the $c(x, t)$ which solves equation 3.10 can be written in an exact expression. For any realistic model of nitriding, an explicit analytical expression for $c(x, t)$ is not practical to find. Rather, equation 3.10 can be solved numerically to find $c(x, \hat{t})$ on an arbitrarily fine grid of discrete x values (which represent the finite elements), where \hat{t} is a diffusion/nitriding time of interest. To begin the layer growth simulation one would set a fixed nitrogen concentration at the surface, the first discrete x value, which is governed by the nitriding potential and maintained by equilibrium with the nitriding atmosphere. The concentration disperses into the material according to Fick's second law at each finite x element, over a series of time steps until the desired simulation time reaches \hat{t} . The iterative update formula applied to the concentration profile at each time step can be obtained by the finite-difference formulation [29]. The grid of the final $c(x, \hat{t})$ values is transformed to a hardness profile using standard conversion methods [23]. There are well established experimental methods, such as indentation and drilling, which can be used to calculate the hardness profile of a given nitrided metal. Hence, the layer growth model allows for validation of the multi-scale model used in this thesis, as it completes the link between the first principles calculations to applied metallurgy.

Chapter 4

Thermodynamic Model

4.1 Authors

The content of this chapter primarily consists of a reformatted journal article which was principally authored during the PhD period by the PhD candidate [5]. The authors of the journal article are as follows:

- **Aurash Karimi** Wrote the programming routines to perform the modelling calculations and carried them out. Perform tests and analysis to ensure the validity of the results. Wrote the manuscript and jointly constructed the figures with Michael Auinger.
- **Michael Auinger**: Formulated the original idea for the work. Provided supervision and scientific input to improve the quality of the manuscript and the presented results. Edited the writing to improve clarity and readability. Jointly constructed the figures with Aurash Karimi.

4.2 Summary

The thermodynamic results in this chapter required an extensive DFT study of the iron-nitrogen-vacancy system. Data resulting from the study is compared to values from literature. The convergence data from the calculations was used to measure the uncertainty in the results with respect to each plane-wave DFT parameter (see section 3.1.5). These are also included, as such details are a valuable reference point for future research. As described in the methodology, using the Gibbs energy construction (see section 3.2.4), the tabulated values can be used in a thermodynamic model to create profound insight into the nitriding process. This insight takes the

form of several figures which are readily understood by nitriding practitioners, and shows how vacancy-rich iron deviates from vacancy-free iron as the vacancy concentration increases. In particular, one has three variables to define the conditions of the nitriding process: temperature, nitriding potential (or nitrogen concentration) and vacancy concentration. Provided that two of these variables are known, the third variable can be inferred using the calculated data. Furthermore, if the amount of vacancies in both α -Fe and γ -Fe are known, one can identify which of the two phases is stable under the nitriding potential and temperature combination of interest.

4.3 Novel Contributions

Nitrogen is the second most common interstitial element in steel-making after carbon, so it is not surprising that a wealth of literature exists on the topic. With respect to DFT studies specifically, the thermodynamics of the iron-nitrogen-vacancy system has been explored for both α -Fe [42, 43] and γ -Fe [47, 48]. The former two papers employ the same model for α -Fe as is used in this work. In contrast, this work is unique in using a non-magnetic model for γ -Fe, which is more commonly modelled as anti-ferromagnetic. There is a general consensus in literature that octahedral sites in the proximity of vacancies act as trapping sites for nitrogen, which leads to the formation of complexes at thermal equilibrium in quantities far beyond that of lone vacancies. However, the current literature lacks quantified evaluations on the potential thermodynamic influences of nitrogen-vacancy complexes in an explicitly applied context, motivating the work that follows. Several factors outlined in this section mark this work as a distinct contribution to the existing literature.

4.3.1 Nitrogen-Vacancy Interactions

This work does not apply the common assumption that when vacancies are in excess, every vacancy will subsequently interact with nitrogen and form a complex. Although complex formation is highly favourable, nitrogen must be within close proximity (around three lattice points) to the vacancy before it is drawn to it. Hence, the rate-determining step of complex formation is interstitial nitrogen diffusion. In other words, the number of complexes that form are limited by the rate at which nitrogen can diffuse through the lattice to reach them. Because of this, the concentration of each nitrogen-vacancy complex is calculated using kinetic data generated by monte carlo simulations rather than by minimising the Gibbs free energy (such as in [47]).

4.3.2 Accuracy of Results

Plane-wave DFT calculations demand access to sufficiently large computing facilities. In general, computing facilities become more powerful and accessible over time. Therefore, modern DFT studies tend to have better refined results because of greater computing capability. The current work exemplifies this. In particular, a far greater energy cutoff (see section 3.1.5) was used in this work than in other literature. It is often the case that, due to systematic error cancelling (see section 3.1.7), a smaller energy cutoff is an appropriate compromise between computational burden and accuracy. However, it was shown that the error margin resulting from a smaller energy cutoff was around the same level as the uncertainty resulting from supercell size. The error margins for the other DFT parameters are negligible in comparison to energy cutoff and supercell size. Hence, the choice of energy cutoff was found to be an essential factor in the overall accuracy of the calculated results.

4.3.3 Repulsion energy

The class of thermodynamic models used in this work usually carry the assumption that the interstitial atoms are in small enough quantities that they do not interact with each other. This assumption begins to deviate from reality if the nitrogen concentration is larger than 0.5 at.%. In α -Fe, due to its low nitrogen solubility in most alloy compositions, this will rarely be the case. However, in γ -Fe this is an important consideration. To this end, a novel method is used to account for nitrogen-nitrogen interactions. By fitting the DFT convergence data with respect to supercell size, one can create a Gibbs free energy expression for nitrogen which depends on nitrogen concentration (see equation 4.16). This takes the form of an additional term in the Gibbs expression which, due to the repulsive behaviour of nitrogen atoms within an iron lattice, will increase the energy (decrease the stability) as the nitrogen concentration increases.

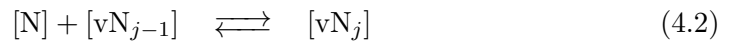
4.3.4 Presentation

There is a strong emphasis in the current work on the communication and presentation of data. It is designed to appeal to both DFT and metallurgical practitioners, which is a rare quality for a DFT study of this nature. Extensive calculations and discussion were not only used to validate the DFT calculations, but also put the work in the context of the real world. For instance, the work is the first to quantify the phase transition between α -Fe and γ -Fe from first principles to reproduce part of the well-known Lehrer diagram (see figures 4 and 5 in the article). Advances

like this should reduce the accessibility gap between first principles data and it's applications in the future. A goal which is further helped by providing comparisons between experimental data and model results where available.

4.4 Methods

Model Description and Notation The nitriding process is modelled by assuming that there is abundant nitrogen at the surface of an iron alloy (due to the high activity of nitrogen) which proceeds into the material via interstitial diffusion [32, 15]. Dissolved nitrogen may then interact with lone vacancies (denoted v) or nitrogen-vacancy complexes (denoted vN_j) where j is the number of nitrogen atoms within the complex. The process is governed by elementary reactions 4.1 and 4.2.



Let i denote chemical components of reaction 4.1 or 4.2 and $s \in \{\text{gas}, \alpha, \gamma\}$ be the state of i , which are diatomic gas, or interstitially dissolved within octahedral sites in either an α or γ phase Fe lattice respectively. $E_i^s(T)$ and c_i^s denote the internal energy and concentration of i in state s respectively. At absolute zero the internal energy E_i^s is defined as $E_i^s(0)$. At thermodynamic equilibrium with fixed temperature and pressure the concentrations are c_i^{seq} .

The rate at which nitrogen enters the proximity of a vacancy from the atmosphere, denoted $r_{\text{enter}}^s(T)$, is the forward rate at which reaction (4.1 & 4.2) proceeds. The rate-determining step of this reaction is assumed to be the interstitial diffusion of nitrogen to reach a vacancy, which is the forward reaction of 4.2, hence $r_{\text{enter}}^s(T)$ is considered to be approximately equal to the forward rate of 4.1. The opposing rate at which nitrogen leaves the proximity of a vacancy, denoted $r_{\text{leave},j}^s(T)$, is then a backward rate of reaction 4.2. Collectively, these rates define the distribution of nitrogen between complex sites, lone nitrogen defects and the gas state at a given temperature. $R = 8.314 \text{ J mol}^{-1} \text{ K}^{-1}$ is the universal gas constant which is used throughout this work.

4.4.1 Atomic Scale Modelling

DFT calculations were carried out with the projector augmented wave method as implemented in GPAW [66, 67]. The Perdew, Burke and Ernzerhof (PBE) exchange-

correlation functional [53] was used in all plane wave calculations. The atomic software library ASE [68] was used to interface with GPAW. Ferromagnetic (FM) body-centered cubic (BCC) Fe and non-magnetic (NM) face-centered cubic (FCC) Fe supercells are used as samples of α and γ phase Fe respectively. A full breakdown of parameters used in DFT calculations is given in tables 4.1 & 4.2.

Table 4.1: Parameter sets for the plane wave DFT calculations used in calculation of internal energies. Error and cut off energy values are given in eV. For temperature-dependent values, u is the maximum uncertainty over the largest temperature range used. u values of - are not explicitly calculated but are inferred to be small with respect to total error. Where u is written as a sum, the uncertainty comprises of constant-volume (left) and constant-pressure (right) considerations.

Energy	E_{cut}	u	supercell	u	kpts	u	u_{total}
E_{N}^{α}		0.003	$4 \times 4 \times 4$	0.013	$4 \times 4 \times 4$	0.014	0.030
$E_{\text{N}}^{\alpha}(T)$		-		$0.037 + 0.003$		-	0.040
E_{v}^{α}		< 0.001		0.004	$8 \times 8 \times 8$	< 0.001	0.004
$E_{\text{vN}_j}^{\alpha}$		0.003		0.055		0.008	0.066
$E_{\text{vN}_j}^{\alpha}(T)$	900	-		$0.037 + 0.019$		-	0.056
E_{N}^{γ}		0.003	$3 \times 3 \times 3$	0.018	$12 \times 12 \times 12$	0.001	0.022
$E_{\text{N}}^{\gamma}(T)$		-		$0.023 + 0.003$		-	0.026
E_{v}^{γ}		< 0.001		0.005	$6 \times 6 \times 6$	0.009	0.014
$E_{\text{vN}_j}^{\gamma}$		0.003		0.113	$12 \times 12 \times 12$	0.001	0.117
$E_{\text{vN}_j}^{\gamma}(T)$		-		$0.023 + 0.030$	$6 \times 6 \times 6$	-	0.053

Table 4.2: Parameter sets for the plane wave DFT calculations used in Nudged Elastic Band (NEB) calculations. The remaining uncertainty u in the resulting energy barriers for nitrogen jumps in iron lattices found for each parameter are given in eV. A u value of - is not explicitly known but inferred to be small with respect to total error. E_{∞}^s and $E_{x \rightarrow y}^{\alpha}$ denote vacancy-free and vacancy-containing supercells in the NEB respectively.

Energy	E_{cut}	u	supercell	u	kpts	u	u_{total}
$E_{x \rightarrow y}^{\alpha}$		< 0.001	$3 \times 3 \times 3$	0.009	$8 \times 8 \times 8$	-	0.010
E_{∞}^{γ}	500	< 0.001	$2 \times 2 \times 2$	< 0.001	$8 \times 8 \times 8$	-	0.001
$E_{x \rightarrow y}^{\gamma}$		< 0.001	$3 \times 2 \times 2$	0.035	$6 \times 8 \times 8$	-	0.036

The parameters which are chosen for each DFT calculation are the kinetic cut-off energy for plane-wave functions E_{cut} , the number of k-points distributed in the Brillouin zone using the Monkhorst-Pack method [64], the supercell size, and Methfessel-Paxton [65] (first order) smearing. The smearing width is set to 0.1 for all calculations. For non-smearing parameters, an estimate for the maximum residual uncertainty in output energy with respect to each parameter is considered.

E_{cut} and k-points are increased until there is < 0.02 eV residual uncertainty for each supercell size considered. Convergence with respect to supercell size requires case-specific treatment as it is the most sensitive trade-off of computational burden against accuracy. (see the closing paragraph of sections 4.4.1 and 4.4.1).

Internal Energies

Calculating $E_i^s(T)$ Let $\tilde{E}(\text{Fe}_n X)$ be the relaxed energy of a DFT supercell with n iron atoms and crystal structure s . Internal energies E_i^s , which can be considered to correspond to infinitely dilute point defects within the supercell approximation, are calculated using equations 4.3 to 4.5:

$$E_{\text{N}}^s = \tilde{E}(\text{Fe}_n^s \text{N}) - \tilde{E}(\text{Fe}_n^s) \quad (4.3)$$

$$E_{\text{v}}^s = \tilde{E}(\text{Fe}_{n-1}^s \text{v}) - \frac{n-1}{n} \tilde{E}(\text{Fe}_n^s) \quad (4.4)$$

$$E_{\text{vN}_j}^s = \tilde{E}(\text{Fe}_{n-1}^s \text{vN}_j) - \tilde{E}(\text{Fe}_{n-1}^s \text{vN}_{j-1}) \quad (4.5)$$

When X is a complex, the energy is dependant on location of the nitrogen atoms relative to the vacancy. In this case, E_i^s is set to the minimal energy found out of all candidate structures of X tested. The value of $E_{\text{vN}_j}^s - E_{\text{N}}^s$ gives the reaction enthalpy of reaction 4.2, which indicates the attractiveness of a complex containing j nitrogen atoms to a lone nitrogen defect. If the reaction enthalpy is large and positive then it is not energetically beneficial for nitrogen to migrate to form that size of vacancy. It is assumed in this work that generally, $E_{\text{vN}_j}^s - E_{\text{N}}^s$ increases with j for $j > 2$ (following assessments from literature [48, 42]). Based on this assumption the inequality

$$2 < n_{\text{N}}^{\text{max}_s} = j \text{ is the largest integer such that: } E_{\text{vN}_j}^s - E_{\text{N}}^s < 0.5 \text{ eV} \quad (4.6)$$

is used to set integer $n_{\text{N}}^{\text{max}_s}$ such that the maximum sized complex considered in a thermodynamic model still has a significant contribution to total nitrogen concentration relative to lone interstitial nitrogen. Complexes more containing more nitrogen atoms than $n_{\text{N}}^{\text{max}_s}$ then need not be considered.

Temperature dependence and zero point energy of E_i^s for each i containing nitrogen is assumed to primarily consist of vibrational contributions, where each nitrogen atom is approximated to behave as a three dimensional harmonic oscillator. Vibrational frequencies are calculated within a supercell representing i by making small

displacements to each nitrogen atom and using the resulting energies to assemble a Hessian matrix, resulting in a second order approximation of the force constants. This method was used as it is implemented in the ASE software library [68].

Convergence The degree of convergence of equation 4.3 with respect to (the number of iron atoms) n for both BCC ($n = 2, 16, 54, 128$) and FCC ($n = 4, 32, 108$) crystal structures in cubic supercells is observed with two approaches. In the more commonly used (and computationally cheaper) constant volume (CV) approach the lattice parameter is minimised using the smallest possible cubic supercell of iron and this lattice parameter is held fixed for each larger supercell. The constant pressure (CP) approach accounts for changes in supercell volume due to point defects by recalculation of the stable lattice parameter at each supercell size. The CV and CP values are two candidate values which can be equated to E_N^s , so the method which results in the smallest energy difference between the two largest considered supercell sizes is chosen as the final result. Furthermore, a quasi-harmonic approach where 4 sets of vibrational frequencies were calculated at 4 different supercell volumes about the energy minimum was used to determine the impact of thermal expansion on internal energies. The convergence behaviour of adding nitrogen to a complex in a supercell is assumed to be similar to adding a lone nitrogen defect to conserve computing resources, so nitrogen-containing supercells in equation 4.5 are only considered at a single volume. For n smaller than that used to determine the converged E_N^s , a more precise definition of equations 4.3 and 4.5 may be obtained by fitting the convergence data from the CV approach. Namely, an extra term

$$E_{\text{repulse}}^s(n) = a \frac{\log n}{n^3} + b \frac{\log n}{n^2} + c \quad (4.7)$$

is added to each equation, which outputs an estimate for the energy difference at n between the true internal energy and the converged 'infinitely dilute' supercell energy. In this study $E_{\text{repulse}}^s(n)$ is only calculated for lone nitrogen defects within α or γ (see table 4.3), otherwise $E_{\text{repulse}}^s(n) = 0$.

Table 4.3: Parameters for fitting equation 4.7, where the output energy may either be in eV or kJ mol⁻¹

defect		a	b	c	range
phase	species	kJ mol ⁻¹	kJ mol ⁻¹	kJ mol ⁻¹	
α	N	-2631	5564	-0.2332	$2 < n < 128$
γ	N	2298	2547	-0.6009	$4 < n < 108$

Rates of Reaction

Energy Barriers Nudged elastic band (NEB) [80] calculations were used to calculate energy barriers for nitrogen jumps between interstitial sites both with and without a vacancy present in the supercell. In all cases the NEB images are relaxed with the BFGS algorithm as implemented in ASE until the overall forces are less than 0.5 eV, then climbing image NEB [4] is used with the FIRE relaxation algorithm [81] until the forces are less than 0.025 eV. The energy barrier for a transition between adjacent stable octahedral positions is denoted by $E_{x \rightarrow y}^s$. Sites for nitrogen are defined by their distance from a vacancy, so that o_j^s is the j^{th} nearest neighbour to a vacancy. In the case of ideal crystals, each jump between sites is identical, so only one barrier $E_{\infty \rightarrow \infty}^s := E_{\infty}^s$ needs to be calculated. Close to a vacancy, there is far less symmetry between different sites, so at least one barrier should be defined for each j (see figure 4.1).

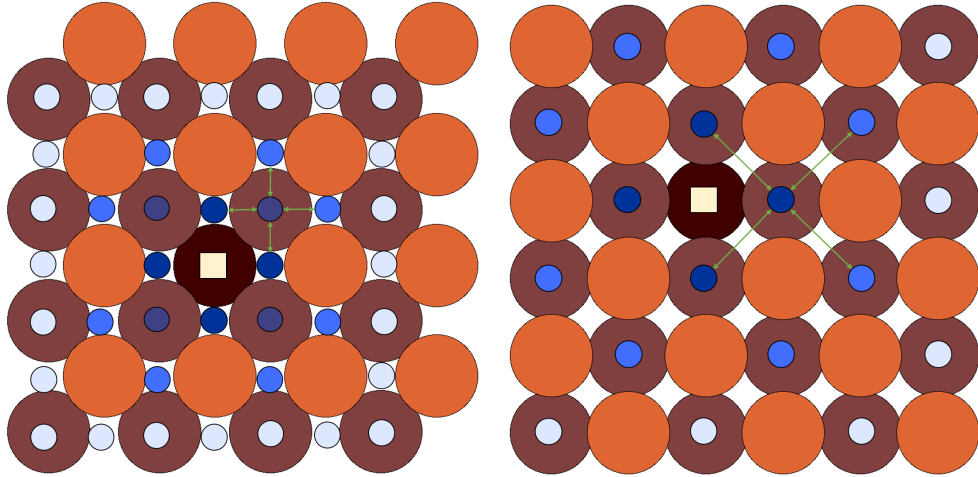


Figure 4.1: A two-dimensional cross section showing octahedral sites for nitrogen atoms (small circles) within α -Fe (BCC, left) and γ -Fe (FCC, right) lattices of iron atoms (large circles) in the proximity of a vacancy (yellow square). Green arrows represent the jumping directions for nitrogen atoms between sites, which are considered to happen with equal frequency if both ends of the arrow point to the same type of site (shade of blue). The small circles with the darkest shade of blue are the sites which are most influenced by the vacancy, whereas the lightest shade indicates sites which are far enough from the vacancy so that the energy barriers between them are not effected. Figure is reproduced from Karimi and Auinger [5] (2020).

Rates Reaction rates are defined in the form of

$$r_{\text{enter / leave}}^s(T) = e^{A - \frac{B}{RT}} \quad (4.8)$$

The jump rate of nitrogen from x to y is defined by the equation

$$r_{x \rightarrow y}^s(T) = v_{x \rightarrow y}^s e^{-\frac{E_{x \rightarrow y}^s}{RT}} \quad (4.9)$$

where $v_{x \rightarrow y}$ is the product of vibrational frequencies of nitrogen in the x position divided by the product of vibrational frequencies in the transition state. Due to symmetrical energy barriers in the ideal crystal, A and B values from equation 4.8 follow immediately from equation 4.9. For the non ideal case, the rejection-free variant of the Kinetic Monte Carlo (KMC) algorithm is used to generate trajectories which are used to adapt the asymmetrical jump rates (see table 4.4) in the proximity of a vacancy so that the net rate at which nitrogen leaves vacancies can be calculated. Nitrogen is evolved in a trajectory within a cubic simulation box which is made to be as small as possible while still containing every type of o_j^s site for which the energy barriers are calculated. The trajectories allow for the calculation of displacement of nitrogen over time at a given temperature. Over a calculated temperature range a linear fit is created from KMC results to calculate A and B .

Convergence The largest $m \times m \times m$ or $m+1 \times m \times m$ sized supercells which are possible within computational constraints are used during NEB calculations. In the cuboid supercells, the NEB calculation is oriented so that the largest distances between the initial and ending states are in the periodic $m+1$ direction to minimise symmetry. For a chosen m it is then necessary to decide the maximum number of o_j^s sites which can be considered. Considering more sites provides more energy barriers to calculate rates, but sites which are further away from the vacancy tend to have increased symmetry between periodic images, leading to a decrease in the accuracy of energy barriers. It is immediately clear that j should satisfy $j < \frac{m+1}{2}$, as larger j would result in overlapping site definitions when considering periodicity. It is also ensured that each j satisfies the inequality equation 4.10.

$$E_{j \rightarrow (j+1)}^s - E_{j \rightarrow (j-1)}^s > 0 \quad (4.10)$$

Equation 4.10 is based on previous findings that the energy barriers for nitrogen jumps are generally smaller for moving towards a vacancy than moving away from a vacancy. If the inequality is not satisfied, then it would appear that the influence of symmetry is large enough so that E_∞^s is closer to the true barrier than $E_{j \rightarrow (j+1)}^s$, so it is more beneficial to the calculation accuracy to treat the site as

uninfluenced by the vacancy.

Table 4.4: Energy barriers (kJ mol⁻¹) for the transition between octahedral positions (ordered by distance to a vacancy) for nitrogen in iron at absolute zero temperature. ∞ positions are deemed far enough from a vacancy that it no longer influences energy barriers.

		Destination			
		<i>o</i> ₁	<i>o</i> ₂	<i>o</i> ₃	<i>o</i> _∞
<i>α/δ</i> -Fe	Start				
	<i>o</i> ₁	-	103.3	-	-
	<i>o</i> ₂	33.0	-	72.5	-
	<i>o</i> ₃	-	48.0	-	74.50
	<i>o</i> _∞	-	-	70.29	70.29
<i>γ</i> -Fe	<i>o</i> ₁	-	252.7	-	-
	<i>o</i> ₂	192.1	218.2	-	218.2
	<i>o</i> ₃	-	218.2	-	218.2
	<i>o</i> _∞	-	218.2	-	218.2

4.4.2 Thermodynamic Model

Gibbs Free Energy At fixed temperature T and pressure p , the equation

$$G(T, p) = \sum_{(i, s) \in \text{reaction}} g(c_i^s, T, p) \quad (4.11)$$

is defined such that $\frac{\partial g}{\partial c_i^s} = \mu_i^s$, where μ_i^s is the molar chemical potential of i in state s . Thus, the derivative ΔG may represent the Gibbs Free Energy change (of reaction) for reactions 4.1 and 4.2. For the purposes of this work, the pressure dependency of equation 4.11 in the gas phase can be reduced to just a dependence on the nitrogen partial pressure p_{N_2} with reference pressure $p_0 = 1$ atm [3]. Ammonia is commonly used to create the high nitrogen activity required to dissolve nitrogen in iron in significant quantities. Thus, the partial pressure of nitrogen at fixed temperature can be expressed using the nitriding potential r_{N} . This is portrayed using the equation

$$p_{\text{N}_2} = p_0 \left(r_{\text{N}} e^{13.955 - \frac{6498.0}{T}} \right)^2 \quad (4.12)$$

which adapts the gas equilibrium data for ammonia from [3].

N_2 is treated as a linear ideal gas to calculate its temperature dependent Gibbs Free Energy from first principles using equation

$$g^{\text{gas}}(c_{\text{N}}^{\text{gas}}, T, p_{\text{N}_2}) = \frac{1}{2} c_{\text{N}}^{\text{gas}} \left[E_{\text{N}_2}^{\text{gas}}(0) - RT \left(S_{\text{other}} + S_{\text{translational}} \ln \left(\frac{p_{\text{N}_2}}{p_0} \right) \right) \right] \quad (4.13)$$

The entropy components denoted by S may be calculated from the vibrational frequencies of the nitrogen molecule. Configurational entropy of lone nitrogen defects dissolved within iron is defined by

$$S_{\text{config}}(c, k) = c \ln \left(\frac{c}{k} \right) + (k - c) \ln \left(1 - \frac{c}{k} \right) \quad (4.14)$$

Where c is the ratio of interstitial elements to iron atoms, and k is the number of interstitial positions per iron atom. Equation 4.14 may be used in a more general definition of configurational entropy for an arbitrary nitrogen and/or vacancy containing defect.

$$S(c_i^s, k) = \begin{cases} S_{\text{config}}(c, 1) & n_{\text{N}}^i = 0 \\ S_{\text{config}}(c, k) & n_{\text{v}}^i = 0 \\ S_{\text{config}}(c, 1) - c \ln \left(n_{\text{permute}}^{n_{\text{N}}^i} \right) & n_{\text{v}}^i = 1, n_{\text{N}}^i > 0 \\ 0 & \text{otherwise} \end{cases} \quad (4.15)$$

Where n_{N}^i denotes the number of nitrogen atoms within i , $n_{\text{v}}^i \in \{0, 1\}$ the number of vacancies and $n_{\text{permute}}^{n_{\text{N}}^i}$ is the number of energetically degenerate ways the n_{N}^i nitrogen atoms may be arranged within the defect. The molar Gibbs Free Energy for a defect with known internal energy (see section 4.4.1) is expressed by

$$g(c_i^s, T) = c_i^s \left(E_i^s(T) + E_{\text{repulse}}^s \left(\frac{1}{c_i^s} \right) \right) + RTS(c_i^s, k) \quad (4.16)$$

Under the considered range of conditions, the number of defects is not necessarily dilute with respect to the number of Fe atoms. The significant difference in internal energy caused by the repulsion of nitrogen atoms as the concentration increases past around 1 at.% is approximated by the E_{repulse}^s using fitted parameters (for each s) from table 4.3 (see section 4.4.1 for calculation details).

With equations 4.13 and 4.16, g is now defined for each possible i and s combination considered in this work where the defect is present in an arbitrary concentration.

Calculating $E_{\text{N}_2}^{\text{gas}}$ Total energy calculations of lone nitrogen molecules with an equilibrium bond length of 1.102 Å are performed within a $10 \times 10 \times 10$ Å bounding box, at cutoff energies from 500 up to 900 eV using a $12 \times 12 \times 12$ k-point grid. When

used within the thermodynamic model (see equation 4.13) the cutoff energy should match that which is used to calculate the internal energies, and in table 4.5 this is 900 eV, which renders the value of very insensitive to further cutoff energy increases. Vibrational frequencies are calculated (at a 900 eV cutoff only) in order to obtain the temperature dependence of E_2^{gas} in the ideal gas approximation using the formalism provided by the ASE software package, and the software is well documented so details of this are omitted. Using calculated vibrational frequencies, the value of the zero point energy (around 0.146 eV) obtained is in very good agreement with experimental data [75]. The calculated Gibbs Free Energy is also in strong agreement with the experimentally-obtained fit [82] over the temperature range considered in this work, with a maximal discrepancy of no more than $\pm 2 \text{ kJ mol}^{-1}$.

Molar Fractions If the concentration of each defect considered is known, one may calculate the molar fraction x_x^s of $x \in \{\text{N}, \text{v}\}$ using the equation

$$x_x^s = \frac{1}{1 + (c_x^{\text{seq}} + \sum_i^{n_x^i > 0} n_x^i c_i^s)^{-1}} \quad (4.17)$$

Calculating c_i^{seq} for each i is equivalent to solving the optimisation problem

$$\min_{c_i^s} G(T, p) \text{ subject to: } c_{\text{N}_2}^{\text{gas}} + c_{\text{N}}^{\text{seq}} = 1 \quad (4.18)$$

The constraint in equation 4.18 is physically motivated, with its purpose to ensure that the concentration of nitrogen available to facilitate reaction 4.2 is the exactly the amount removed from the atmosphere by reaction 4.1 per mole of iron present. Since the formation of the most abundant nitrogen-vacancy complexes is highly favourable if both reactants are in close proximity, it is assumed that the limiting aspect of their formation is the interstitial diffusion rate of nitrogen. Hence, diffusion (reaction) rates are used to determine the equilibrium concentrations of nitrogen-vacancy complexes as opposed to their internal energies. To this end $\hat{c}_{\text{vN}_j}^s$ is defined using the mass-action law applied to reaction 4.2 for successive j :

$$\hat{c}_{\text{vN}_j}^s = \frac{(r_{\text{enter}}^s)^j}{\prod_{m=1}^{m=j} r_{\text{leave}_m}^s} (c_{\text{N}}^s)^j \quad (4.19)$$

Let P_{v}^s be defined so that $P_{\text{v}}^s c_{\text{v}}^{\text{seq}}$ is the concentration of vacancies available for reaction 4.2. To investigate the thermodynamic behaviour that occurs when there are excess lone vacancies are present initially, but they aren't readily replenished while the system reaches a (meta)stable state, it should be the case that $\sum_j c_{\text{vN}_j}^s \leq$

$P_v^s c_v^{s\text{eq}}$. Thus, the equation

$$c_{vN_j}^s = \begin{cases} P_v^s c_v^{s\text{eq}} \frac{\hat{c}_{vN_j}^s}{\sum_j \hat{c}_{vN_j}^s} & P_v^s > 1 \\ c_v^{s\text{eq}} \hat{c}_{vN_j}^s & P_v^s = 1 \end{cases} \quad (4.20)$$

is used to obtain the concentration of each nitrogen-vacancy complex.

Phase Change The thermal stability of nitrogen within the α and γ phases relative to the reference state of nitrogen gas at fixed T and p_{N_2} is defined by

$$F^s(T, p_{N_2}, P_v^s) = g(c_N^s, T) + \sum_{j=1}^{n_N^{\text{max}_s}} g(c_{vN_j}^s, T) - g^{\text{gas}}(c_N^s + \sum_{j=1}^{n_N^{\text{max}_s}} c_{vN_j}^s, T, p_{N_2}) \quad (4.21)$$

Where $n_N^{\text{max}_s}$ corresponds to the maximum number of nitrogen considered for complexes in lattice s . Using equation 4.21 one may identify one of T , p_{N_2} , P_v^α or P_v^γ at which the α - γ phase transition occurs by fixing the other three. For example, to solve for a phase change temperature \hat{T} :

- Calculate $c_N^{\alpha\text{eq}}$ and $c_N^{\gamma\text{eq}}$ by applying 4.18 to the sum of equations 4.16 and 4.13.
- Calculate each $c_{vN_j}^s$ using P_v^s and $c_N^{s\text{eq}}$.
- \hat{T} is a root of the equation

$$F^\alpha(T, p_{N_2}, P_v^\alpha) - F^\gamma(T, p_{N_2}, P_v^\gamma) + \frac{1}{2}[2 - (x_v^\alpha + x_v^\gamma)](E_{\text{Fe}}^\alpha(T) - E_{\text{Fe}}^\gamma(T)) = 0 \quad (4.22)$$

where $E_{\text{Fe}}^s(T)$ is the molar Gibbs Free energy of pure Fe, adapted from [74] in this work.

4.5 Results and Discussion

4.5.1 Atomic Scale Results

The lattice parameters for ferromagnetic BCC and non-magnetic FCC iron were found to be 2.838 Å (= 0.2838 nm) and 3.461 Å (= 0.3461 nm) respectively, with negligible discrepancies for both lattice parameters within previous published DFT literature (see [42, 83] and [84, 47] respectively). In comparison to experimental

data [6], the lattice parameter for γ Fe at absolute zero is underestimated by non-magnetic FCC Fe by around 0.11 \AA ($= 0.011 \text{ nm}$), whereas the discrepancy for α Fe is $< 0.001 \text{ \AA}$ ($= 0.0001 \text{ nm}$). The more significant discrepancy in the γ case is not too surprising, austenite is known to be both paramagnetic and unstable at absolute zero temperature, both of which are not accounted for in the applied DFT methodology.

Internal Energy

Internal energies at absolute zero temperature calculated in this work are presented in table 4.5, along with total projected uncertainties with respect to convergence of DFT parameters. A large plane wave cutoff energy E_{cut} value was used in this work relative to other DFT publications (900 eV in this study and $500 \pm 100 \text{ eV}$ in others), which is predicted to correspond to discrepancies of around 0.05 eV (α) and 0.08 eV (γ) in nitrogen-containing defect energies between this work and other literature. There does not currently appear to be a widespread consensus within literature of k-points (relative to supercell size) as in the E_{cut} case, so it is more difficult to predict potential discrepancies in this case. However, halving the number of k-points in each cartesian direction as used in this work amounts to energy differences of at most around 0.1 eV , and the majority of k-point meshes used historically fall within this range. It is common to observe supercell sizes identical to those used in this study or one cubic degree larger (see [44, 48]), so the resulting discrepancies between this work and others due to supercell size should not exceed the uncertainty estimates in table 4.5. For E_{N}^{α} and E_{N}^{γ} , the uncertainties ($\pm 0.070 \text{ eV}$ and 0.048 eV respectively) are relatively insensitive to supercell size. This is because they were calculated using the computationally intensive approach of allowing the lattice parameter to vary at each supercell size. As seen in table 4.5, the uncertainty for internal energies of nitrogen complexed with vacancies can be several times higher, as they were calculated at fixed lattice parameters and are therefore more sensitive to supercell size. When calculation uncertainty in this work is combined with all the preceding considerations, most literature values fall within the anticipated range of values in this work, which amounts to around $\pm 0.2 \text{ eV}$ ($= 19.3 \text{ kJ mol}^{-1}$) on average.

Incorporating thermal expansion through the quasi-harmonic approach to calculate the temperature-dependant parts of internal energy was compared to calculating temperature-dependence at the energy minimising volume. Over the $523\text{-}1394 \text{ K}$ range there were maximum discrepancies of around 0.003 eV per atom for both α and γ . Furthermore, considering three volumes instead of four results in a discrepancy of the same order, so incorporating more volumes when fitting the

lattice parameter at each temperature was not considered necessary. The small discrepancy between the single and four-volume cases is due to very minimal lattice expansion found due to the vibrational energy of nitrogen ($< 0.001 \text{ \AA}$) over the temperature range for both α and γ).

It is noteworthy that in this work and other referenced DFT literature, both $E_v^\alpha = 2.22 \text{ eV}$ and $E_v^\gamma = 2.42 \text{ eV}$ are significantly overestimated by their experimental evaluations found with positron annihilation, which are $1.4 \pm 0.1 \text{ eV}$ and $1.7 \pm 0.2 \text{ eV}$ [85] respectively. This supports the earlier prediction of this work, which was that real alloys will have far larger vacancy concentrations than would be expected from idealised iron lattices at thermal equilibrium. Henceforth in this work it is set that $n_N^{\text{max}_s} = 3$, which satisfies equation 4.6 for both s . Due to the large increase in internal energy from $E_{vN_2}^s$ to $E_{vN_3}^s$ values, earlier assertions that complexes with 2 or less nitrogen atoms tend to be far more abundant than the more nitrogen-rich complexes appear to be true.

Rates of Reaction

The intuition that vacancies tend to trap diffusing nitrogen atoms appears to hold true in both α and γ Fe, with the vacancy having a particularly large effect on the barriers between o_1^s and o_2^s sites, causing them to deviate greatly from the ideal crystal activation energy E_∞^s . The maximum number of sites satisfying equation 4.10 was found to be 3 for the α phase and 2 for γ using $4 \times 3 \times 3$ and $3 \times 2 \times 2$ supercells. The difference in the value of $E_{1 \rightarrow 2}^s - E_{2 \rightarrow 1}^s$ between the two largest tested supercells is a good upper bound for uncertainty, as the closest barriers to the vacancy have the largest deviations from E_∞^s and hence the largest potential for error. The corresponding differences are 0.009 and 0.045 eV for the α and γ phases respectively, so the uncertainty holds some significance in the γ case. It appears that the higher symmetry in the o_2^γ position for the $2 \times 2 \times 2$ cell has caused a high variance in the supercell convergence between different barriers, by underestimating the energy minimum at o_2^γ and hence widening the energy barrier $E_{2 \rightarrow 1}^\gamma$. Therefore, a moderate increase in accuracy should be achieved in γ if a larger supercell size can be used within computing constraints. This indicates that while equation 4.10 is a good overall marker of how many energy barriers can be calculated for a given supercell, it does not necessarily ensure the energy barriers are precise to a level of experimental uncertainty ($< 0.01 \text{ eV}$). Between o_3^α and o_4^α sites the energy barriers do not deviate largely from E_a^α , which indicates that at this distance the effect of the vacancy on barriers is largely diminished. Thus, larger supercells to calculate barriers for further positions from the vacancy most likely need not be considered even if

Table 4.5: The calculated Internal energies at 0 kelvin of a singular nitrogen atom or vacancy in various point defects within iron, with corresponding uncertainty estimates and zero-point energies (of nitrogen only). The reference state for each internal energy is that of the full supercell containing the defect, and the tabulated value is the energy which remains (see equations 4.3-4.5) when a single nitrogen atom is left. For instance, considering the nitrogen-vacancy complexes, the associated internal energy is of the nitrogen atom which is added to form $E_{\text{vN}_j}^s$ from $E_{\text{vN}_{j-1}}^s$. Identified DFT literature sources are added for comparison, which are adjusted where required using $E_{\text{N}_2}^{\text{gas}}$ in this work so that all values share a common reference state. Abbreviations in parenthesis refer to magnetic states where the magnetism is different to that used in this work.

Defect	Energy		Uncertainty (\pm)				Zero-point Energy		Literature
	eV	kJ mol ⁻¹	eV	kJ mol ⁻¹	eV	kJ mol ⁻¹	eV	kJ mol ⁻¹	eV
$\frac{1}{2}E_{\text{N}_2}^{\text{gas}}$	-8.450	-815.1	-	-	0.146	14.1	-	-	-
E_{N}^{α}	-8.198	-791.0	0.070	6.75	0.0982	9.48	-8.13 [86], -8.43[83], -8.317 [44]		
E_{v}^{α}	2.22	214.2	0.004	0.39	-	-		2.12 [42]	
$E_{\text{vN}_1}^{\alpha}$	-9.080	-876.1	0.112	10.81	0.0894	8.63		-8.91 [42]	
$E_{\text{vN}_2}^{\alpha}$	-8.930	-861.6	0.112	10.81	0.0945	9.1		-9.02 [42]	
$E_{\text{vN}_3}^{\alpha}$	-7.863	-758.7	0.112	10.81	0.0998	9.63		-7.93 [42]	
E_{N}^{γ}	-8.768	-846.0	0.048	4.63	0.128	12.3		-8.609(AFMD) [48]	
E_{v}^{γ}	2.42	233.5	0.014	1.35	-	-		2.30 [47] 2.23 [84]	
$E_{\text{vN}_1}^{\gamma}$	-9.486	-915.2	0.170	16.40	0.129	12.5		-9.468 [47]	
$E_{\text{vN}_2}^{\gamma}$	-9.497	-916.3	0.170	16.40	0.126	12.1		-9.578 [47]	
$E_{\text{vN}_3}^{\gamma}$	-8.776	-846.7	0.170	16.40	0.120	11.6		-8.848 [47]	

computing resources are abundant. In the γ case, using a $2 \times 4 \times 3$ supercell which is quite taxing on computing resources still leaves too much symmetry to satisfy equation 4.10, as $E_{2 \rightarrow 3}^{\gamma} - E_{3 \rightarrow 2}^{\gamma} = -0.036$ eV with this supercell. Employing larger supercells to calculate these barriers may prove beneficial to accuracy, although it is not expected that the energy difference in barriers at o_3^{γ} would be as significant as the difference at o_3^{α} due to further distance from the vacancy in the γ case. Indeed, the slow supercell convergence is a sign that the true $E_{2 \rightarrow 3}^{\gamma} - E_{3 \rightarrow 2}^{\gamma}$ is relatively small in magnitude, as it is unable to outweigh the effect of symmetry even in relatively large supercells.

Table 4.6: Reaction rates calculated in this work as defined by equation 4.8. j indicates the number of nitrogen atoms in the associated complex. * indicates estimated errors deduced from similar calculations

Direction	Rate		A	B		Uncertainty (\pm)	
	phase	j		eV	kJ mol ⁻¹	eV	kJ mol ⁻¹
enter v	α	-	-5.624	0.727	70.1	0.010	1.0
	γ	-	-4.064	2.247	216.8	0.036	3.5
leave v	α	1	-1.990	1.734	167.3	0.019	1.8
		2	-1.990	1.574	151.9	0.019	1.8*
		3	-1.990	0.528	50.9	0.019	1.8*
	γ	1	-1.583	2.811	271.2	0.045	4.3
		2	-1.583	2.839	273.9	0.045	4.3*
		3	-1.583	2.062	198.9	0.045	4.3*

4.5.2 Thermodynamic Implications

Solubility

Idealised Iron The presence of lone nitrogen and vacancies within iron leads to the formation of complexes by reaction 4.2, and provided there is plentiful nitrogen available at the metal surface, increases the total fractions of nitrogen and vacancies in the system at equilibrium. It is seen from figure 4.2 that in both iron phases the total fraction of vacancies (equation 4.17) is heavily dependant on the nitriding potential and temperature, and many orders of magnitude above c_v^{seq} . This relationship agrees with findings in previous work [45] (α -Fe) and [47] (γ -Fe). The dependence on r_N is far stronger in the α case, showing that there is a stronger tendency to form complexes in this phase, which can also be surmised by comparing the internal energies.

The same does not hold for the total fraction of nitrogen, as an insignificant fraction of nitrogen dissolved within either Fe phase is contained in complexions with vacancies, compared to the amount of lone nitrogen interstitial defects. This is to be expected considering the definition of complex concentrations (equation 4.20), the product $c_v^{seq}c_N^{seq}$ tends to be far smaller than c_N^{seq} , but relatively close to c_v^{seq} . Indeed, for hydrogen [84], carbon [70] and previous (γ) nitrogen studies [47] the relationship found between the concentrations of interstitial elements, vacancies (at thermal equilibrium), and their complexes are very similar to the relationship discussed here. The calculated solubility of nitrogen at $p_{N_2} = 1$ atm up to the melting point of Fe is shown in figure 4.2 (left). In line with the previous comments, the fraction at equilibrium is almost entirely comprised of lone nitrogen interstitials, meaning that vacancies have little influence on nitrogen solubility at equilibrium. This matches

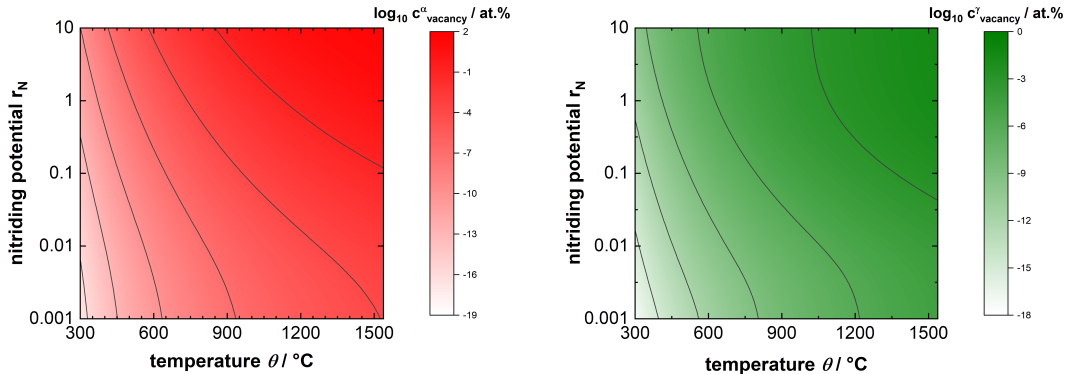


Figure 4.2: The fraction of vacancies in idealised α (left) and γ (right) iron when nitrogen-vacancy complexes as well as lone vacancies are considered. Note that the upper limit of vacancies reached under these conditions is lower in the γ case and this is reflected in the colour bar values. Figure is reproduced from Karimi and Auinger [5] (2020).

the conclusion from [42] for α -Fe whereas a similar explicit comparison for γ -Fe was not found. In comparison with experimental results (sourced from [6, 7]), there are underestimations in nitrogen solubility beyond the predicted uncertainties in the DFT results of up to an order of magnitude for both phases. If an idealised crystal may indeed be used to calculate the solubility of nitrogen at the same precision of experiments, then the underestimations in $E_N^s(T)$ would likely be due to unconsidered temperature-dependant effects. In a sensitivity analysis, a normal distributed error term $\sim \mathcal{N}(0, 10)$ was added to $E_N^s(T)$ (using the lower uncertainty bound energy value at $T = 0$) at evenly spaced intervals over the stable temperature ranges of each phase to create 10000 independent samples. This resulted in 6.84% and 14.5% of the sample solubility's for α and γ respectively exceeding a linear fit of experimental solubility results (on average over the temperature ranges), which corresponds to average over-estimations of internal energies of around 14.9 and 10.5 kJ mol^{-1} . While this magnitude of error is not impossible through systemic DFT errors, phonon energies and magnetic considerations which have not been accounted for in the model, the large and consistent (over both phases) overestimation of energy gives cause to investigate the vacancy-rich case.

Iron with Excess Vacancies Since vacancies tend to make the dissolution of nitrogen more favourable, the solubility of nitrogen increases when they are in excess. This relationship is depicted in figure 4.2 (right) for $p_{\text{N}_2} = 1 \text{ atm}$. It is observed that experimental α solubility values fall within $0.001 < c_V^\alpha < 0.1 \text{ at.}\%$ whereas for the

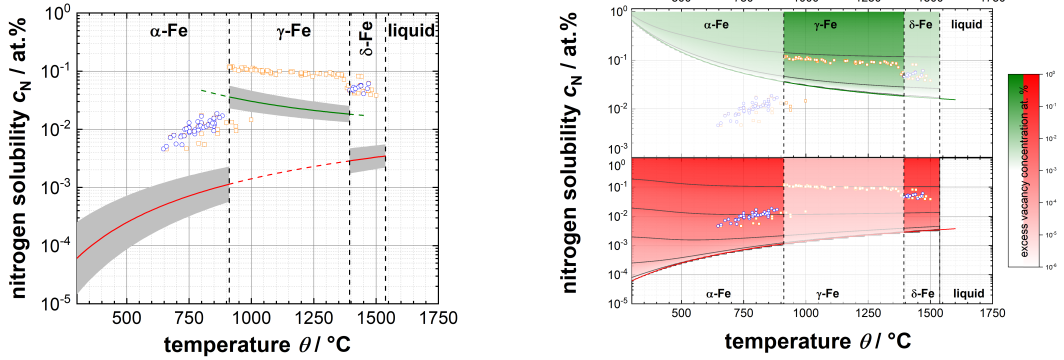


Figure 4.3: Solubility of nitrogen in iron at nitrogen partial pressure $p_{N_2} = 1$ atm. Experimental values are represented by blue circles [6] and orange circles [7]. In the left image, the solubility of nitrogen in ideal crystals as calculated by DFT is depicted for α (red line) and γ (green line) iron, and DFT calculation uncertainty is represented by the grey shaded area. Excess vacancies, represented by red and green contours, are added to α and γ respectively in the right image which increases the solubility of nitrogen above the value obtained from an ideal crystal calculation. Figure is reproduced from Karimi and Auinger [5] (2020).

γ and δ values $0.01 < c_v^\gamma, c_v^\delta < 0.1$ at.%. It appears almost all nitrogen atoms are contained within vacancies at higher temperatures. As the temperature increases, nitrogen is increasingly mobile and has the thermal energy to escape vacancy sites more easily so the trapping effect is weaker. This is observed concretely through the term $\frac{(r_{\text{enter}}^s)^j}{\prod_{m=1}^{m=j} r_{\text{leave}_m}^s}$ in equation 4.20, which tends towards 1 as $T \rightarrow \infty$. Particularly at higher temperatures, the expected proportion of excess vacancies appear to make up a substantial proportion of the metal, which may correspond to the large coverage of the metal interior by grain boundaries and other defects. One may make the observation that the number of excess vacancies predicted by experimental data in figure 4.2 tends to increase with temperature in the α phase. It appears that at lower temperatures nitrogen is less efficient at interacting with vacancies which are suggested to be available at higher temperatures. Finer grain boundaries and stronger vacancy traps could obstruct uniform access to all vacancies for nitrogen at low temperatures. Contrary logic would explain why there is a jump in predicted excess vacancies as iron transitions from the α phase to the γ phase. While diffusion in the γ phase is known to be slower in general, the traps are significantly weaker while the grain boundaries are coarser meaning diffusion directions should be less constrained by vacancies. Indeed, it is assumed that r_{enter}^s is equal the unhindered diffusion rate of nitrogen in the base metal, but in reality imperfections in the crys-

tal structure may inhibit nitrogen atoms from reaching more stable configurations because their access to available vacancies is restricted. At higher temperatures (around 912 °C), the variation of excess vacancy concentration with respect to temperature changes reduces sharply, indicating that available vacancies are utilised to a maximal value. This would explain both the higher variance in the predicted number of vacancies filled and the increased sparsity of experimental data in the α phase, as less vacancies are required to make relatively large changes to solubility.

Phase Stability

Idealised Iron As seen in figure 4.4, the α - γ phase boundary appears to resemble the line obtained from experimental data (FSstel accessed via FactSage [8]). Indeed, the the experimental data is almost within the predicted uncertainty range, suggesting that committing more computational resources to reduce this range would be beneficial. The calculated phase boundary shows better agreement with experimental data than the calculated nitrogen solubility's at $p_{\text{N}_2} = 1$ does. This is likely because the solubility results are underestimated for both phases, leading to consistent changes in energy for both phases in equation 4.21. While the calculated phase stability energies may be overestimated due to the lower solubility's, the consistency results in error cancelling in the phase boundary computation (equation 4.22).

If the $E_{\text{repulse}}(n)$ terms are included when calculating the phase boundary, at lower temperatures and larger r_{N} the calculated boundary diverges from the experimental data. This means that either the repulsion energy is significantly overestimated (in γ relative to α) by the constant-volume fit to $E_{\text{repulse}}(n)$ (see section 4.4.1), or there are significant contributions which are not accounted for in the (idealised crystal) model which counteract the resulting divergence from experimental data. Since the inclusion of the current $E_{\text{repulse}}(n)$ terms are not supported by the experimental data, they are omitted in the further results of this work. However, it is worth noting that it was calculated in this work and others [44] that constant-pressure DFT data converges significantly faster with respect to supercell size. Faster convergence would result in a flatter $E_{\text{repulse}}(n)$ function, which in turn would greatly reduce the repulsion energies. Hence, a $E_{\text{repulse}}(n)$ function fitted to constant-pressure may prove to be more promising.

Iron with Excess Vacancies Since nitrogen-vacancy interactions are energetically favourable, the α - γ phase boundary can become more favoured towards the α -phase or γ -phase (see figure 4.5) when vacancies are in excess in the respective phases. The thermodynamic model does not take into account the repulsion of nitro-

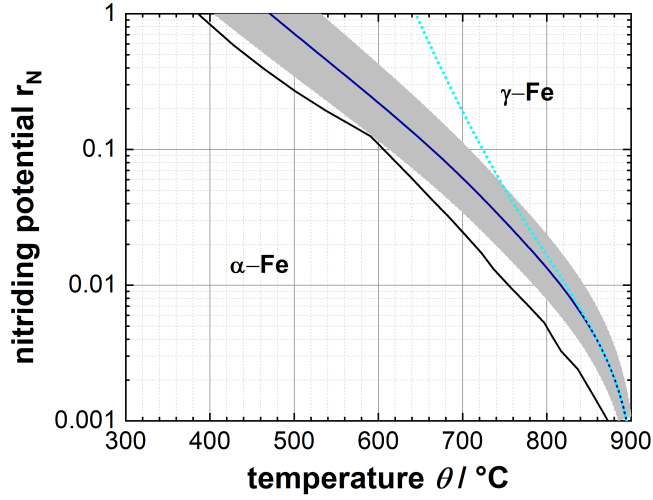


Figure 4.4: The calculated α - γ phase boundary in the iron-nitrogen system from first principles (blue line) and the calculation uncertainty range (grey area). Cyan dots show the same boundary calculated with estimated corrections for nitrogen repulsion. The black line is the corresponding boundary line from experimental data (sourced from the FSstel database accessed via FactSage [8]). Although in reality there are more stable iron-nitride allotropes in certain regions for the conditions featured, they are not included in this figure for conciseness. Figure is reproduced from Karimi and Auinger [5] (2020).

gen between complexes, meaning that the total nitrogen fractions within vacancies are expected to be overestimates when a substantial amount of the total nitrogen is contained within them and the total fraction of vacancies is large (> 1 at.%). The attraction of nitrogen-vacancy complexes between each other to form larger complexes, which competes with the repulsion of the contained nitrogen atoms is a relationship which is still under investigation in literature [47, 48, 42], so it is difficult to predict the point at which vacancy complexes will cease to form due to unfavourable repulsion (despite an abundance of vacancies and nitrogen). Nevertheless, the majority of regions in figure 4.5 (left) should not suffer significant inaccuracies from this, as the regions of the Lehrer diagram with high nitriding potential and temperature tend to contain the largest total fractions of vacancies (see figure 4.2).

Considering figure 4.5, following the contour surface edges to the bottom right, less vacancies are required to make a noticeable difference to the phase boundaries. Moreover, as can be seen in figure 4.6, the surface at the highest temperature (and accordingly, the lowest nitriding potential) is the least filled, as a larger range

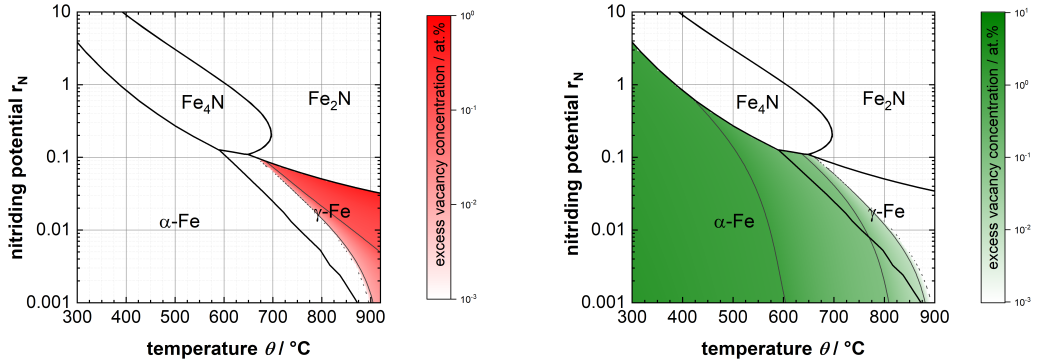


Figure 4.5: The concentration of excess lone vacancies required in nitrogen-containing α (red contours) and γ (green contours) iron, to shift the phase boundary and expand their respective phase within the Lehrer diagram. The edges of the contour surfaces (where they meet) represent the α - γ phase boundary for a theoretical ideal crystal, so they almost correspond (see figure 4.4) to the experimentally derived values for this boundary. All experimental data (Black lines) is sourced from the FSstel database accessed via FactSage [8]. This study was limited to the α and γ phases, but the ϵ (Fe_2N) and γ' (Fe_4N) regions are included to portray the results of this work in the wider context. Note that the colorbars between both graphs have different ranges of vacancy concentrations. Figure is reproduced from Karimi and Auinger [5] (2020).

of excess vacancies (with smaller concentrations) may alter the phase change temperature by over $250\text{ }^\circ\text{C}$. This effect is caused by the larger ratio of excess vacancies to dissolved nitrogen as the phase boundary enters the low nitriding potential and high temperature regions of the Lehrer diagram. That is, the nitrogen within the excess vacancies become an increasingly dominating fraction of the total nitrogen dissolved. The surfaces in figure 4.6 are more heavily covered by negative values rather than positive, meaning that in the instance where both phases are rich in vacancies, a larger γ phase region is favoured. There is consistently an overestimation of the α phase region by the vacancy-free calculation (see figure 4.4), which would indicate that a vacancy rich model. On the other hand, the temperature difference between the α - γ boundary calculated in this work compared to the experimental data by no more than $120\text{ }^\circ\text{C}$ (up to the triple point). It seems that with regard to the phase boundary, in contrast to calculations of nitrogen solubility, the ideal crystal can provide a moderately precise approximation to the experimentally obtained values, and the remaining discrepancies may be reduced further with more resource-heavy DFT computations. Indeed, the experimental boundary almost lies within the uncertainty range expected from DFT calculations. If uncertainty ranges

were reduced further, it would make the distinction between vacancy effects and DFT uncertainty clear.

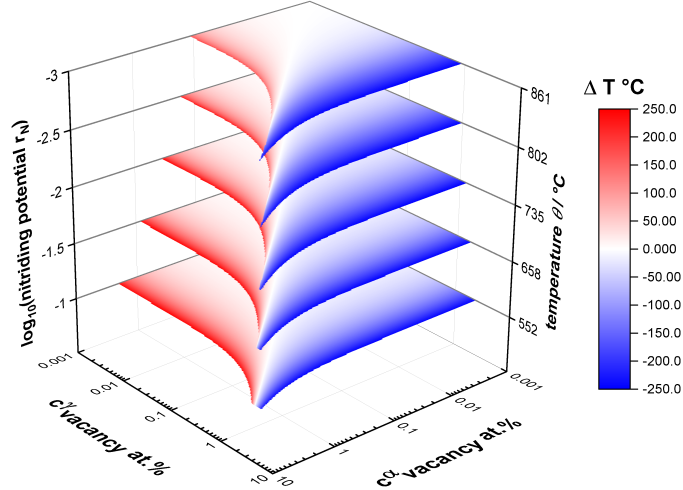


Figure 4.6: The change of the α - γ iron phase transition temperature (ΔT) in the presence of nitrogen and an excess vacancy concentration in both phases. Each surface represents an evenly spaced (with respect to $\log_{10}r_N$) point on the phase boundary which is calculated for ideal crystals (see figure 4.4), which are denoted on the vertical axes. The shift is made hotter ($\Delta T > 0 \text{ } ^\circ\text{C}$) by excess vacancies in α -Fe and colder ($\Delta T < 0 \text{ } ^\circ\text{C}$) for γ vacancies accordingly. For $\Delta T < -250 \text{ } ^\circ\text{C}$ or $\Delta T > 250 \text{ } ^\circ\text{C}$ the surface is left uncoloured for better visibility. Figure is reproduced from Karimi and Auinger [5] (2020).

4.6 Conclusion

Multiscale modelling was applied to calculate the thermodynamic properties of nitrogen in non-ideal iron lattices. This allows advancements towards bridging the gap between simulations from first principles and industrial applications. The α - γ phase boundary in the iron-nitrogen system was assessed from first principles and appears to complement current experimental observations. The phase boundary and nitrogen solubility have been quantified with an explicit dependence on vacancy concentration at conditions which are relevant to nitriding. Residual uncertainty from the DFT calculations in this work are carefully quantified, which allows error bounds for the calculated thermodynamic quantities to be set. Although DFT calculations are well converged relative to the current literature, due to the limitations of computing resources, the total uncertainties could not always be reduced to

the same level of experimental data, particularly with respect to nitrogen-vacancy complex energies. Despite this, it was determined that there is a credible case that vacancy-rich crystals are in fact more true to reality (than idealised lattices) for the thermodynamic quantities studied. The following points summarise this case and give cause for further investigation.

- It is a consistent finding in this work and other literature, that the vacancy formation energies of the α and γ phases are significantly underestimated in DFT-calculations, compared to experimentally derived values. This indicates that real alloys have far higher (excess) vacancy concentrations than predicted from idealised lattices.
- Nitrogen solubility is underestimated by considering idealised lattices in both phases, and these underestimations lie well outside of the expected uncertainty ranges for the calculations. It is detected following a sensitivity analysis that this is more likely to be due the effect of vacancies (and other crystal imperfections) rather than modelling artifacts. This is supported by experimental nitrogen solubility data, which suggest a large excess of vacancies to be present in real alloys, even for low nitrogen activities. This deviation may be the result of excess nitrogen at grain boundaries or other crystal imperfections.
- The experimentally derived temperature shift for the α - γ phase boundary (see figure 4.4) as a function of nitrogen activity is consistently overestimated in the absence of vacancies (i.e. assuming ideal lattices). While the discrepancy between experimental and calculated phase transition temperatures is relatively small and almost within the range of the predicted calculation uncertainty, the influence of vacancies is more pronounced in the austenite (γ iron) phase. As shown in figure 4.5, small concentrations of excess vacancies in austenite can have large effects on the phase transition temperatures, especially at higher temperatures and low nitriding potentials. Moreover, figure 4.6 shows that even when equal excess vacancy concentrations are present for both phases, the shift results in a larger austenite region. This indicates that excess vacancies could be responsible for the discrepancy between the calculated and experimental phase boundaries seen in figure 4.4.

Chapter 5

Diffusion Model

5.1 Authors

The content of this chapter primarily consists of a reformatted journal article which was principally authored during the PhD period by the PhD candidate [9]. The authors of the journal article are as follows:

- **Aurash Karimi** Wrote the programming routines to perform the modelling calculations and carried them out. Perform tests and analysis to ensure the validity of the results. Wrote the manuscript.
- **Michael Auinger**: Formulated the original idea for the work. Provided supervision and scientific input to improve the quality of the manuscript and the presented results. Edited the writing to improve clarity and readability.

5.2 Summary

This chapter required several new DFT calculations to add to the previous calculations from the thermodynamics chapter (see chapter 4). However, the bulk of the effort was to carry out an array of KMC simulations (see section 3.3.3). Firstly, a range of conditions; temperature, nitrogen concentration and vacancy concentration were decided. Each of these ranges were split evenly into discrete points, where every unique combination of points corresponds to a KMC simulation run. Subsequently, at each set of conditions, a diffusion coefficient for nitrogen was obtained. Interpolation was then used to calculate the diffusion coefficient between each of the discrete points. Furthermore, a fitted polynomial expression for both the α -Fe and γ -Fe matrix was used to capture the quantitative diffusion data in an easily

transferable form. This allows experimentalists to access quantitative data on the nitrogen diffusion coefficients as a function of nitrogen concentration c_N , vacancy concentration c_v and temperature T .

By their design, DFT calculations most accurately depict idealised (perfectly symmetrical) crystal structures, while industrial iron alloy grades inevitably contain numerous atomic-scale defects. There is evidence that this distinction between DFT and iron alloys in reality is significant when making thermodynamic predictions from first principles. For example, it was shown that DFT-calculated nitrogen solubility's in iron have closer agreement with experimental data when excess vacancies (see chapter 4) are introduced to idealised lattices. Thus, the diffusion of nitrogen is considered in both idealised and vacancy-rich BCC/FCC lattices. This work attempts to exhaustively consider the range of vacancy concentrations which would impact nitrogen diffusion in a meaningful way during heat treatment. However, experimental evidence is required to verify whether the levels of deformation (up to 10 at.% vacancies) which are considered occur in applied contexts.

5.3 Novel Contributions

In the literature regarding the diffusion of nitrogen atoms in vacancy-rich iron, energy barriers near vacancies have been calculated for both α -Fe [46] and γ -Fe [47]. To the authors knowledge there are no publications which employ a non-magnetic γ -Fe model as used in this work. Moreover, it was shown that the non-magnetic model of γ -Fe was effective at reproducing all available experimental data, provided that volume contributions were included. It is consistently found in literature that the energy barrier for a nitrogen atom leaving a vacancy is larger than the barrier going towards a vacancy, causing a net migration of nitrogen towards vacancies. In other words, there is a trapping effect which inhibits the free diffusion of nitrogen atoms when vacancies are present. However, there is not an empirically supported way to transform the energy barriers into a vacancy-dependent diffusion coefficient (see section 3.3.4) which can be used in nitriding models. Moreover, multi-nitrogen and multi-vacancy interactions also need to be considered. For example, in [46] (α -Fe) it was found that nitrogen-vacancy complexes containing more than two nitrogen atoms did not restrict the mobility of the nitrogen. Historically, it has been assumed for modelling purposes that the impact of vacancies on nitrogen diffusivity could be calculated as a function of the trapping enthalpy only. More recent approaches improve on this assumption by using multiscale modelling to incorporate more intricate details calculated from first principles [46, 87].

Many sources [83, 43] report that the energy barrier for nitrogen diffusion obtained by DFT calculations using ferromagnetic BCC iron has strong agreement to the low-temperature energy barrier obtained from experimental data for α Fe [10]. The situation is more challenging for γ Fe since it is both unstable at low temperatures (at high Fe purity) and most commonly thought to be paramagnetic, which are not readily incorporated features in DFT modelling. Anti-ferromagnetic FCC models are commonly used as they yield energy barriers close to that of solute-rich (expanded) austenite, which are typically around $0.8 \text{ eV} = 77.2 \text{ kJ mol}^{-1}$ [88, 3]. However, there is limited DFT literature which investigates the dilute-solute case, which is known experimentally to have a distinctly larger energy barrier for diffusion $1.74 \text{ eV} = 167 \text{ kJ mol}^{-1}$ [11]. Both nitrogen [47] and carbon [89] energy barriers are found to be consistently overestimated from DFT calculations using non-magnetic FCC iron, exceeding their experimental evaluations by more than $0.5 \text{ eV} = 48.2 \text{ kJ mol}^{-1}$. Discrepancies of this magnitude are peculiar, since at temperatures where austenite is in thermodynamic equilibrium, the magnetic contribution to diffusion energy barriers should be relatively small. To investigate, a non-magnetic FCC model which incorporates temperature dependent factors such as thermal expansion and vibrational energy is considered in this work. This work employs KMC simulations, which are calibrated using DFT-calculated energy barriers, to investigate the effect of vacancies on nitrogen diffusion under a range of conditions. Moreover, a novel method is used to endow the model with multi-nitrogen interactions. In particular, a nitrogen repulsion term is included in the KMC jump rate calculations. The previous thermodynamics work from chapter 4 is used to justify the omission of multi-vacancy interactions, and the limitations of the omission are examined in the article. The data generated from KMC simulations at the condition/composition range of interest was used to fit vacancy-dependent diffusion coefficients for nitrogen interstitials in iron. Diffusion coefficients are used in layer growth models [30] for nitriding (see section 3.3.4) and kinetic databases such as FactSage [8]. To the authors knowledge, this work features the first vacancy-dependent diffusion coefficient for nitrogen which is calculated from first principles or otherwise.

5.4 Methods

First principles data calculated as outlined in section 5.4.1 is used in combination with published data from [5] to calculate the jump rates for diffusion (see section 5.4.2) in BCC/FCC iron containing vacant lattice sites and interstitially

dissolved nitrogen. Section 5.4.1 features only new/essential details regarding the DFT methodology applied, the reader is referred to the previously published work mentioned for more detailed discussion. In particular, the energy barriers for nitrogen jumps in the proximity of a vacancy are quoted from [5] in table 5.2, which are needed to calculate the jump rates defined in equation 5.3. Using the calculated jump rates, an array of KMC trajectories are used to study the dynamics of the iron-vacancy-nitrogen system over the chosen temperature and nitrogen/vacancy concentration ranges. As detailed in 5.4.2, the data from trajectories are used to create polynomial expressions for the diffusion coefficient of interstitial nitrogen atoms.

5.4.1 First Principles Calculations

The projector augmented wave method as implemented in GPAW [66, 67], applying the exchange correlation functional [53] of Perdew, Burke and Ernzerhof (PBE), was used in for all DFT calculations. Atomic Simulation Environment (ASE) [68] was used to interact with the GPAW software. The parameters which are chosen for each DFT calculation are adapted from previous work [5]. These are the kinetic cut-off energy for plane-wave functions, the number of k-points distributed in the Brillouin zone using the Monkhorst-Pack method [64], the supercell size, and the width of Methfessel-Paxton [65] (first order) smearing. The smearing width is set to 0.1 for all calculations. All other DFT parameters, which were chosen from their convergence behaviour with respect to the two (ferromagnetic BCC and non-magnetic FCC) Fe systems of interest, are specified in table 5.1. The uncertainty estimates are calculated by summing together the residual error margins of the cut-off energy, the supercell size, and the number of k-points. The residual error margins are calculated as the energy difference between the last two iterations of the convergence test for each DFT parameter with respect to the calculated DFT energy.

Table 5.1: Parameter sets used for all plane wave DFT calculations in this work, for supercells of BCC/FCC Fe containing nitrogen and/or vacancies. The estimated uncertainty in energy barriers calculated using these parameters is included from [5].

Lattice	E_{cut} (eV)	Supercell Size	K-points	Uncertainty (eV)
BCC (ferromagnetic)	500	$3 \times 3 \times 3$	$8 \times 8 \times 8$	0.010
FCC (non-magnetic)		$3 \times 2 \times 2$	$6 \times 8 \times 8$	0.036

The Nudged elastic band (NEB) [80] method was used to calculate minimum energy pathways (and subsequently the energy barriers) for nitrogen and iron atoms

transitioning between interstitial sites and lattice sites respectively. In all cases the NEB images are relaxed with the Broyden-Fletcher-Goldfarb-Shanno (BFGS) algorithm as implemented in Atomic Simulation Environment [68] (ASE) until the overall forces were less than 0.5 eV, then climbing image NEB [4] is used with the FIRE algorithm [81] until the forces are less than 0.025 eV.

Using the location of transition states which are obtained using NEB results, the volume dependencies of energy barriers for nitrogen are calculated by fixing two iron atoms in supercells containing nitrogen in both transition and octahedral positions. The supercells are held at fixed volume over a range of evenly spaced lattice parameters up to 5.46% (BCC) and 4.70% (FCC) larger than their (DFT calculated) equilibrium values. At each volume, the supercell is relaxed with BFGS.

Vibrational frequencies are calculated for the nitrogen atom in octahedral and transition sites, where it is treated as an independent three-dimensional harmonic oscillator. The nitrogen atom is displaced by 0.01 Å in six Cartesian directions to assemble a Hessian matrix using the central differences method. Three frequencies are calculated, which are used in equation 5.1 to calculate the temperature-dependent Helmholtz energy $E(T)$ from the corresponding ground state energy E :

$$E(T) = E + E_{\text{zpe}} + \sum_i^{i=3} k_{\text{B}} T \ln \left(1 - e^{-\frac{\epsilon_i}{k_{\text{B}} T}} \right) \quad (5.1)$$

Where the ϵ_i are the energy associated with each vibrational frequency, E_{zpe} is the zero-point energy and k_{B} is the Boltzmann constant. The volume dependence and the vibrational frequencies are calculated using the same DFT parameters which were used in NEB calculations (see table 5.1). It was assumed that calculating volume dependence and vibrational frequencies for vacancy-containing supercells is not impactful enough in diffusion modelling to justify the computing resources required, so only the ideal (vacancy-free) case is considered for these contributions.

The repulsion energy of diffusing nitrogen atoms $E_{\text{N-N}}$ is approximated using the nitrogen binding energy of a supercell containing two neighbouring nitrogen atoms. Let $\tilde{E}(X)$ denote the ground state energy of X calculated in a DFT supercell, then:

$$E_{\text{N-N}} = \tilde{E}(\text{Fe}_n\text{N}_2) - \tilde{E}(\text{Fe}_n\text{N}) - \frac{1}{2} \tilde{E}(\text{N}_2) \quad (5.2)$$

where n is the amount of iron atoms in the supercell.

5.4.2 Diffusion Model

Jump Rates

The energy barrier for a diffusing species x with an interacting neighbour species y to jump to a new stable position is denoted by $E_{y(i \rightarrow j)}^x$, where the old (pre-jump) and new position of x are i 'th and j 'th nearest neighbours to y . In this work only nitrogen and vacancies are considered, so $x, y \in \{N, v\}$ where "v" denotes a vacancy. The third ($i, j < 4$) and second ($i, j < 3$) nearest neighbours are the farthest interactions considered for BCC and FCC Fe respectively, as these constraints are considered to be a good compromise between computational burden and accuracy [5]. The nearest neighbour positions and jump paths for a nitrogen atom in the proximity of a vacancy are shown in figure 5.1. The isolated and dilute energy barrier is denoted $E_{y(\infty \rightarrow \infty)}^x := \Delta E^x$, where x is the diffusing species. In the FCC crystal, it is approximated that $E_{v(2 \rightarrow 2)}^N = \Delta E^N$. This is because the vacancy is too far away to have a significant effect on the energy barrier for the $2 \rightarrow 2$ jump [5]. The variant of KMC used in this work does not efficiently simulate diffusion within deep energy basins i.e. the FCC $1 \rightarrow 1$ jump. Whilst modifications to the KMC algorithm have recently been demonstrated to accelerate convergence in this situation [90, 91, 92], the FCC $1 \rightarrow 1$ jump is omitted in the present diffusion simulations. As detailed in section 5.5.4, the contribution of the $1 \rightarrow 1$ jumps to the calculated macroscopic diffusion coefficient of nitrogen is small enough to justify their omission.

A jump rate $r_{y(i \rightarrow j)}^x$ of x is defined for each unique energy barrier of x at temperature T by the equation

$$r_{y(i \rightarrow j)}^x(V, T) = \nu_x e^{-\frac{E_{y(i \rightarrow j)}^x(V, T) + E_{N-N}^*(x)}{RT}} \quad (5.3)$$

$$E_{N-N}^*(x) = \begin{cases} [\text{Number of nearest-neighbour} \\ \text{N adjacent to jump destination}] \times E_{N-N} & x = N \\ 0 & \text{otherwise} \end{cases} \quad (5.4)$$

Where $R = 8.314 \text{ J mol}^{-1} \text{ K}^{-1}$ is the universal gas constant. Experimental data [72] of lattice expansion with respect to temperature is combined with calculated data of energy barriers at expanded supercell volumes (see section 5.4.1), to account for the impact of thermal expansion on nitrogen diffusion. Consequently, the volume dependence of each $E_{y(i \rightarrow j)}^N(V, T)$ used in equation 5.3 is reduced to a temperature dependence in practice. Moreover, $E_{y(i \rightarrow j)}^N(V, T)$ contains the tem-

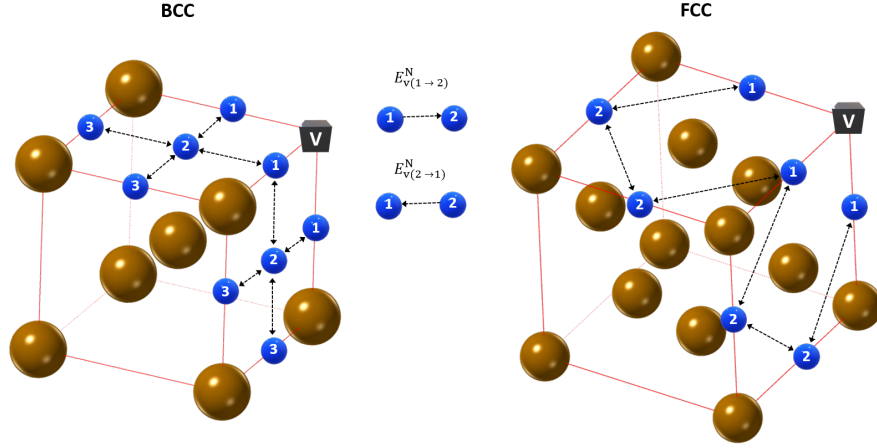


Figure 5.1: Jump paths (black arrows) and interstitial positions (blue spheres) for a nitrogen atom in nearest neighbour positions around a vacancy (grey cube) in BCC and FCC lattices. A numbering of i indicates that an interstitial position is an i 'th nearest neighbour to the vacancy. $E_{v(i \rightarrow j)}^N$ denotes the energy barrier for nitrogen to jump from an i position to a j position. Figure is reproduced from Karimi and Auinger [9] (2021).

perature dependent vibrational contributions shown in equation 5.1. The attempt frequency of nitrogen jumps ν_N is calculated from DFT, by dividing the product of vibrational frequencies of nitrogen in an octahedral site by the product of the vibrational frequencies in the corresponding tetrahedral transition site (omitting the weakest frequency at the tetrahedral site). The $E_{N-N}^*(x)$ term defined in equation 5.4 is used to account for nitrogen repulsion. The repulsion energy adjusts the rate at which nitrogen atoms jump to a nearest neighbour position of other nitrogen by the proportion of paired N-N complexes relative to lone nitrogen interstitials at equilibrium (see equation 5.2). Due to the way it is defined, the repulsion contribution only applies when nitrogen has a candidate jump which is already the nearest neighbour to one or more other nitrogen atoms. Furthermore, if the jump is in the range of a vacancy, it is approximated that the vacancy does not influence the repulsion energy.

To calculate the jump rate $r_{y(i \rightarrow j)}^x$ for each x to jump from its current position to a candidate position, the nearest neighbour distances of both positions to the closest y are considered. For example, suppose $x = N$ and $y = v$. If the closest vacancy to the nitrogen atom in its current position is a second nearest neighbour ($i = 2$) and the candidate position is a first nearest neighbour to the vacancy ($j = 1$), then the rate for nitrogen to jump to the candidate position is given by $r_{v(2 \rightarrow 1)}^N(T)$.

Diffusion Coefficient

At temperature T , the interstitial diffusion coefficient D^s of nitrogen atoms dissolved in iron containing vacancy and nitrogen concentrations of c_v and c_N respectively, is defined for considered phases of iron $s \in \{\alpha, \gamma\}$ by the equation

$$\ln(D^s(T, c_v, c_N)) = \sum_{k=0}^{k \leq 3} a_k^s \left(\frac{1}{T}\right)^k. \quad (5.5)$$

By employing the jump rates which are calculated as outlined in section 5.4.2, the KMC algorithm as implemented in [79] is used to generate trajectories of mobile nitrogen atoms within $25 \times 25 \times 25$ supercells of BCC Fe (31 250 atoms) and FCC Fe (62 500 atoms). Let T_m , c_{vm} and c_{Nm} represent the fixed conditions of the KMC supercell for each independent and unique trajectory, indexed by m . Let $x_n(t)$ denote the position of nitrogen atom n at time t within a KMC simulation cell containing a total of N mobile nitrogen atoms. The value of the diffusion coefficient (equation 5.5) for each m is given from a KMC trajectory by calculating the mean squared displacement (MSD)

$$\mu_N(t, T_m, c_{vm}, c_{Nm}) = \sum_{n=1}^N \frac{|x_n(t) - x_n(0)|^2}{N}. \quad (5.6)$$

Where

$$D^s(T_m, c_{vm}, c_{Nm}) = \lim_{t \rightarrow \infty} \frac{\mu_N(t, T_m, c_{vm}, c_{Nm})}{6t}. \quad (5.7)$$

The evolution of the MSD (equation 5.6) as time passes in the KMC trajectory is calculated in 200 evenly spaced time increments, using the method detailed in [93]. The dissolved nitrogen concentration in the KMC supercell is held fixed at either $c_{Nm} = 0.1$ at.% or 1.0 at.%, and the vacancy concentration is chosen at discrete points from the range $0.01 \text{ at.\%} < c_{vm} < 10 \text{ at.\%}$. For each unique combination of c_{vm} and c_{Nm} considered, 48 KMC trajectories consisting of 2.5×10^6 KMC steps are generated at temperatures which are evenly spaced over the range $\frac{1}{227^\circ\text{C}} > \frac{1}{T} > \frac{1}{1538^\circ\text{C}}$. The MSD from the last time increment of each trajectory is used to calculate the diffusion coefficient using equation 5.7. The diffusion coefficient is also calculated using the MSD from the second-to-last time increment and the MSD after the first half of KMC steps have executed. To ensure that the trajectories are properly converged, it is checked that the logarithm of each of the three calculated diffusion coefficients (in cm^2s^{-1}) differ by no more than 0.05. The KMC supercells are initially populated with nitrogen and vacancies in randomised

positions. The first 20% of KMC steps are not included in MSD calculations, to allow time for the nitrogen atoms to approach their equilibrium configurations.

The data generated from the trajectories are used to fit equation 5.5 using least-squares regression, resulting in a calculated set of a_k^s expressions. If the fitted diffusion coefficient is only dependent on temperature, thus corresponding to a fixed c_{Nm} and c_{vm} pair, the a_k^s are constants. Otherwise, the a_k^s are polynomial expressions of c_N and c_v , each comprising of a set of coefficients which are fitted. Lower-order polynomials are favoured in equation 5.5 for simplicity and prevention of over-fitting, so all a_k^s where $k > 1$ are set equal to zero unless including higher-order terms would reduce the total squared error by 20% or more. Piecewise log-linear interpolation is used to aid the visualisation of calculated results. For example, suppose that two sets of a_k^s parameters are calculated by fitting equation 5.5, using a set of KMC trajectories which span the temperature range, at two corresponding vacancy concentrations $c_{v1} = 0.1$ at.% and $c_{v2} = 1$ at.%. Provided the nitrogen concentrations are the same in all the KMC supercells, both fits are only dependent on temperature. Let $D_1^s(T)$ and $D_2^s(T)$ denote the value of the two fits at temperature T . At any temperature, say $T = 500$ K, the logarithm of the diffusion coefficient is calculated for any $0.1 \text{ at.\%} < c_v < 1 \text{ at.\%}$ by the expression $\frac{\log[D_1^s(500)] - \log[D_2^s(500)]}{\log(0.1) - \log(1)}(\log(c_v) - \log(0.1)) + \log[D_1^s(500)]$. The reader is referred to section 5.5.5 for a generalised version of this example.

5.5 Results and Discussion

5.5.1 First Principles Results

Ground State Energies

All relevant energy values at the ground state are summarised in table 5.2. Moreover, the energy barriers for nitrogen to jump between neighbouring octahedral sites are visualised in figure 5.2a. These values are for constant-volume BCC Fe and FCC Fe, with lattice parameters of 2.838 \AA ($= 0.2838 \text{ nm}$) and 3.461 \AA ($= 0.3461 \text{ nm}$) respectively. In vacancy-free BCC Fe the energy barrier was found to be $70.29 \text{ kJ mol}^{-1}$. This value shows fair agreement with other NEB ($69.47 \text{ kJ mol}^{-1}$) [83], semi-empirical molecular dynamics ($75.26 \text{ kJ mol}^{-1}$) [94] and experimental evaluations (ranging from 70 to 80 kJ mol^{-1}) [10, 36, 95]. In vacancy-free FCC Fe the calculated energy barrier was found to be $218.2 \text{ kJ mol}^{-1}$, but both computational and experimental comparisons are scarce. No documented values were found in literature for comparable NEB calculations using non-magnetic FCC Fe. Semi-empirical molecu-

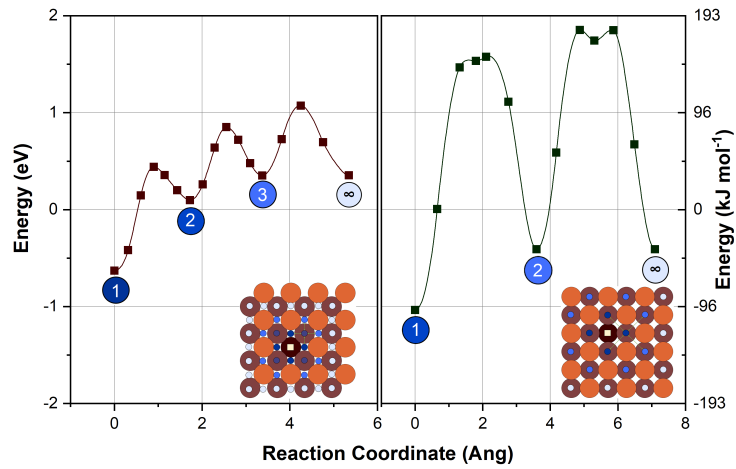
lar dynamics has previously reported a barrier of (131.2 kJ mol⁻¹) [94], which is very far from the NEB value. The most recent experimental evaluation reports a barrier of 167.9 kJ mol⁻¹ [11], which does not show good agreement with either of the two computationally obtained values. However, as detailed in section 5.5.1, taking into account the impact of lattice volume on the DFT-calculated energy barrier results in far closer agreement with the experimental data. Definitive conclusions can not be made about nitrogen diffusion in the presence of vacancies by only considering the $E_{y(i \rightarrow j)}^N$ energy barriers for the individual jumps, and there are no $E_{y(i \rightarrow j)}^N$ values in literature to compare with. However, figure 5.2a suggests that vacancies form traps for diffusing nitrogen atoms in both phases of iron. This is because the energy barriers for nitrogen to move away from a vacancy $E_{v(i \rightarrow i+1)}^N$ are larger than the reverse jump towards the vacancy $E_{v(i+1 \rightarrow i)}^N$ in all instances.

Table 5.2: First principles calculation results for interstitial nitrogen and vacancies in ferromagnetic BCC iron and non-magnetic FCC iron. E_{N-N} is the binding energy for nitrogen atom pairs. $E_{v(i)}^N$ is the binding energy for nitrogen atoms which are i 'th nearest neighbours to a vacancy. ΔE^x is the interaction-free energy barrier for x to jump between neighbouring stable positions. $E_{v(i \rightarrow j)}^N$ is the energy barrier for a nitrogen atom to jump from an i 'th to a j 'th nearest neighbour position with respect to a vacancy, and the corresponding energy at the transition site for the jump is denoted $E_{\min(i,j)}^{\text{TS}}$. All values are recorded in kJ mol⁻¹. Energy barrier data was reproduced from Karimi and Auinger [5].

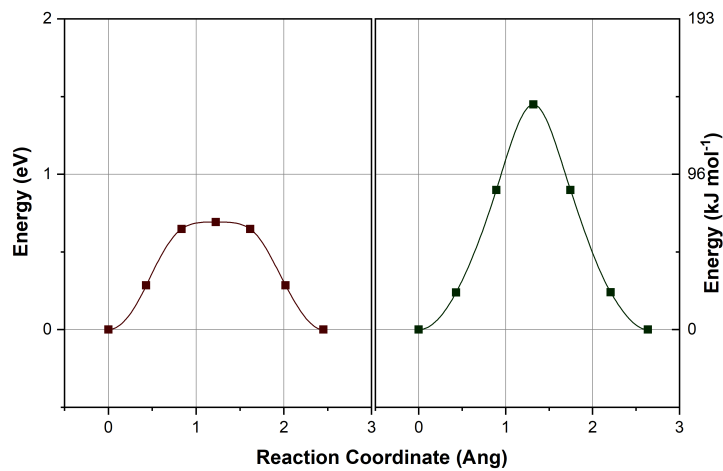
Lattice	E_{N-N}	$E_{v(1)}^N$	$E_{v(2)}^N$	$E_{v(3)}^N$	$E_{v(\infty)}^N$	E_1^{TS}	E_2^{TS}	E_∞^{TS}		
BCC	68.62	-60.84	9.50	34.00	34.12	42.45	82.02	104.40		
FCC	19.04	-100.01	-39.45	-	-39.44	152.71	-	178.70		
			ΔE^v			$E_{v(1 \rightarrow 2)}^N$	$E_{v(2 \rightarrow 1)}^N$	$E_{v(2 \rightarrow 3)}^N$	$E_{v(3 \rightarrow 2)}^N$	ΔE^N
BCC			66.83			103.29	32.95	72.52	48.02	70.29
FCC			139.80			252.72	192.16	-	-	218.20

Comparing figures 5.2a and 5.2b indicates that lone vacancies will migrate at a similar rate to lone nitrogen atoms in BCC Fe, as the calculated ΔE^N and ΔE^v values are within 10 kJ mol⁻¹ of each other. In contrast, it appears that vacancies are substantially more mobile than nitrogen in the FCC lattice as ΔE^v exceeds ΔE^N by almost 100 kJ mol⁻¹.

The nearest-neighbour repulsion energies of nitrogen E_{N-N} were found to be 68.62 kJ mol⁻¹ and 19.04 kJ mol⁻¹ for BCC Fe and FCC Fe respectively. Since E_{N-N} was found to be positive for both crystal structures, it prevents the crowding of nitrogen atoms in KMC simulations. Namely, nitrogen atoms will jump to nitrogen-neighbouring octahedral spaces infrequently, due to the contribution of the E_{N-N}^*



(a) Nitrogen migration



(b) Vacancy migration

Figure 5.2: Results from Nudged Elastic Band (NEB) calculations in BCC (left) and FCC (right) Fe supercells. Each filled square is an NEB data point. **Top:** The energy of an interstitial nitrogen atom in ferromagnetic BCC iron (left) and non-magnetic FCC iron (right) relative to a nitrogen atom in the gas state, as it transitions between octahedral positions (blue shaded circles) in the proximity of a vacancy (filled yellow square in lattice diagrams). The process used to obtain the reference energy of nitrogen gas is detailed in Karimi and Auinger [5]. **Bottom:** The energy of an iron atom in BCC (left) and FCC (right) Fe, as it transitions to a vacant nearest neighbour lattice position. Figure is reproduced from Karimi and Auinger [9] (2021).

term in equation 5.3. The current repulsion model is an approximation which does not account for the effect of a neighbouring nitrogen atom on the transition sites for nitrogen jumps. NEB calculations are needed to refine this by calculating the energy barriers where there is a N-N interaction, such as $E_{N(1\rightarrow2)}^N$ and $E_{N(2\rightarrow1)}^N$.

Temperature/Volume Dependent Energy Barriers

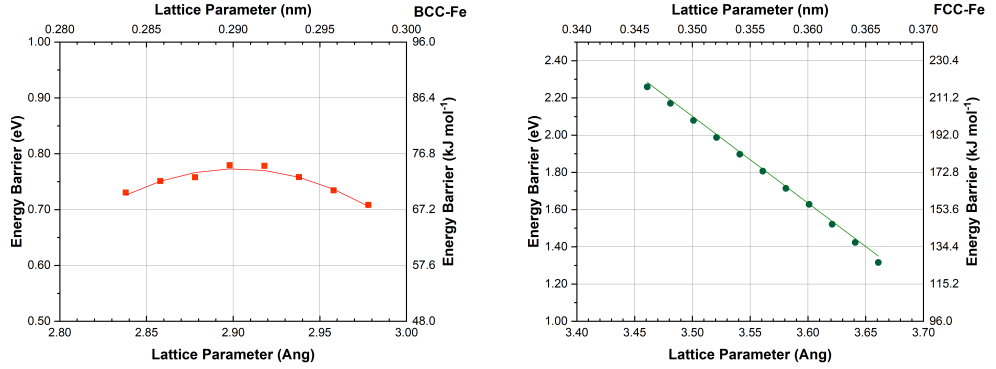


Figure 5.3: The calculated energy barrier for nitrogen diffusion in α iron (red curve, left) and γ iron (green line, right) when the lattice parameter is varied from its equilibrium value at absolute zero temperature. Filled squares and circles are data points calculated from first principles for ferromagnetic BCC iron and non-magnetic FCC iron respectively.

Figure 5.3 shows the relationship between the lattice parameter and energy barrier for nitrogen jumps. The data points shown in figure 5.3 can be fitted to quadratic (for BCC) and linear (for FCC) functions with small residual errors. The dependence of the energy barriers on the thermal expansion of the iron lattice can then be expressed (in kJ mol^{-1}) using the following equations for BCC and FCC respectively:

$$E_{v(i\rightarrow j)}^N(V, T) = E_{v(i\rightarrow j)}^N(T) - 0.8613 + 0.006374T - 0.000002056T^2, \quad (5.8)$$

$$E_{v(i\rightarrow j)}^N(V, T) = E_{v(i\rightarrow j)}^N(T) - 36.62 - 0.03854T. \quad (5.9)$$

The first terms in the equations are the energy barriers calculated at the equilibrium lattice parameters determined by DFT, which are temperature dependent at a fixed volume because of vibrational contributions. The vibrational contributions are calculated from the values in table 5.3 using equation 5.1. The other terms that follow in equations 5.8 and 5.9 represent the volume dependence of the energy

barriers as a function of temperature. This is done using well-established linear relationships between the lattice parameters and temperature [72], in combination with the relationships between the lattice parameters and energy barriers calculated in this work (see figure 5.3). Considering the case where $T = 0$, the volume correction is much larger for FCC Fe. This reflects the larger discrepancy between experimental and DFT-calculated ground state lattice parameters in FCC Fe compared to BCC Fe. The constant terms in equations 5.8 and 5.9 scale the DFT-calculated barrier $E_{v(i \rightarrow j)}^N(0)$ to correspond to experimentally-determined lattice parameters (extrapolated to absolute zero temperature), which are -0.7% (BCC Fe) and +2.8% (FCC Fe) smaller/larger than the lattice parameters used to calculate $E_{v(i \rightarrow j)}^N(0)$. For FCC Fe, volume considerations at absolute zero play a significant role in enforcing agreement between DFT and experimentally calculated nitrogen diffusion data. This is seen through the constant term in equation 5.9. If $T = 0$ in equation 5.9, then $\Delta E^N = 181.6 \text{ kJ mol}^{-1}$. This shows more promising agreement with the experimental value of $167.9 \text{ kJ mol}^{-1}$ than the ground state energy barrier of $218.2 \text{ kJ mol}^{-1}$.

Table 5.3: The zero point energy E_{zpe} , jump attempt frequency ν_N and vibrational energies ϵ_i for a nitrogen interstitial atom in ferromagnetic BCC iron and non-magnetic FCC iron, calculated from first principles. The nitrogen atom is approximated to behave as an independent three-dimensional harmonic oscillator which sits in an octahedral (OCT) or tetrahedral (TS) position in the iron lattice.

		Energies (eV)				
			E_{zpe}	ϵ_1	ϵ_2	ϵ_3
	$\log_{10}(\nu_N \text{ Hz})$					
BCC	12.828	OCT	0.095037	0.041587	0.044928	0.103559
		TS	0.10105	0.035421	0.082629	0.08405
FCC	13.052	OCT	0.113581	0.07468	0.075766	0.076715
		TS	0.108573	0.024165	0.096123	0.096858

5.5.2 Diffusion Model Results

KMC Simulations

Figure 5.4 shows the calculated diffusion coefficient of nitrogen at each of the 200 time increments for selected KMC trajectories at the start, middle and end of the reciprocal temperature range. In both α Fe and γ Fe, the diffusion coefficient formed by a trajectory generally decreases if the vacancy concentration is increased. The histograms for the trajectories with vacancies also tend to be flatter i.e. less concentrated at the median value. This is because vacancies create large differences in the

jump rates by changing the energy barrier in the exponential term of equation 5.3 in accordance with table 5.2. The frequencies of each jump type chosen by the KMC algorithm at each time increment will vary substantially, causing fluctuations in the recorded MSD (see equation 5.6) values. The effect of the fluctuations with respect to the diffusion coefficient diminish at later time increments as they become smaller with respect to the accumulated MSD. In contrast, the MSD steadily increases at each time increment in the vacancy-free simulations. Hence, the diffusion coefficient converges to its equilibrium value at a much earlier time increment in the vacancy free case.

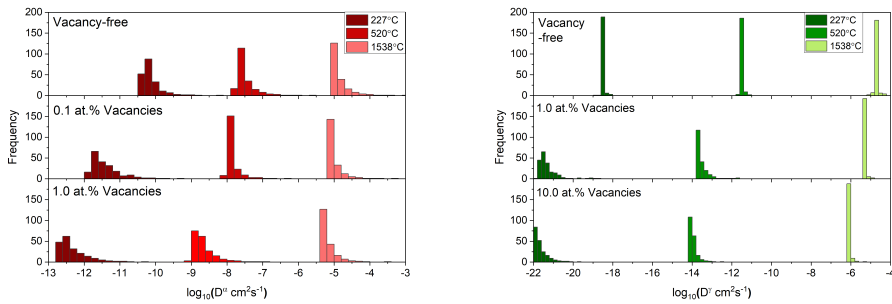


Figure 5.4: Traces of the diffusion coefficient of interstitial nitrogen atoms from Kinetic Monte Carlo trajectories in ferromagnetic BCC iron (red) and non-magnetic FCC iron (green) supercells. The BCC supercell contained a nitrogen concentration of 0.1 at.%, and the FCC supercell contained a nitrogen concentration of 1 at.%. The supercell for each trajectory had a fixed concentration of vacant lattice positions as labelled. Figure is reproduced from Karimi and Auinger [9] (2021).

The trajectory data for each temperature at a chosen vacancy concentration was used to fit the parameters in equation 5.5, and the residual errors for the fits are recorded in table 5.4. The corresponding data points for each fit are plotted in section 5.5.6. The vacancy-free fits have small residual errors regardless of whether the fitting expression is a linear, quadratic or cubic function of reciprocal temperature. Vacancies can cause superlinear growth in the diffusion coefficient as the temperature increases. This is reflected by the larger residual errors in the linear fits for vacancy-rich trajectories in table 5.4. Increasing the degree of the fitted polynomial, decreases the residual errors. In particular, using a quadratic fit reduces the average residual so it is less than 0.01 in all cases. Over a short temperature range ($< 200^\circ\text{C}$) all fits are approximately linear (see figure 5.12 to verify this). Thus, a linear extrapolation is used to extend the lower bound of the temperature range for the fits from 227°C (the smallest KMC temperature) to 100°C so that it can be compared to low-temperature experimental data. Extrapolation is preferred

over explicit calculation here, as a lot of computational resources are saved with a negligible effect on the accuracy.

Table 5.4: The sum of squared residuals (SSR) and average squared residual (ASR) in polynomial fits for the diffusion coefficient of nitrogen in α/γ iron at fixed nitrogen concentration c_N and vacancy concentrations c_v .

		Polynomial Fit Degree					
		1		2		3	
	c_v at. %	SSR	ASR	SSR	ASR	SSR	ASR
α Fe, $c_N = 0.1$ at. %	0	0.02954	4.34E-04	0.02653	3.96E-04	0.02408	3.65E-04
	0.1	2.78625	0.04097	0.26359	0.00393	0.04024	6.10E-04
	1	0.67582	0.00994	0.13175	0.00197	0.0835	0.00127
γ Fe, $c_N = 1$ at. %	0	0.05002	7.36E-04	0.04933	7.36E-04	0.04835	7.33E-04
	1	1.33366	0.01961	0.21461	0.0032	0.13057	0.00198
	10	3.35103	0.04928	0.08166	0.00122	0.0778	0.00118

Vacancy-Free Diffusion

Figure 5.5 shows a comparison between the available experimental data and the calculated vacancy-free diffusion coefficients for nitrogen. The calculated diffusion coefficients are $\log_{10}(D^\alpha(T)) = \frac{-3652}{T} - 3.098$ and $\log_{10}(D^\gamma(T)) = \frac{-9515}{T} + 0.4588$. The most significant discrepancies between the experimental and calculated sources are seen for the BCC Fe phases (α and δ) at higher temperatures. This is because a single linear Arrhenius-type fit can not accurately portray nitrogen diffusion in BCC iron up to its melting point [10]. Diffusion-enhancing magnetic effects [36] are thought to be the cause of divergence from a single linear fit in the experimental data, which are not incorporated in the computational model. As documented by [10], the experimental data can be separated into two linear fits at the point where $\frac{1}{T} = 0.0029$. The low-temperature fit ($\frac{1}{T} > 0.0029$) of $\log_{10}(D^\alpha(T)) = \frac{-3727}{T} - 3.376$ is outside of the temperature range calculated in this work. However, because the data is linear, the calculated fit should extrapolate accurately to lower temperatures. Indeed, comparing the energy barriers (-3727 and -3652) and prefactors (-3.376 and -3.098) shows agreement between the low-temperature experimental fit and the calculated fit for α Fe. In contrast, the high-temperature fit ($\frac{1}{T} < 0.0029$) of $\log_{10}(D^\alpha(T)) = \frac{-4176}{T} - 2.001$ shows divergence from the low-temperature fits.

In nitrogen-saturated iron, an experimentally-calculated diffusion coefficient will deviate from the values in figure 5.5. The KMC supercells are assumed to retain a cubic crystal structure under all diffusion conditions considered in this work. How-

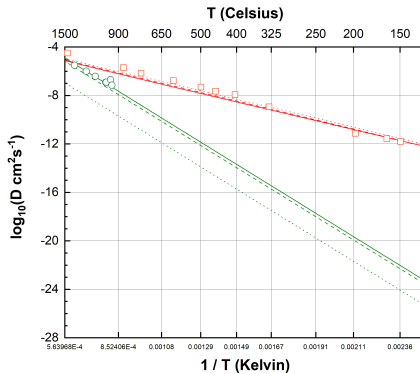


Figure 5.5: Nitrogen diffusion data calculated from first principles in ferromagnetic BCC iron (red lines) and non-magnetic FCC iron (green lines). Solid lines indicate that volume and vibrational contributions are incorporated into the calculation. Dashed lines indicate only volume contributions are included, while the dotted lines indicate both contributions are omitted. Experimental diffusion data for α iron [10] (red squares) and γ iron [11] (green circles) are included for comparison. Figure is reproduced from Karimi and Auinger [9] (2021).

ever, in BCC Fe nitrogen interstitials induce a local tetrahedral distortion. If the nitrogen concentration is small enough that the nitrogen atoms rarely interact, the distortion does not impact diffusion. However, due to the distortion, neighbouring nitrogen interstitials will have asymmetric diffusion pathways. When the nitrogen concentration is high, the energies of the octahedral stable sites and tetrahedral transition sites will not be equivalent throughout the lattice. This effect makes the energy barrier for nitrogen diffusion dependant on the nitrogen concentration. The experimentally calculated diffusion coefficient of nitrogen does not deviate significantly in dilute nitrogen concentrations up to at least $c_N = 0.7$ at.% [96]. Looking to the analogous case of carbon interstitials, which are more studied than nitrogen interstitials in this regard, the impact on diffusion is significant at a solute concentration of 5 at.% where the energy barrier differs by around 10 kJ mol^{-1} compared to the dilute case [97]. Similar effects would likely be observed for nitrogen interstitials, as the divergence from a cubic crystal in super-saturated Fe-N is significant at $c_N = 4.4$ at.% [98]. Furthermore, Fe_{16}N_2 forms in Fe-N martensites at low temperatures ($< 400 \text{ K}$) [44]. This affects the diffusivity of nitrogen in a substantial concentration range ($0.05 \text{ at.}\% < c_N < 11 \text{ at.}\%$). More information is needed to assess the extent of these effects if vacancies are introduced, as vacancies significantly change the conditions where each type of nitride is stable [5].

The nitrogen concentration dependency found experimentally in austenite

(FCC Fe) is particularly strong when the nitrogen concentration exceeds 1 at.% [88], and the underlying reasoning for this may not be incorporated in the current model. For instance, the findings of this work suggest that volume-considerations are important (see figure 5.5) for nitrogen diffusion in austenite. The model considers the thermal expansion of the Fe lattice, but it does not consider the substantial lattice expansion which is induced by increasing the nitrogen concentration [6].

Impact of Vacancies

The presence of vacancies in excess of their expected concentration at thermal equilibrium can result in significantly slower nitrogen diffusion in both α and γ Fe. At fixed nitrogen concentration, the diffusion coefficient decreases with increased vacancy concentration. The impact of vacancies on diffusion is less pronounced at higher temperatures because nitrogen atoms are more likely to escape from them. This can be seen by considering the definition of a jump rate in equation 5.3. As the temperature increases, all jump rates approach a common value of v_x , meaning that the random walk followed by nitrogen atoms approaches a symmetrical random walk. Hence, the dynamics simulation closely resembles interaction-free (between nitrogen and vacancies) diffusion at high temperatures.

There are 42 and 38 octahedral trapping sites around a vacancy in BCC and FCC crystals respectively, with 48 and 78 transition events between trapping sites to the interaction-free sites. Therefore, α Fe has more sites to hold nitrogen atoms, and there are fewer routes for those trapped atoms to escape. However, there are three octahedral spaces for each lattice space in a BCC crystal, meaning that it has a larger proportion of interaction-free sites relative to a FCC crystal with the same vacancy concentration. Migration to vacancies in α Fe was generally calculated to be more energetically favoured than in γ Fe. For instance, $E_{v(1\rightarrow2)}^N - E_{v(2\rightarrow1)}^N = 70.3 \text{ kJ mol}^{-1}$ and 60.6 kJ mol^{-1} for α and γ respectively. The repulsion energy between two nitrogen atoms in α was found to be much larger (see section 5.5.1). A higher repulsion energy reduces the ability of vacancies to trap multiple nitrogen atoms, meaning that the trapping effect diminishes quickly if the nitrogen concentration is higher than the vacancy concentration.

Figure 5.6 quantifies the decrease in the nitrogen diffusion coefficient when the vacancy concentration increases. The nitrogen concentrations are fixed at $c_N = 0.1 \text{ at.}\%$ for α Fe and $c_N = 1 \text{ at.}\%$ for γ Fe, which are chosen to represent typical nitrogen solubility values for each phase. The dashed black curves highlight where $c_v = c_N$, which signifies an important change in the dynamics of the KMC simulations because each nitrogen has at least one vacancy to bind to. At low tem-

peratures, the binding is so strong that the nitrogen atoms are barely mobile enough to explore the supercell, so increasing the concentration of vacancies has a limited impact on the already 'frozen' nitrogen. As the temperatures increase, increasing the vacancy concentration has a more pronounced effect on diffusion. This effect can be seen from the $c_v = c_N$ curves in figure 5.6, because they increase at a superlinear rate as the temperature increases. In α Fe the curve is close to vacancy-free diffusion at high temperatures, but it diverges at low temperatures where the trapping effect is stronger. In γ Fe, the curve is close to the lower bound of diffusion speed in the vacancy range tested i.e. the fitted curves with $c_v = 1$ at.% and $c_v = 10$ at.% are similar. Thus, there is a large difference in the behaviour of α Fe with $c_N = 0.1$ at.% and γ Fe with $c_N = 1$ at.% when $c_v > c_N$. This can also be seen in figure 5.7; in the γ case there is a sharp change at $c_v = c_N = 1$ at.% where increasing the vacancy concentration has minimal impact on diffusion; in α the diffusion speed consistently decreases when the vacancy concentration increases. A significant consideration here is that in α Fe the concentrations are an order of magnitude smaller than in γ Fe, meaning that interactions are overall less likely. When $c_v = c_N = 0.1$ at.% there is a vacancy available to pair with each nitrogen, but the nitrogen-vacancy encounter rate is lower than for $c_v = c_N = 1$ at.%. Indeed, the diffusion coefficient for $c_v = c_N = 0.1$ at.% in γ Fe was found to closely correspond to vacancy-free diffusion, which contrasts the $c_v = c_N = 1$ at.% case which is depicted in figure 5.6.

The vacancy concentrations which are investigated (0.01 at.% $< c_v < 10$ at.%) represent extreme levels of deformation which do not necessarily arise under common manufacturing conditions. However, it can be seen from figure 5.7 that the impact of vacancies is greatly diminished if the vacancy concentration is an order of magnitude smaller than the nitrogen concentration. This suggests that extreme levels of deformation are required in order to observe significant disruption of nitrogen diffusion due to vacancy-related effects. It has previously been shown in the case of nitrogen solubility that vacancy-rich models from first principles can depict the nature of nitrogen in iron more accurately than vacancy-free models [5]. There is evidence that the same applies for the diffusion model in this work, although a conclusive judgement is not possible with the experimental data that is currently available. Concerning low-temperature diffusion data for α Fe, the Arrhenius fit for the experimental data is close to the calculated fit, but it is strictly smaller over the temperature range with a steeper gradient and a smaller prefactor (see section 5.5.2). Moreover, the low-temperature experimental data points ($< 200^\circ\text{C}$) in figure 5.6 are all below the calculated vacancy-free diffusion fit. The diffusion data measured by low-temperature experiments is better represented by the calculated data with va-

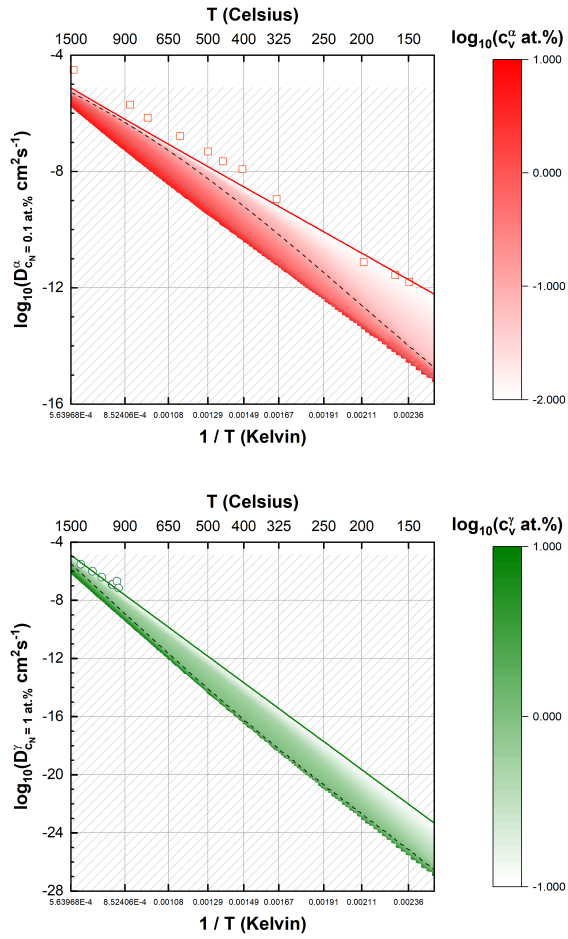


Figure 5.6: The interstitial diffusion coefficient D of nitrogen in α iron (red, top) and γ iron (green, bottom) calculated with nitrogen concentrations $c_N = 0.1$ at.% and $c_N = 1.0$ at.% respectively. Experimental data points for comparison are from [10] (red squares) and [11] (green circles). The diffusion coefficients calculated in absence of vacancies are given by red and green solid lines. The contour surfaces indicate the shift in diffusion coefficient at varied vacancy concentrations. The dashed black curves on the contour surfaces indicate where the nitrogen and vacancy concentrations are equal. Figure is reproduced from Karimi and Auinger [9] (2021).

cancy concentrations of around $0.01 \text{ at.\%} < c_v < 0.1 \text{ at.\%}$, which is many orders of a magnitude higher than the vacancy concentration expected at equilibrium. It is not possible to conclude if the situation is similar for high-temperature α Fe, as there are deviations which are thought to be unrelated to vacancies (discussed in section 5.5.2), and the effect of vacancies are smaller at higher temperatures. All of the experimental data points for γ Fe are above 912°C , because high-purity γ

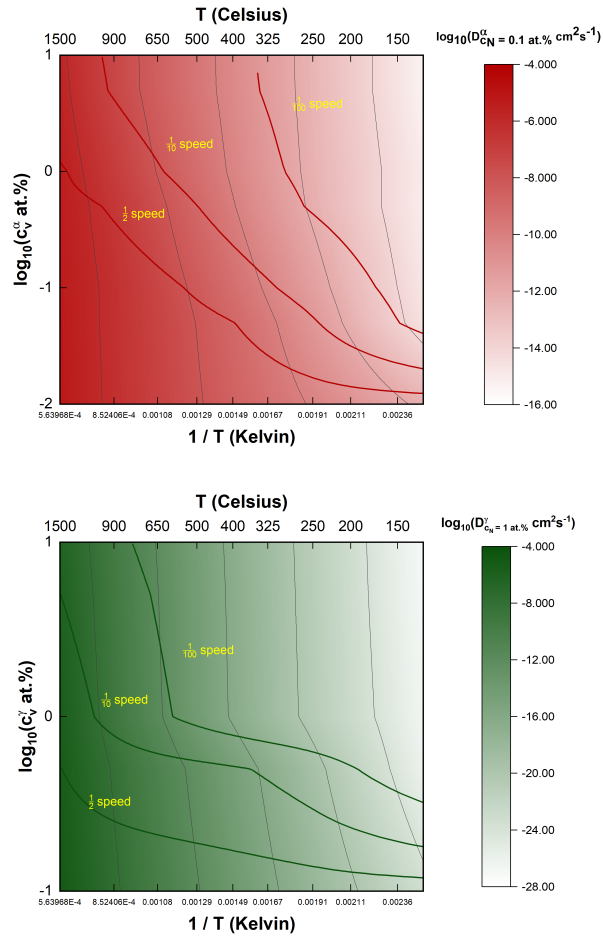


Figure 5.7: The contour surface which portrays the shift in the diffusion coefficient of nitrogen in α iron (red, top) and γ iron (green, bottom) at varied vacancy concentrations and temperatures. The nitrogen concentration is fixed at 0.1 at.% and 1 at.% for α and γ respectively. red and green lines on the surfaces trace the points where the diffusion coefficient has decreased (compared to vacancy-free diffusion) 2, 10 and 100-fold due to vacancies. Figure is reproduced from Karimi and Auinger [9] (2021).

Fe is not stable at lower temperatures. Therefore, as seen in figure 5.6, a vacancy concentration larger than 0.1 at.% would be required to disrupt nitrogen diffusion to a significant extent. This is unlikely in experiments which intentionally use pure and well-formed Fe, so it is not surprising that the experimental data is in close agreement with the vacancy-free calculation.

The current model is limited to singular point defect interactions. However, when nitrogen and vacancies are abundant within iron, larger nitrogen-vacancy com-

plexes can form [5, 46, 48]. This may result in deviations between the calculated and experimental diffusion data, particularly when the concentrations of nitrogen or vacancies exceed that of the DFT supercells which were used to calculate the energy barriers (see table 5.1). From the size of the DFT supercells, the concentrations where such deviations could begin to occur are estimated to be around 1.9 at.% and 2.1 at.% for α and γ Fe respectively. Concerning mono-vacancy multi-nitrogen complexes, the deviations should not be significant. In both α and γ Fe the most abundant complexes of this type are those containing one (vN) or two (vN₂) nitrogen atoms. The respective difference in nitrogen binding energies between vN and vN₂ for either Fe phase does not exceed 10 kJ mol⁻¹ [5]. Therefore, the jump rates associated with the vN complex are a good approximation for the rates associated with the vN₂ complex, while complexes with three or more nitrogen atoms are rare enough to disregard for most applications. Insufficient information is available to deduce the significance of multi-vacancy multi-nitrogen complexes, meaning that the calculated results should be treated with scrutiny when 1 at.% < c_v < 10 at.% as the omitted vacancy-vacancy interactions would be frequent. Furthermore, the nitrogen repulsion energy used in the calculations is not affected by the presence of vacancies. Hence, the current repulsion model does not capture the nuances of nitrogen-vacancy interactions. However, it has the desirable effect of discouraging the formation of overly nitrogen-dense complexes which are non-physical.

Vacancy-Dependent Diffusion Coefficient

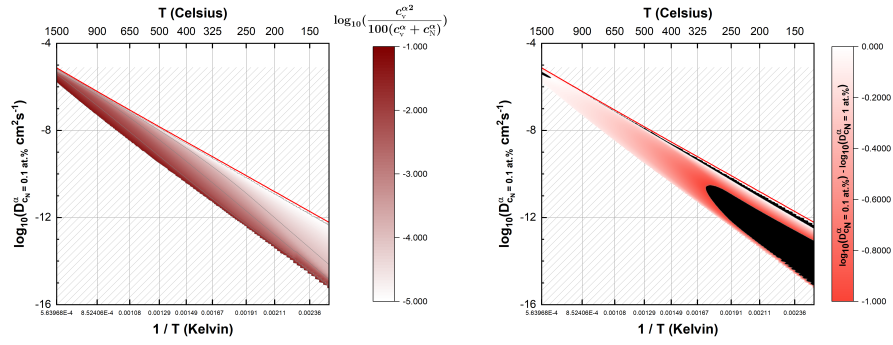
In order to cast the calculated diffusion data in an applied setting, it is used to fit diffusion coefficients as functions of nitrogen concentration, vacancy concentration and temperature. In particular, each a_k^s from equation 5.5 is expressed as a function of c_v and c_N . Two intuitive considerations are used to choose the form of the a_k^s . Firstly, the vacancy mixing ratio $\frac{c_v}{c_v+c_N}$ is closely tied to the trapping ability of vacancies. If there are few vacancies relative to nitrogen atoms, then the vacancy contribution to the diffusivity of nitrogen will be small, as the displacement is averaged over all nitrogen atoms (see equation 5.6). However, the mixing ratio is not sufficient to fully capture the relationship. If the absolute vacancy concentration is small, nitrogen-vacancy interactions will be unlikely regardless of what the mixing ratio is. To account for both the ratio and the absolute vacancy concentration, each parameter of equation 5.5 is expressed as $a_k^s = \sum_j b_j \log_{10} \left(\frac{c_v^2}{100(c_v+c_N)} \right)^j$ where the b_j are obtained from least squares fitting. The reader is referred to table 5.5 for the fitted parameter values and the spreadsheet in the supplementary data for example usages.

In this work, the parameters are only calculated at nitrogen concentrations of 0.1 at.% and 1.0 at.%, meaning that they will not generalise over a range of nitrogen concentrations as well as they do in a range of vacancy concentrations. The fit corresponding to $c_N = 1$ at.% in α Fe is used to validate the $c_N = 0.1$ at.% fit, and similarly the $c_N = 1$ at.% fit is validated against the $c_N = 0.1$ at.% fit in γ Fe. This approximates the upper bounds of error from generalising the diffusion coefficient to varied nitrogen concentrations over the full range of conditions as shown in figure 5.8.

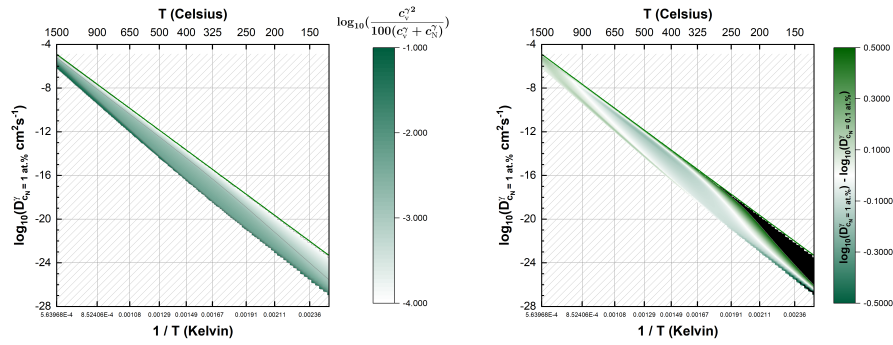
Table 5.5: Fitted parameters for diffusion coefficients of nitrogen in α iron and γ iron which are dependent on nitrogen concentration c_N , vacancy concentration c_v and temperature T Kelvin. The fits are valid in a range of $\log_{10}(\frac{c_v^2}{100(c_v+c_N)})$ values which are specified in the table. AR denotes the average residual error of the fit.

$\alpha, c_N = 0.1$ at.%		$\log_{10}(\frac{c_v^2}{100(c_v+c_N)})_{\min}$	$\log_{10}(\frac{c_v^2}{100(c_v+c_N)})_{\max}$	AR (%)		
		-5.04E+00	-1.01E+00	4.48E-01		
		b_0	b_1	b_2	b_3	b_4
	a_0	-4.80E+00	-2.35E+00	-3.41E-01	1.84E-01	3.44E-02
	a_1	-9.19E+02	7.07E+03	3.08E+03	3.15E+02	-8.03E+00
a_2	-1.37E+06	-2.54E+06	-1.21E+06	-1.56E+05	-9.87E+02	
$\alpha, c_N = 1$ at.%		$\log_{10}(\frac{c_v^2}{100(c_v+c_N)})_{\min}$	$\log_{10}(\frac{c_v^2}{100(c_v+c_N)})_{\max}$	AR (%)		
		-6.00E+00	-1.04E+00	5.88E-01		
		b_0	b_1	b_2	b_3	b_4
	a_0	-4.84E+00	-3.21E+00	-1.62E+00	-3.17E-01	-2.14E-02
	a_1	-3.22E+03	4.03E+03	2.57E+03	5.55E+02	3.95E+01
a_2	3.80E+05	3.57E+05	1.63E+05	3.29E+04	2.35E+03	
$\gamma, c_N = 0.1$ at.%		$\log_{10}(\frac{c_v^2}{100(c_v+c_N)})_{\min}$	$\log_{10}(\frac{c_v^2}{100(c_v+c_N)})_{\max}$	AR (%)		
		-5.04E+00	-1.00E+00	1.06E+00		
		b_0	b_1	b_2	b_3	
	a_0	-3.87E+00	-6.31E+00	-2.30E+00	-2.42E-01	
	a_1	-5.62E+03	9.89E+03	4.10E+03	4.56E+02	
a_2	-4.54E+05	-1.36E+06	-5.88E+05	-6.69E+04		
$\gamma, c_N = 1$ at.%		$\log_{10}(\frac{c_v^2}{100(c_v+c_N)})_{\min}$	$\log_{10}(\frac{c_v^2}{100(c_v+c_N)})_{\max}$	AR (%)		
		-4.04E+00	-1.04E+00	9.69E-01		
		b_0	b_1	b_2	b_3	
	a_0	-1.06E+01	-1.69E+01	-7.22E+00	-9.18E-01	
	a_1	8.67E+03	3.23E+04	1.44E+04	1.86E+03	
a_2	-6.13E+06	-1.03E+07	-4.65E+06	-6.12E+05		

It is reported in literature that carbon interstitials, like nitrogen interstitials,



(a) α -Fe



(b) γ -Fe

Figure 5.8: The diffusion coefficient of nitrogen in vacancy-containing α iron (red, top) and γ iron (green, bottom). The figures on the left hand side indicate the shift in the diffusion coefficient at a range of values of the expression $\log_{10} \left(\frac{c_v^2}{100(c_v^2 + c_N^2)} \right)$, where c_N is the nitrogen concentration and c_v is the vacancy concentration. The left hand side figures are calculated with interstitial nitrogen concentrations of $c_N = 0.1$ at.% and $c_N = 1$ at.% for α iron and γ iron respectively. The figures on the right hand side shows the difference between polynomial fits of the diffusion coefficient corresponding to two different nitrogen concentrations. The areas where the difference between the fits is outside of the colour bar range of the contours is coloured in black. Figure is reproduced from Karimi and Auinger [9] (2021).

are strongly attracted to vacancies [46]. Therefore, carbon atoms could compete with nitrogen for energetically favourable locations around vacancies, acting as a deterrent to nitrogen trapping near vacancies. This would suggest that the quantified results are lower bounds of an experimentally-calculated diffusion coefficient, because they carry the underlying assumption that the available trapping sites are solely accessible to nitrogen. This would be a particularly important consideration when the carbon concentration exceeds the nitrogen concentration. Moreover, the calculated diffusion coefficient in this work is dependent on nitrogen concentration,

but it is invariant under changing nitrogen concentration unless the vacancy concentration is greater than zero. This is a simplification. As discussed in section 5.5.2, the diffusion coefficient is dependent on the nitrogen concentration in vacancy-free Fe.

5.5.3 Using the Supplementary Spreadsheet

The spreadsheet referred to in this section is contained in the supplementary data of [9].

Vacancy-Free Diffusion

In the vacancy-free case there is only one input to the spreadsheet, which is the temperature in °C. This should be entered into cell A6. Cell E7 will turn red to warn the user if the input temperature is outside of the validity range of the fit. The corresponding diffusion coefficient for nitrogen is calculated in U10 and U19 for α Fe and γ Fe respectively.

Vacancy-Dependent Diffusion

In the vacancy-dependent case there are three inputs to the spreadsheet, the nitrogen concentration, vacancy concentration and temperature. The temperature input is the same as in section 5.5.3. The nitrogen concentration and vacancy concentration are entered into cells A31 and B31, respectively. There are four diffusion coefficients calculated in total, which are found in cells U36 (α Fe, $c_N = 0.1$ at.%), U50 (α Fe, $c_N = 1$ at.%), U71 (γ Fe, $c_N = 0.1$ at.%) and U85 (γ Fe, $c_N = 1$ at.%). Each of the diffusion coefficients is calculated using the fitted parameters recorded in table 5.5. Potential issues with the calculated diffusion coefficient at the chosen conditions are flagged by the diagnostic cells: U62, V36, and V50 for α Fe; U97, V71 and V85 for γ Fe. The examples that follow show how to interpret the calculated result and use the diagnostic cells for α Fe, and similar statements apply to γ Fe.

Example 1

- Input $T = 500^\circ\text{C}$, $c_v = 0.5$ at.% and $c_N = 0.1$ at.%.
- The value of U50 should be disregarded, as an experimentally-calculated diffusion coefficient will closely match U36. This is because the parameters which are used to calculate U36 are fitted from simulation data where $c_N = 0.1$ at.%.

Example 2:

- Input $T = 500^\circ\text{C}$ and $c_v = c_N = 0.5 \text{ at.}\%$.
- An experimentally-calculated diffusion coefficient should be in the interval between U36 and U50. However, because $c_N = 0.5 \text{ at.}\%$ is close to $c_N = 1 \text{ at.}\%$ on a logarithmic scale, the diffusion coefficient is likely much closer to U50 than U36.
- The maximum error caused by using interpolation to calculate the diffusion coefficient for $0.1 \text{ at.}\% < c_N < 1 \text{ at.}\%$ is displayed in U62, which is the length of the interval between U36 and U50. However, this is the absolute upper bound. If the two calculated diffusion coefficients are weighted appropriately, the error is likely to be smaller. Moreover, as shown in figure 5.8a the error varies greatly with temperature. At some temperatures the nitrogen concentration can be changed without significantly increasing the margin for error.

Example 3:

- Input $T = 500^\circ\text{C}$, $c_v = 0.001 \text{ at.}\%$ and $c_N = 0.1 \text{ at.}\%$.
- At the chosen nitrogen concentration one might expect that the diffusion coefficient in U36 closely resembles an experimentally-calculated diffusion coefficient. However, in this case V36 is highlighted in red. This is to indicate that the U36 value exceeds the vacancy-free diffusion coefficient for $\alpha \text{ Fe}$, so it is no longer in the coloured region of figure 5.8a (left hand side) at the chosen temperature. This can be verified by cross-referencing the figure with the value in cell E31.
- The vacancy concentration is much smaller than the nitrogen concentration. This means that the value of $\log_{10} \left(\frac{c_v^2}{100(c_v + c_N)} \right)$ is below the minimum threshold for the fit to be valid. However, the vacancy-free diffusion coefficient (U10) closely resembles an experimentally-calculated diffusion coefficient, because the vacancy contribution to diffusion will be accordingly small.

5.5.4 FCC $1 \rightarrow 1$ jump

Figure 5.9 shows the minimum energy path for a $1 \rightarrow 1$ jump of nitrogen in a FCC lattice, and a graphical representation of the jump in a FCC supercell is given in figure 5.1. The $E_{v(1 \rightarrow 1)}^N$ energy barrier was found to be $108.8 \text{ kJ mol}^{-1}$. $E_{v(1 \rightarrow 1)}^N$ is far smaller than all the other FCC energy barriers (see table 5.2), meaning that the $1 \rightarrow 1$ jump rate $r_{v(1 \rightarrow 1)}^N$ is many orders of magnitude larger than the other jump rates. Moreover, the large $E_{v(1 \rightarrow 2)}^N = 252.7 \text{ kJ mol}^{-1}$ energy barrier ensures with

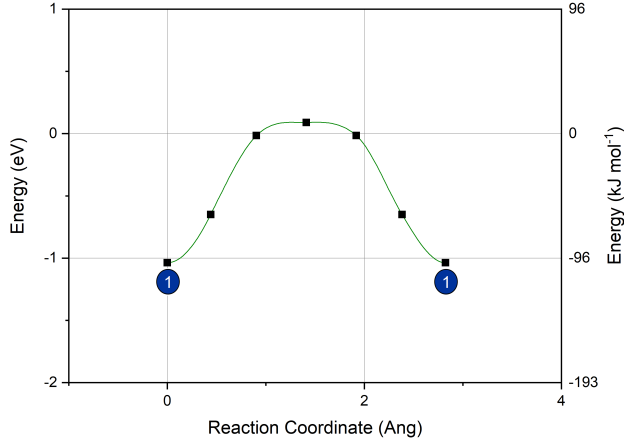


Figure 5.9: The energy of an interstitial nitrogen atom in non-magnetic FCC iron relative to a nitrogen atom in the gas state, as it transitions between symmetrical octahedral positions which are first nearest neighbours to a vacancy. The process used to obtain the reference energy of nitrogen gas is detailed in Karimi and Auinger [5]. Figure is reproduced from Karimi and Auinger [9] (2021).

high statistical certainty that many $1 \rightarrow 1$ jumps are repeated in succession before a nitrogen atom leaves a vacancy. At equilibrium, the random walk followed by each nitrogen atom which jumps between first nearest neighbour (FNN) positions to a vacancy in an arbitrary time interval is constrained to a finite domain. The finite domain ensures that, for any time interval where a nitrogen atom performs successive $1 \rightarrow 1$ jumps, every starting and ending position is equally likely. Hence, the mean squared displacement (MSD) (see equation 5.6) is constant with respect to a sequence of repeated $1 \rightarrow 1$ jumps over time. If the system is restricted to only $1 \rightarrow 1$ jumps, the theoretical value of the MSD is the expected value over all the possible squared displacements. There are a total of 36 squared displacements which the nitrogen atom can achieve in each coordinate dimension while restricted to FNN positions around a vacancy. 18 of the possible displacements are zero, 16 are $(\frac{a}{2})^2$ and two are a^2 . Hence, the MSD contribution at equilibrium is

$$\mu_{1 \rightarrow 1} = 3 \times \frac{16(\frac{a}{2})^2 + 2a^2}{36} = \frac{a^2}{2}. \quad (5.10)$$

The lattice parameter a for γ Fe is given by the expression $a = 3.544 + 0.0000856T$ where T is the temperature [72]. For example, using equation 5.10 for $T = 500$ K, the equilibrium contribution of repeated $1 \rightarrow 1$ jumps to the MSD is 6.43 \AA^2 . Figure 5.10 shows the effect of the $1 \rightarrow 1$ jump on the MSD in KMC

simulations. At each temperature considered, the MSD fluctuates about the theoretical value implied by restricting the nitrogen atom to only FNN positions. The large $r_{v(1 \rightarrow 1)}^N$ rate means that the vast majority of KMC steps consist of repeated $1 \rightarrow 1$ jumps. Hence, a simulation with $1 \rightarrow 1$ jumps included requires orders of magnitude more KMC steps to reach equilibrium. The dashed lines in figure 5.10 show that the MSD approaches the expected linear relationship with time, in the same number of KMC steps, if $1 \rightarrow 1$ jumps are omitted from the simulation.

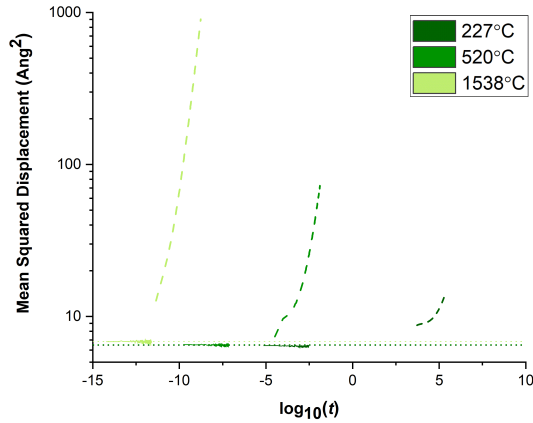


Figure 5.10: Traces of the mean squared displacement of nitrogen atoms over time t in non-magnetic FCC iron with a vacancy concentration of 10 at.% and interstitial nitrogen concentration of 1 at.%. Solid lines represent trajectories where first nearest neighbour jumps for nitrogen around a vacancy are included in Kinetic Monte Carlo (KMC) simulations, and dashed lines represent trajectories where such jumps are omitted. Each of the six traces shown comprise of 250000 KMC steps. The dotted lines show the theoretical contribution to the mean squared displacement from repeated first nearest neighbour jumps of nitrogen around a vacancy at equilibrium. Figure is reproduced from Karimi and Auinger [9] (2021).

It is not computationally viable to determine the impact of the $1 \rightarrow 1$ jump on the diffusion coefficient of nitrogen through direct calculation, because the $1 \rightarrow 1$ jump creates poor convergence behaviour in KMC. Rather, upper bounds are derived for its impact under the considered conditions in this work. Denote the MSD of a single nitrogen atom $\mu(t)$ at time t . At equilibrium, the MSD is linear with respect to time with a constant gradient. Thus, in equal-length time intervals, the MSD's are also equal. That is,

$$\mu(t) = \mu(t - k) + \mu(k) \quad (5.11)$$

for any $t \geq k \geq 0$. Let $0 \leq t_{\text{enter}}^0 \leq t_{\text{exit}}^0 < t_{\text{enter}}^1 \leq t_{\text{exit}}^1 < \dots < t_{\text{enter}}^m \leq t_{\text{exit}}^m \leq t$

represent the (possibly zero) distinct times that the nitrogen atom enters/exits a vacancy. The $[t_{\text{enter}}^i, t_{\text{exit}}^i]$ interval spans the time where the nitrogen atom is in FNN positions to a vacancy. The $1 \rightarrow 1$ jump repeatedly occurs in the interval, with the last one completing at time t_{exit}^i . Denote the total time the nitrogen spends in FNN positions as $t_v = \sum_{i=0}^{i=m} t_{\text{exit}}^i - t_{\text{enter}}^i$. Using equation 5.11, the MSD is

$$\mu(t) = |x(t) - x(0)|^2 = \underbrace{|x(t - t_v) - x(0)|^2}_{\text{all other jumps}} + \underbrace{\sum_{i=0}^{i=m} |x(t_{\text{exit}}^i) - x(t_{\text{enter}}^i)|^2}_{1 \rightarrow 1 \text{ jumps only}}. \quad (5.12)$$

Where $x(t)$ denotes the location of the nitrogen atom at time t . At equilibrium, $m \leq 1 + r_{v(1 \rightarrow 2)}^N t$ in equation 5.12, because a $1 \rightarrow 2$ jump must occur before each new unique vacancy entry time. Moreover, because nitrogen is restricted to a single vacancy in each interval, the value of $\frac{\sum_{i=0}^{i=m} |x(t_{\text{exit}}^i) - x(t_{\text{enter}}^i)|^2}{m}$ approaches $\frac{a^2}{2}$ (see equation 5.10) as $m \rightarrow \infty$. Hence,

$$\begin{aligned} \sum_{i=0}^{i=m} |x(t_{\text{exit}}^i) - x(t_{\text{enter}}^i)|^2 &= m \frac{\sum_{i=0}^{i=m} |x(t_{\text{exit}}^i) - x(t_{\text{enter}}^i)|^2}{m} \\ &\leq (1 + r_{v(1 \rightarrow 2)}^N t) \frac{\sum_{i=0}^{i=m} |x(t_{\text{exit}}^i) - x(t_{\text{enter}}^i)|^2}{m} \\ \implies \sum_{i=0}^{i=\infty} |x(t_{\text{exit}}^i) - x(t_{\text{enter}}^i)|^2 &\leq (1 + r_{v(1 \rightarrow 2)}^N t) \frac{a^2}{2} \end{aligned} \quad (5.13)$$

Combining equations 5.7, 5.12 and 5.13, and noting that $m \rightarrow \infty$ as $t \rightarrow \infty$

$$\begin{aligned} D(t) &= \lim_{t \rightarrow \infty} \frac{|x(t - t_v) - x(0)|^2}{6t} + \lim_{t \rightarrow \infty} \frac{\sum_{i=0}^{i=m} |x(t_{\text{exit}}^i) - x(t_{\text{enter}}^i)|^2}{6t} \\ &\leq \lim_{t \rightarrow \infty} \frac{|x(t - t_v) - x(0)|^2}{6t} + \lim_{t \rightarrow \infty} \frac{a^2(1 + r_{v(1 \rightarrow 2)}^N t)}{12t} \\ &= \lim_{t \rightarrow \infty} \frac{|x(t - t_v) - x(0)|^2}{6t} + \frac{a^2 r_{v(1 \rightarrow 2)}^N}{12}. \end{aligned} \quad (5.14)$$

In this work, the diffusion coefficient is approximated by the left hand side term of equation 5.14, by omitting the $1 \rightarrow 1$ jump from KMC simulations. Over all the conditions considered, the right hand side term is generally small compared to the left hand side term, meaning that the error caused by the approximation is small. Figure 5.11 shows the maximum error by using equation 5.14 to compute

the maximum difference in the diffusion coefficient. For any vacancy concentration smaller than 1 at.%, the error is negligible. The only conditions where the error margin of 0.05 for KMC simulations (see section 5.4.2) are surpassed is when the vacancy concentration is 10 at.% and the temperature is over 900°C. The upper bound set by equation 5.13 is generous, because $r_{v(1\rightarrow 2)}^N t$ may be significantly larger than the rate that nitrogen visits new vacancies. Hence, the potential magnitude of error is insufficient to justify the vastly higher computational cost to include the $1 \rightarrow 1$ jump in KMC simulations.

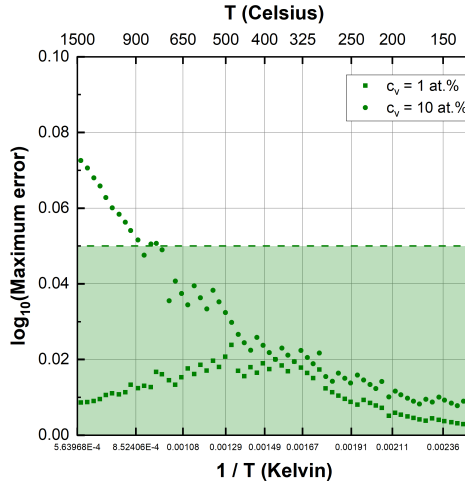


Figure 5.11: Maximum error in the calculated diffusion coefficient of nitrogen in non-magnetic FCC iron, if first nearest neighbour jumps for nitrogen around a vacancy are omitted from Kinetic Monte Carlo simulations. The vacancy concentration of iron is denoted by c_v . The area under the dashed line shows where the error is smaller than the chosen convergence criteria for KMC simulations. Figure is reproduced from Karimi and Auinger [9] (2021).

5.5.5 Piecewise Log-Linear Interpolation

Piecewise log-linear interpolation is applied in this work to approximate the diffusion coefficient between two parameters when the other parameters are fixed. For example, at fixed T and c_{N_m} , let l index a sorted set of all the c_{v_l} where $c_{N_l} = c_{N_m}$. Then for any c_v with $c_{v_l} < c_v < c_{v_{l+1}}$, $\log(D^s(T, c_v, c_{N_m})) = B + A \log(c_v)$, where A and B define the line which joins $(\log(c_{v_l}), \log(D^s(T, c_{N_m}, c_{v_l})))$ and $(\log(c_{v_{l+1}}), \log(D^s(T, c_{N_m}, c_{v_{l+1}})))$.

5.5.6 Simulated Diffusion Data Plots

Figure 5.12 contains the raw data points from selected KMC trajectories in this work.

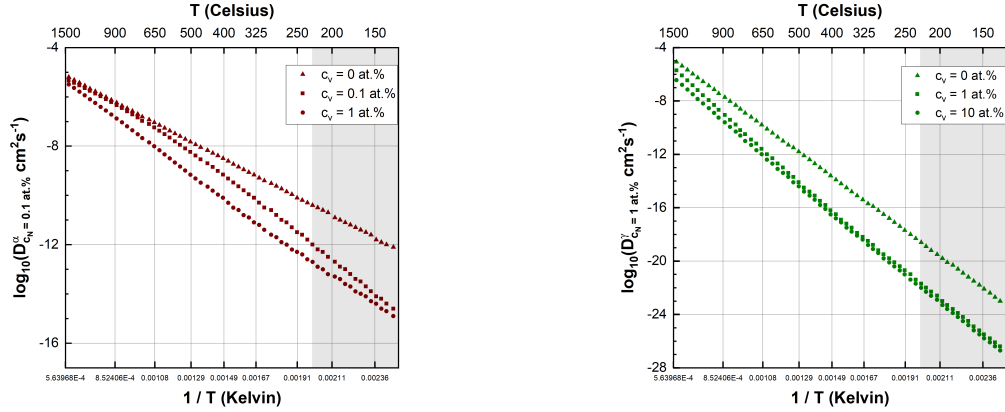


Figure 5.12: The diffusion coefficient of nitrogen in α iron (red, top) and γ iron (green, bottom) with interstitial nitrogen concentrations of 0.1 at.% and 1 at.% respectively. The vacancy concentration of the iron is denoted by c_v . The data points represent converged data from Kinetic Monte Carlo simulations as detailed in the text. The grey shading indicates that the data points are extrapolated using a linear fit to the two closest calculated points. Figure is reproduced from Karimi and Auinger [9] (2021).

5.6 Conclusion

A robust multi-scale model was used in this work to generate nitrogen diffusion data in iron from first principles. The data was used to fit polynomial expressions so that it can be incorporated in applied settings, such as layer growth models for nitriding or further experimental research. Nitrogen diffusion was systematically investigated in α and γ Fe to enhance the clarity of the current literature. In particular, it is shown that non-magnetic FCC Fe can be a suitable candidate to model γ Fe for this purpose, provided that thermal expansion considerations are included. Good agreement was found between the diffusion model used in this work and the available experimental nitrogen diffusion data for both phases of iron. The model quantifies the effect of vacancies, and it was found that both the vacancy concentration and the nitrogen-vacancy ratio can have a large impact on the diffusion speed of nitrogen. A direct method to quantify this impact is provided through the diffusion coefficients of nitrogen in each phase, which are valid in a range of temperatures

($100\text{ }^\circ\text{C} < T < 1538\text{ }^\circ\text{C}$), nitrogen concentrations ($0.1\text{ at.}\% < c_{\text{N}} < 1\text{ at.}\%$ with potential to extrapolate), and vacancy concentrations ($0.01\text{ at.}\% < c_{\text{v}} < 10\text{ at.}\%$). For the considered conditions, it appears that significant deformation ($c_{\text{v}} > 0.01\text{ at.}\%$) is required to disrupt nitrogen diffusion to an extent which is experimentally observable. The predicted upper limit of errors under the conditions examined (see figure 5.8) shows that in most cases, the diffusion coefficients calculated in this work yield an enhanced method for determining nitrogen diffusibility in vacancy-rich iron.

Chapter 6

Nitrogen Concentration Profile

In this chapter, the implications of the modelling work carried out in chapters 4 and 5 are investigated for representative examples of nitriding in α -Fe and γ -Fe. The α -Fe composition reflects common nitriding conditions, as it is the usual composition for the diffusion zone in a nitrided metal. Nitrogen diffusion in γ -Fe also has industrial relevance through austenitic nitriding [99] and high nitrogen steels [100]. A realistic example of an industrial process is outside the scope of the PhD project. This is because generating results which are comparable to experimental data would require the implementation of a layer growth model (see section 3.3.4), which simultaneously calculates solutions to Fick's diffusion equation for all the nitride layers formed in nitriding. In the simplified monolayer model used in this chapter, the nitrogen-dense ϵ and γ' layers which form the hard surface are omitted. This is achieved by keeping the nitrogen activity at the surface small, to the extent that only the α -Fe or γ -Fe compositions are stable. Moreover, the diffusion coefficient is assumed to be independent of the nitrogen concentration, meaning that an analytical solution to Fick's equation is available. This trivialises the calculation of the nitrogen concentration profile in a metal as time passes. Despite the simplicity, it allows one to gain insight into the potential impact of the PhD project in an applied context. In particular, results from the project are used to calculate the impact of vacancies on the nitrogen concentration profile. Predicting the nitrogen concentration profile accurately is vital for modelling nitriding, as the profile is an excellent predictor of the material properties after the treatment.

6.1 Methodology

A *constant source* Fick's law diffusion model is employed to calculate nitrogen concentration profiles, where nitrogen atoms diffuse in from one end of a semi-infinite bar of iron. The function $c(x, t)$ represents the nitrogen concentration at distance (perpendicular to the surface) within the metal x , at time t . The nitrogen concentration at the source $c(0, t) = 0.1$ at.%, is assumed to be constantly replenishing and does not change with time. This is representative of nitriding surface treatment, where the nitrogen concentration at the surface is maintained through equilibrium with the nitriding atmosphere [3]. It is assumed, as a first approximation, that the diffusion coefficient of nitrogen in iron is not dependant on the nitrogen concentration. In this case, Fick's second law is

$$\frac{\partial c}{\partial t} = D(T, c_v) \frac{\partial^2 c}{\partial x^2}. \quad (6.1)$$

and $D(T, c_v) := D$ is the diffusion coefficient of nitrogen, which is constant at a fixed temperature T and vacancy concentration c_v . Provided that the initial nitrogen concentration in the iron bar is zero, the solution to equation 6.1 for $t > 0$ is

$$c(x, t) = c(0, t) \left(1 - \operatorname{erf} \left(\frac{x}{2\sqrt{Dt}} \right) \right). \quad (6.2)$$

Where erf is the *error function*, defined as

$$\operatorname{erf}(x) = \frac{2}{\sqrt{\pi}} \int_0^x e^{-u^2} du. \quad (6.3)$$

The integral in equation 6.3 is solved numerically, as no analytical solution is available.

6.2 Results and Discussion

The parameters used to calculate nitrogen concentration profiles are shown in table 6.1. The diffusion coefficients were calculated at the prescribed conditions and temperatures using the function defined in [9]. Due to the choices of nitrogen concentration (0.1 at.%) and vacancy concentrations (0 at.% and 0.1 at.%), the error margin in the diffusion coefficient is small because it is interpolated directly from diffusion simulation results [9].

The concentration profiles generated are depicted in figures 6.1 (α -Fe) and 6.2 (γ -Fe). Despite the simplicity of the model, which does not consider the ϵ and γ' nitride

Table 6.1: Parameters used to generate nitrogen concentration profiles in a model of nitrogen diffusion in iron. c_N and c_v are the nitrogen and vacancy concentrations respectively. The diffusion coefficient of nitrogen is D .

Phase	t hours	T °C	c_v at.%	$\log_{10}(D)$ [$c_N = 0.1$ at.%]
α -Fe	10	400	0	-8.522
			0.1	-9.188
		600	0	-7.280
			0.1	-7.582
γ -Fe	100	600	0	-10.44
			0.1	-10.74

layers, reasonable agreement with experimental data [101] (α -Fe) [102, 103] (γ -Fe) is observable. In all cases it is clear that a vacancy concentration of 0.1 at.% has a distinct effect on the concentration profile. Although it should be noted that if the nitrogen concentration exceeds the vacancy concentration, the effect will begin to diminish. A vacancy concentration of 0.1 at.% is much higher than one would expect at thermodynamic equilibrium. However, the thermodynamic model [5] suggests that naturally-occurring crystal imperfections cause iron to behave as if it has an excess of vacancies. Moreover, the amount of imperfections would increase if cold-working processes such as machining/peening are applied. Hence, the chosen vacancy concentration is physically relevant in real experimental scenarios.

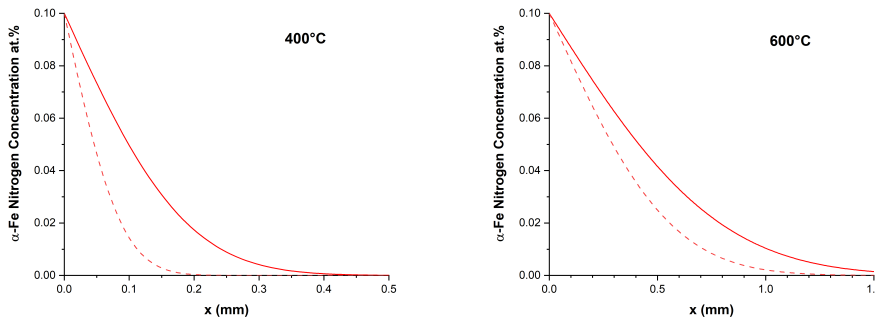


Figure 6.1: Diffusion of nitrogen into a semi-infinite bar of α -iron for 10 hours. The nitrogen concentration at the source where $x = 0$ is fixed at 0.1 at.% throughout time. The solid lines indicate that the iron is vacancy-free, whilst the dashed lines indicate a vacancy concentration of 0.1 at.%. The figures correspond to diffusion temperatures of 400°C and 600°C as labelled.

The nitriding process is typically carried out at $400^\circ\text{C} < T < 600^\circ\text{C}$, as these temperatures are low enough to avoid any thermal degradation of the metal [104]. A post-treatment nitrogen concentration profile which is too flat means that the

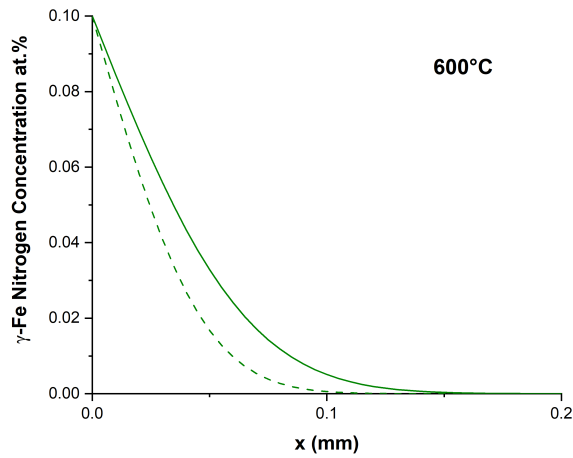


Figure 6.2: Diffusion of nitrogen into a semi-infinite bar of γ -iron for 100 hours. The nitrogen concentration at the source where $x = 0$ is fixed at 0.1 at.% throughout time. The solid lines indicate that the iron is vacancy-free, whilst the dashed lines indicate a vacancy concentration of 0.1 at.%. The diffusion temperature is fixed at 600°C.

treated metal has lost a significant amount of ductility, and is therefore brittle. In contrast, an overly sharp concentration profile reduces the load-bearing performance of the metal, and leads to the egg shell effect. Literature suggests that employing the currently available diffusion coefficients for nitrogen can result in discrepancies between modelled and experimental concentration profiles [30].

Figure 6.1 shows that the concentration profile becomes more uniform and penetrates deeper into the material as the temperature increases. This is because the nitrogen atoms are faster to reach the energetic ideal where $c(x, t) = c(0, t)$ for all $x > 0$. The nitrogen penetration depths calculated for the 400°C and 600°C nitrogen concentration profiles were around 0.5 mm and 1.5 mm respectively. The addition of vacancies creates a significant change at both of the calculated temperatures. Moreover, the shape of the 400°C concentration profile shows a larger change upon the addition of vacancies than the 600°C profile. This is because the diffusion coefficients in table 6.1, where it can be seen that the difference in the diffusion coefficient caused by the addition of vacancies is two times larger at 400°C relative to 600°C. If the current model was expanded to use a diffusion coefficient which is dependent on nitrogen concentration, the effect of vacancies would be more pronounced than currently shown. As x increases and nitrogen penetrates deeper into the material, the concentration of nitrogen atoms decreases. If the vacancy concen-

tration is uniform throughout the metal, the mixing ratio of nitrogen to vacancies would decrease as x increases. The diffusion coefficient is heavily dependent on the mixing ratio of nitrogen to vacancies $\frac{c(x,t)}{c(x,t)+c_v}$. Vacancy-related diffusion effects are more pronounced if $\frac{c(x,t)}{c(x,t)+c_v} < 1$. In contrast, the excess nitrogen begins to dilute the vacancy-related effects if $\frac{c(x,t)}{c(x,t)+c_v} > 1$ [9].

In austenitic nitriding, which is typically carried out at $600^\circ\text{C} < T < 725^\circ\text{C}$ [99], a γ -Fe layer is formed before the α -Fe layer. An important result of the diffusion study in this work [9], is that nitrogen diffusion data was directly calculated in the relevant temperature range (rather than extrapolated) in γ -Fe, where there is no experimental data available. It is difficult to obtain experimental data, because if the solute concentration is low, γ -Fe is unstable at low temperatures (see section 1.2.1). Nitrogen diffusion in γ -Fe is slow compared to α -Fe, which is intuitive because FCC lattices are more densely packed than BCC lattices. As seen by comparing figure 6.2 to figure 6.1, the penetration depth of nitrogen is far smaller despite the diffusion time being ten times larger in γ -Fe. This is potentially dangerous in nitriding, as the γ -Fe layer could prevent sufficient nitrogen from reaching the α -Fe diffusion layer to support the surface. For the conditions investigated, the impact of vacancies is similar for α -Fe and γ -Fe. This is because the temperatures of concern were relatively high. As the temperature increases, the effect of vacancies are gradually diminished to nothing. Hence, the vacancy-related effects associated with α -Fe and γ -Fe are far more distinguishable at low temperatures [9].

Chapter 7

Conclusions and Future Work

The PhD project has met its primary goal of utilising density functional theory (DFT) to increase the clarity and capability of current models for nitriding. This takes the form of several novel contributions to the existing literature surrounding the iron-nitrogen-vacancy system, which are summarised in this chapter. These contributions fall into two main categories, forming two sections in the conclusion. These are: the thermodynamic model, which provides insight into the behaviour of the system once local equilibrium is reached; and the diffusion model, which shows the rate at which nitrogen atoms are dispersed throughout the metal. Finally, the key areas where the work should be extended in the future are highlighted.

7.1 Thermodynamics

7.1.1 Nitrogen-Vacancy Equilibrium

The nitriding potential influences the concentration of vacancies which form at thermodynamic equilibrium [5]. This is due to the formation of nitrogen-vacancy complexes [41], which are defects in the iron which contain some arrangement of nitrogen atoms and vacancies. This work was restricted to complexes with a single vacancy, and the most abundant of these contain three or fewer nitrogen atoms [5]. Since in general, nitrogen is more stable in the proximity of vacancies, increasing the nitriding potential also increases the concentration of vacancies in both α -Fe and γ -Fe. This relationship has been quantified in figure 4.2. It was found that the formation of complexes does not significantly impact the overall nitrogen concentration, as there are far more lone nitrogen defects than complexes under most conditions. However, the model suggests that the overall vacancy concentration can be increased by many orders of a magnitude by increasing the nitrogen activity.

7.1.2 Modelling Crystal Imperfections with Vacancies

Excess Vacancies

One has no way to fine control the vacancy abundance at thermodynamic equilibrium in the same way as nitrogen through the nitriding potential, and the equilibrium quantities of vacancies in iron are low enough to be insignificant in this context [5]. A meaningful discussion of vacancies therefore requires that they are far in excess of their equilibrium quantity. These excess vacancies are not strictly considered as lone point defects. In particular, the current model investigated the credibility of treating the concentration of vacancies as effectively equivalent to the proportion of *imperfection* of the lattice. In essence, the excess space caused by the variety of defects and grains which naturally occur in iron, are approximated to behave similarly to collections of independent vacancies. Evidence was found both with regards to nitrogen solubility and phase stability, which validates this assumption.

Nitrogen Solubility

To calculate the energetic properties of the nitriding reaction (see 4.1) from first principles, it is natural to first calculate equilibrium data from ideal BCC or FCC iron supercells. That is, where the respective crystal structures are arranged with perfect symmetry without defects. According to the current work [5], the thermodynamic model which uses idealised structures underestimates the experimental solubility with $p_{\text{N}_2} = 1$ atm in both α -Fe and γ -Fe. Some degree of systematic error is expected from applying DFT (see section 3.1.5), but this uncertainty was quantified in the work and the discrepancy between the experimental and calculated data was well outside of the anticipated margin for error.

Vacancy trapping of nitrogen atoms in iron is an intuitive phenomenon. Vacancies are unoccupied space in an otherwise efficiently packed lattice. Thus, it is energetically desirable for nitrogen atoms to migrate to this space and fill it. The nitrogen also has a stabilising effect on vacancies, so it is favourable for the nitrogen concentration to increase in the lattice if vacancies are abundant. When this effect is quantified using the calculated results, the discrepancies in the solubility data can be resolved (see figure 4.3). That is, one can deduce that the inherent imperfections in real iron are responsible for the larger nitrogen solubility in experimental data compared to the model-calculated solubility.

Phase Stability

The model-calculated α - γ phase boundary in the Lehrer diagram was found to disagree with the experimental data, even when taking the expected uncertainty into account. Namely, the calculated boundary indicates a larger range of stable conditions for α -Fe than is indicated by current literature. This discrepancy only applies in the vacancy-free case, because vacancies can be used to increase the phase stability of both α -Fe and γ -Fe in an atmosphere with high nitrogen activity. That is, increasing the concentration of vacancies in either phase will expand its stability to a larger range of nitriding potentials and temperatures (see figure 4.5). Changing the vacancy concentration in either of the phases shifts the phase boundary. As seen in figure 4.6, if one allows for a proportion of vacancies in each phase to represent crystal imperfections, the phase boundary matches the experimental data over the appropriate temperature range.

Model Validity

In both the solubility and phase stability calculations, the disagreement between the model-calculated data and experimental data was beyond the expected margin for error. This indicates that at some point the assumptions of the model, at least in the vacancy-free case, were not appropriate for the accuracy required. The vacancy formation energies for both α -Fe and γ -Fe were found to be underestimated in DFT-calculations, compared to experimentally derived (through positron annihilation) values [5]. This is a strong indicator that the model with excess vacancies is closer to reality. The introduction of vacancies corrects the deviations from experimental data in both instances mentioned, indicating it is a necessary element to include in thermodynamic models for the iron nitrogen system. Ideally this should be verified in future work by bespoke experiments, as it could be argued that the vacancy inclusion is correcting discrepancies which are not necessarily vacancy related. In absence of direct experimental evidence, it is prudent to discuss other possible sources of the deviations. The most significant factors in this regard are as follows:

- As discussed in 3.1.3, the accuracy of any DFT calculation is subject to a well chosen exchange-correlation functional. Since exploration of the functional choice was outside the scope of this work, the use of the PBE functional in this work was justified by its frequent successful application for similar systems in previous work. It is important to note that older works would, in general, have less computing capacity. The uncertainty resulting from other

DFT parameters will tend to decrease as the computing power is increased. Hence, there is an increasing chance that the functional choice becomes the bottleneck for the accuracy of the calculation.

- In practice, even high-purity iron in experiments contains a variety of alloy and interstitial elements (carbon being the most prominent example) in non-negligible amounts. Due to the complexity of these impurities, it is not clear to what extent they affect the thermodynamic behaviour of nitrogen in iron, and a full treatment of them using DFT was outside the reach of this work. This is also the reason the experimental data often has a significant spread when comparing between multiple sources. The iron samples are unlikely to share exactly identical compositions in terms of defects, although it is also important to note that these experiments may be decades apart which creates variations in methodology and equipment.
- The vibrational energy contributions in the model were calculated by treating nitrogen interstitial atoms as independent harmonic oscillators, rather than computing the full phonon densities of nitrogen-containing systems (see section 3.2.1). Due to the computational expense of full-phonon calculations, there are limited sources comparing the difference between the two approaches. For α -Fe, the distinction between calculating full phonon densities over using the vibrational approximation has been shown to be significant [44].

A sensitivity analysis [5] showed that when considering the largest (closest to experimental data points) solubility curve within the model uncertainty (see figure 4.3), an additional average overestimation of 14.9 kJ mol^{-1} (α -Fe) and 10.5 kJ mol^{-1} (γ -Fe) in the internal energy for the nitrogen defect would be required for the calculated solubility to agree with the experimental data. In other words, to discount the theory that vacancy-related effects cause the discrepancies between calculated and experimental solubility data, the internal energy calculations would have to be refined by an average of 14.9 kJ mol^{-1} (α -Fe) and 10.5 kJ mol^{-1} (γ -Fe) over the temperature range by some means which is not accounted for in the current model. Further exploration of the three points above are required to investigate if they are capable of causing errors of this magnitude. As it currently stands, the evidence supports the theory of a vacancy-rich model. Both by the high magnitude of the deviations from the experimental data, and the consistent way that the solubility of nitrogen is underestimated such that it can be corrected by increasing the vacancy concentration.

7.2 Diffusion

7.2.1 Thermal Expansion

Iron exhibits significant expansion when it is heated. This effect changes the lattice spacing and subsequently, influences the energy barrier for atomic nitrogen jumps (see section 3.3.1). In essence, the energy barrier should be temperature dependent. In α -Fe, thermal expansion was not found to have a significant impact on diffusion (see figure 5.5). However, in γ -Fe the impact was substantial. It was essential to include thermal expansion in the diffusion model for γ -Fe, otherwise there is a large discrepancy between the model result and experimental data [9]. This discovery could resolve a long-standing issue in literature with models for both nitrogen and carbon diffusion in γ -Fe. Non-magnetic models of FCC Fe, used to represent γ -Fe in this work, are not the typical choice to investigate interstitial diffusion in γ -Fe because it has not previously been justified by agreement with experimental data. This work has shown that, provided that thermal expansion is considered, the non-magnetic model is appropriate [9].

7.2.2 Impact of Vacancies

Previous work has established that in both α -Fe and γ -Fe, due to the attraction between nitrogen atoms and vacancies, vacancies have a trapping effect which slows nitrogen diffusion. In the current work, the trapping effect is quantified over a range of vacancy concentrations, nitrogen concentrations, and temperatures, by characterising a diffusion coefficient for both α -Fe and γ -Fe which depends on the three variables [9]. The diffusion coefficient allows for experimental verification, and ultimately the improvement of existing nitriding models. Since vacancy-rich iron can have a diffusion coefficient several orders of magnitude smaller than vacancy-free iron (see figure 5.6), the diffusion coefficient characterised in this work offers potentially much higher accuracy than one which does not consider vacancies. In contrast to experimental solubility data, the experimental diffusion data shows relatively strong agreement to the vacancy-free model. However, there are exceptions where the experimental and calculated diffusion data deviates. As seen in figure 5.6, there are diffusion-enhancing magnetic effects in α -Fe [9] which become significant at temperatures above 400°C. The experimental diffusion data which the model is compared to was generated from conditions with a higher nitrogen activity than $p_{\text{N}_2} = 1$ atm, and accordingly higher nitrogen concentrations than shown in the solubility data from figure 4.3. In general, if the ratio of vacancies to nitrogen atoms is sufficiently small, a minimal effect on nitrogen diffusion will be observed.

This is because nitrogen atoms within the lattice are repulsive to each other, so vacancies make less potent traps if they are overly saturated. Hence, a diffusion coefficient which depends on the vacancy concentration should also be dependent on the nitrogen concentration.

7.3 Future Work

7.3.1 DFT Accuracy

A recurring theme in DFT studies is that increased computing capability reduces uncertainty, and this work is no exception. There is potential to reduce the error margin in both the thermodynamic and diffusion results if one has access to enough resources. In particular, refining the calculations with respect to the DFT parameters outlined in chapter 4 would decrease the uncertainty by up to 0.1 eV. Using larger supercells in both the α -Fe and γ -Fe systems has the largest impact in this regard, although the computational cost of DFT increases on a cubic scale with respect to the supercell size. An alternative to the plane-wave variant of DFT, which solves the system on a real-space grid, scales more efficiently with increased supercell size [66, 67]. This is because real-space solvers parallelise more efficiently over multiple computing cores. The DFT literature which applies real-space solvers is sparser than for plane-wave solvers, because the former method is newer. Thus, an investigation into real-space solvers would be a significant contribution to knowledge. Reducing the error margin in the current DFT calculations is a valuable step in validating the model results against experimental data and understanding the cause of discrepancies, which are substantial in the solubility case (see section 7.1.2). More involved adjustments to the current model should also be tested to assess their impact on accuracy. The full phonon density of states should be incorporated into the calculations to compare with the current results which employ the computationally cheaper vibrational approximation. The effect of different exchange-correlation functionals such as rev-PBE [105] should be explored, as the majority of literature covering this system employs the standard PBE functional. Moreover, the effect of using hybrid functionals [106] to minimise self-interaction error in the coulomb repulsion term of the Kohn-Sham formulation (see section 3.1.2) should be tested. Hybrid functionals have not been used so far in DFT calculations with iron nitrides, but they are considered essential in calculations with iron oxides [55].

7.3.2 Experimental Verification of Vacancy-Rich Model

To validate both the thermodynamic and diffusion models in the vacancy-rich case, new experimental data is required for comparison. Generating such experimental data is challenging because there are not currently well established methods to induce or measure a given concentration of vacancies in iron. However, the current work is a reference which allows investigation of the degree of deformation caused by various cold-working processes. For instance, supposing that a process is found to slow the diffusion speed of nitrogen, the diffusion coefficient (visualised in figure 5.6) could then be used to quantify the proportion of deformation caused by the process. Furthermore, assuming that the temperature does not affect the degree of deformation, one can use a single observation to predict the effect that an arbitrary amount of deformation will have at any temperature in the model range. Provided that a good approximation of the level of deformation is known, the vacancy-dependent diffusion coefficient, as defined in [9], can be used to implement a layer growth model (see chapter 6). Once the model is verified against experimental data, this will lead to more robust models for the nitriding process than are currently available. Due to the popularity of nitriding, this has potentially far-reaching consequences of improving the longevity of treated metals, limiting adverse environmental effects, and reducing costs.

7.3.3 Improvements to the Diffusion Model

The diffusion coefficient of nitrogen depends on the nitrogen concentration within an iron lattice [88]. This is a particularly important consideration for γ -Fe, because it is the phase present in high-nitrogen steels [100]. It is important to note that while the diffusion coefficient developed in this work is dependent on nitrogen concentration, this is only to consider its ratio with respect to the vacancy concentration. In order to improve the robustness of the current diffusion model in nitrogen-rich conditions, further investigation is required. It has been shown in this work that thermal expansion has a large influence on the diffusion energy barrier in γ -Fe (see figure 5.3), because the barrier is heavily dependent on volume. It is therefore important to explore other forms of lattice expansion, such as the expansion caused by increasing the nitrogen concentration [6]. In α -Fe, there is the added complication that nitrogen interstitials cause a local tetragonal distortion. As the nitrogen concentration increases, the assumption of a perfectly cubic lattice in KMC simulations deviates from reality. The effect that this loss of symmetry has on nitrogen diffusion is not quantified in current literature. However, there are analogous models which have

been designed for this purpose in carbon interstitials [97], which also form tetragonal distortions in α -Fe. Since the behaviour of carbon and nitrogen interstitials in iron are similar, the existing theory could be used to extend the current nitrogen diffusion model.

7.3.4 Extension to Other Interstitial elements

Carbon based heat treatments such as carburising and nitrocarburising are among the most important processes in tertiary steelmaking. Since the majority of the methodology employed in this work to study the iron-nitrogen-vacancy system would also be applicable to the iron-carbon-vacancy system, a natural extension of the work is to carry out a similar study of carbon. Literature suggests [46] that, similar to nitrogen, vacancies are attractive to interstitial carbon atoms in iron. This creates competition between nitrogen and carbon atoms for the energetically favourable sites around vacancies. It is likely that this would decrease the trapping potency of vacancies that was found with the current model, as the effect of the vacancies would be *shared out* by both nitrogen and carbon. On the other hand, the formation of carbon-nitrogen-vacancy complexes may be more favourable than the formation of nitrogen/carbon-vacancy complexes, which would increase the trapping potency of vacancies. Since carbon is the most common interstitial element in iron, this would have large implications on the current state of the art in modelling.

Oxygen is an important element in steelmaking, because it is central to *basic oxygen steelmaking* [107], which is used to control the carbon content of molten iron. The majority of oxygen is removed before the steel is solidified, because oxygen reacts with carbon during solidification and forms carbon monoxide. The entrapment of gas in the metal creates blowholes, which reduces the quality of the steel [108]. Oxygen interstitials have been shown in DFT studies to have similar thermodynamic and diffusion properties to carbon and nitrogen [42, 46]. However, the carbon-oxygen interaction [109] has yet to be investigated from first principles. To extend the current modelling approach for oxygen interstitials, the DFT+U method or a hybrid functional should be used. This is because iron oxides are thought to have a significant self-interaction error in Kohn Sham DFT (see section 3.1.2).

Bibliography

- [1] D. Gualtieri. 3d-printing stainless steel. 2017. URL http://www.tikalon.com/blog/blog.php?article=2017/3D_stainless [accessed: 16.11.2020].
- [2] Saraz. History and overview of nitriding. 2017. URL <https://www.sarazhandpans.com/handpan-construction/handpan-and-pantam-nitriding/> [accessed: 16.11.2020].
- [3] J.T.Slycke, E.J.Mittemeijer, and M.A.J.Somers. 1 - Thermodynamics and kinetics of gas and gas–solid reactions. In *Thermochemical Surface Engineering of Steels*, pages 3–111. Woodhead Publishing, Oxford, 2015.
- [4] G. Henkelman, B.P. Uberuaga, and H. Jónsson. A climbing image nudged elastic band method for finding saddle points and minimum energy paths. *The Journal of Chemical Physics*, 113(22):9901–9904, 2000.
- [5] A Karimi and M Auinger. Thermodynamics of the iron-nitrogen system with vacancies. from first principles to applications. *Journal of Alloys and Compounds*, 821:153343, 2020.
- [6] H.A. Wriedt, N.A. Gokcen, and R.H. Nafziger. The Fe-N (Iron-Nitrogen) system. *Bulletin of Alloy Phase Diagrams*, 8(4):355–377, 1987.
- [7] Z. You, M.K. Paek, and I.H. Jung. Critical evaluation and optimization of the Fe-N, Mn-N and Fe-Mn-N systems. *Journal of Phase Equilibria and Diffusion*, 39(5):650–677, 2018.
- [8] C. W. Bale, P. Chartrand, E. Bélisle, S. A. Deckerov, G. Eriksson, A.E. Gheribi, K. Hack, I. H. Jung, Y. B. Kang, J. Melançon, A. D. Pelton, S. Petersen, C. Robelin, J. Sangster, P. Spencer, and M-A. Van Ende. Factsage thermochemical software and databases. *Calphad*, 54:35–53, 2016.

- [9] A Karimi and M Auinger. Nitrogen diffusion in vacancy-rich ferrite and austenite, from first principles to applications. *Acta Materialia*, page 117292, 2021.
- [10] M.L. Wasz and R.B. McLellan. Nitrogen diffusion in bcc iron. *Scripta Metallurgica et Materialia*, 28:1461–1463, 1993.
- [11] P. Grieveson and E.T. Turkdogan. Iron and steel division - kinetics of reaction of gaseous nitrogen with iron part i: Kinetics of nitrogen solution in gamma iron. *The American Institute of Mining, Metallurgical, and Petroleum Engineers*, 230:1604, 1964.
- [12] L.Barrallier. 10 - Classical nitriding of heat treatable steel. In *Thermochemical Surface Engineering of Steels*, pages 393–412. Woodhead Publishing, Oxford, 2015.
- [13] R.A. Mesquita. *Tool Steels: Properties and Performance*. CRC Press, 2016.
- [14] M.A.J. Somers, R.M. Lankreijer, and E.J. Mittemeijer. Excess nitrogen in the ferrite matrix of nitrided binary iron-based alloys. *Philosophical Magazine A*, 59:353–378, 2006.
- [15] M. Auinger and M. Rohwerder. Coupling diffusion and thermodynamics - exemplified for the gas nitriding of iron-chromium alloys. *HTM Journal of Heat Treatment and Materials*, 66:100–102, 2011.
- [16] Y. Deng, C. Tan, Y. Wang, L. Chen, P. Cai, T. Kuang, S. Lei, and K. Zhou. Effects of tailored nitriding layers on comprehensive properties of duplex plasma-treated altin coatings. *Ceramics International*, 43, 04 2017.
- [17] O. Kessler, F. Hoffmann, and P. Mayr. The role of cvd parameters in producing the “eggshell” effect during the coating of steel. *Chemical Vapor Deposition*, 6(5):253–259, 2000.
- [18] E Lehrer. Magnetic investigation of the system iron-nitrogen. *Z. Elektrochem.*, 36(7):460–473, 1930.
- [19] G. Stein and I. Hucklenbroich. Manufacturing and applications of high nitrogen steels. *Materials and Manufacturing Processes*, 19(1):7–17, 2004.
- [20] R.C. Shivamurthy, M. Kamaraj, R. Nagarajan, S.M. Shariff, and G. Padmanabham. Laser surface modification of steel for slurry erosion resistance

in power plants. In *Laser Surface Modification of Alloys for Corrosion and Erosion Resistance*, Metals and Surface Engineering, chapter 7, pages 177 – 287. Woodhead Publishing, 2012.

- [21] T. Hirsch, T.G.R. Clarke, and A. da Silva Rocha. An in-situ study of plasma nitriding. *Surface and Coatings Technology*, 201(14):6380 – 6386, 2007.
- [22] J-O Andersson, Thomas Helander, Lars Höglund, Pingfang Shi, and Bo Sundman. Thermo-calc & dictra, computational tools for materials science. *Calphad*, 26(2):273–312, 2002. ISSN 0364-5916.
- [23] P. Cavaliere, G. Zavarise, and M. Perillo. Modeling of the carburizing and nitriding processes. *Computational Materials Science*, 46(1):26–35, 2009.
- [24] F N Jespersen, J H Hattel, and M A J Somers. Modelling the evolution of composition-and stress-depth profiles in austenitic stainless steels during low-temperature nitriding. *Modelling and Simulation in Materials Science and Engineering*, 24(2):025003, 2016.
- [25] K. Dawi, C.-W. He, M.-F. Barthe, P. Desgardin, and A. Volgin. Vacancy defects study in fe based alloys induced by irradiation under various conditions. *Journal of Physics: Conference Series*, 505:012007, 2014.
- [26] N. Igata, R. Hasiguti, and S. Seto. Behaviors of nitrogen atoms in irradiated iron and iron alloy revealed by internal friction and electron microscopy. *Trans. Iron Steel Inst. Jap.*, 10:21–24, 1970.
- [27] T.R Anthony. Solute segregation in vacancy gradients generated by sintering and temperature changes. *Acta Metallurgica*, 17(5):603–609, 1969. ISSN 0001-6160.
- [28] A. Gariépy, H. Miao, and M. Lévesque. 3.12 - peen forming. In Saleem Hashmi, Gilmar Ferreira Batalha, Chester J. Van Tyne, and Bekir Yilbas, editors, *Comprehensive Materials Processing*, pages 295 – 329. Elsevier, Oxford, 2014.
- [29] Xiaohu Deng and Dongying Ju. Prediction of Phase Composition and Nitrogen Concentration During the Nitriding Process in Low-Alloy Steel. *Materials Research*, 19:353 – 359, 04 2016.
- [30] Xiaohu Deng, Dong-ying Ju, and Min Li. Finite Element Modeling and Experimental Verification of Nitriding Process in S30C Steel. *Materials Research*, 20:509 – 513, 04 2017.

- [31] F. Bottoli, G. Winther, T.L. Christiansen, K.V. Dahl, and M.A.J. Somers. Low-temperature nitriding of deformed austenitic stainless steels with various nitrogen contents obtained by prior high-temperature solution nitriding. *Metallurgical and Materials Transactions A*, 47:4146–4158, 2016.
- [32] M. Auinger, E.M. Müller-Lorenz, and M. Rohwerder. Modelling and experiment of selective oxidation and nitridation of binary model alloys at 700°C - the systems Fe, 1wt.%{Al, Cr, Mn, Si}. *Corrosion Science*, 90:503–510, 2015.
- [33] B.J. Kooi, M.A.J. Somers, and E.J. Mittemeijer. An evaluation the Fe-N phase diagram of considering long-range order of N atoms in $\gamma' - Fe_{4n1-x}$ and $\epsilon - Fe_{2n1-z}$. *Metallurgical and Materials Transactions A*, 27A(4):1063–1071, 1996.
- [34] H. Du. A reevaluation of the Fe-N and Fe-C-N systems. *Journal of Phase Equilibria*, 14(6):682–693, 1993.
- [35] K. Frisk. A new assessment of the Fe-N phase diagram. *CALPHAD*, 11(2):127–134, 1987.
- [36] J.R.G. da Silva and R.B. McLellan. Diffusion of carbon and nitrogen in b.c.c. iron. *Materials Science and Engineering*, 26(1):83–87, 1976.
- [37] J. H. Swisher and E. T. Turkdogan. Solubility, permeability and diffusivity of oxygen in solid iron. *The American Institute of Mining, Metallurgical, and Petroleum Engineers*, Jan 1968.
- [38] C. A. Wert. Diffusion coefficient of C in α -iron. *Phys. Rev.*, 79:601–605, Aug 1950.
- [39] H. Mehrer. *Diffusion in Solids: Fundamentals, Methods, Materials, Diffusion-Controlled Processes*. Springer Series in Solid-State Sciences. Springer Berlin Heidelberg, 2007.
- [40] A.L. Nikolaev and T.E. Kurennykh. On the interaction between radiation-induced defects and foreign interstitial atoms in α -iron. *Journal of Nuclear Materials*, 414(3):374–381, 2011.
- [41] F. Walz, H. J. Blythe, and H. Kronmüller. Binding enthalpies of nitrogen-vacancy complexes in irradiated α -Fe. *Radiation Effects and Defects in Solids*, 116(4):339–352, 1991.

- [42] C. Barouh, T. Schuler, C.C. Fu, and M. Nastar. Interaction between vacancies and interstitial solutes (C, N, and O) in α -Fe: From electronic structure to thermodynamics. *Physical Review B*, 90:054112, 2014.
- [43] S. Sakuraya, K. Takahashi, N. Hashimoto, and S. Ohnuki. The effect of point defects on diffusion pathway within α -Fe. *Journal of Physics Condensed Matter*, 27:175007, 2015.
- [44] S.D. Waele, K. Lejaeghere, E. Leunis, L. Duprez, and S. Cottenier. A first-principles reassessment of the Fe-N phase diagram in the low-nitrogen limit. *Journal of Alloys and Compounds*, 775:758–768, 2019.
- [45] T. Schuler, C. Barouh, M. Nastar, and C.C. Fu. Equilibrium vacancy concentration driven by undetectable impurities. *Physical review letters*, 115:015501, 2015.
- [46] C. Barouh, T. Schuler, C.C. Fu, and T. Jourdan. Predicting vacancy-mediated diffusion of interstitial solutes in α -Fe. *Phys. Rev. B*, 92:104102, 2015.
- [47] M.H. Wu, X.H. Liu, J.F. Gu, and Z.H. Jin. Dft study of nitrogen-vacancy complexions in (fcc) Fe. *Modelling and Simulation in Materials Science and Engineering*, 22:055004, 2014.
- [48] F. Ye, K. Tong, Y.K. Wang, Z. Li, and F. Zhou. First-principles study of interaction between vacancies and nitrogen atoms in fcc iron. *Computational Materials Science*, 149:65–72, 2018.
- [49] D.S. Sholl and J.A. Steckel. *Density Functional Theory: A practical introduction*. John Wiley & Sons, Ltd, 2009.
- [50] M. Born and R. Oppenheimer. Zur quantentheorie der molekeln. *Annalen der Physik*, 389(20):457–484, 1927.
- [51] P. Hohenberg and W. Kohn. Inhomogeneous electron gas. *Phys. Rev.*, 136: B864–B871, Nov 1964.
- [52] W. Kohn and L. J. Sham. Self-consistent equations including exchange and correlation effects. *Phys. Rev.*, 140:A1133–A1138, Nov 1965.
- [53] J.P. Perdew, K. Burke, and M. Ernzerhof. Generalized gradient approximation made simple. *Phys. Rev. Lett.*, 77:3865–3868, 1996.

- [54] S. Dick and M. Fernandez-Serra. Machine learning accurate exchange and correlation functionals of the electronic density. *Nat Commun*, 2020.
- [55] Y. Meng, X-W. Liu, C-F. Huo, W-P. Guo, D-B. Cao, Q. Peng, A. Dearden, X. Gonze, Y. Yang, J. Wang, H. Jiao, Y. Li, and X-D. Wen. When density functional approximations meet iron oxides. *Journal of Chemical Theory and Computation*, 12(10):5132–5144, 2016.
- [56] J. Heyd, G.E. Scuseria, and M. Ernzerhof. Hybrid functionals based on a screened coulomb potential. *The Journal of chemical physics*, 118(18):8207–8215, 2003.
- [57] S. Tolba, K. Gameel, A.B. Ali, H.A. Almossalami, and N.K. Allam. The dft+u: Approaches, accuracy, and applications, density functional calculations. *IntechOpen*, 2018.
- [58] J-S. Chen, C. Yu, and H. Lu. Phase stability, magnetism, elastic properties and hardness of binary iron nitrides from first principles. *Journal of Alloys and Compounds*, 625:224–230, 2015.
- [59] G. Kresse and D. Joubert. From ultrasoft pseudopotentials to the projector augmented-wave method. *Phys. Rev. B*, 59:1758–1775, Jan 1999.
- [60] P. Ehrhart, B. Schönfeld, H.H. Ettwig, and W. Pepperhoff. The lattice structure of antiferromagnetic γ -iron. *Journal of Magnetism and Magnetic Materials*, 22(1):79 – 85, 1980.
- [61] W. Kümmerle and U. Gradmann. Ferromagnetism in γ -iron. *Solid State Communications*, 24(1):33 – 35, 1977.
- [62] K. Knöpfle, L. M. Sandratskii, and J. Kübler. Spin spiral ground state of γ -iron. *Phys. Rev. B*, pages 5564–5569, Sep 2000.
- [63] C. Kittel. *Introduction to Solid State Physics*. Wiley, 2004.
- [64] H.J. Monkhorst and J.D. Pack. Special points for brillouin-zone integrations. *Phys. Rev. B*, 13:5188–5192, 1976.
- [65] M. Methfessel and A.T. Paxton. High-precision sampling for brillouin-zone integration in metals. *Phys. Rev. B*, 40:3616–3621, 1989.
- [66] J.J. Mortensen, L.B. Hansen, and K.W. Jacobsen. Real-space grid implementation of the projector augmented wave method. *Phys. Rev. B*, 71:035109, 2005.

- [67] J. Enkovaara, C. Rostgaard, J.J. Mortensen, J. Chen, M. Dulak, L. Ferrighi, J. Gavnholt, C. Glinsvad, V. Haikola, H.A. Hansen, H.H. Kristoffersen, M. Kuisma, A.H. Larsen, L. Lehtovaara, M.L. Jungberg, O. Lopez-Acevedo, P.G. Moses, J. Ojanen, T. Olsen, V. Petzold, N.A. Romero, J. Stausholm-Müller, M. Strange, G.A. Tritsarlis, M. Vanin, M. Walter, B. Hammer, H. Häkkinen, G.K.H. Madsen, R.M. Nieminen, J.K. Nørskov, M. Puska, T.T. Rantala, J. Schitz, K.S. Thygesen, and K.W. Jacobsen. Electronic structure calculations with GPAW: a real-space implementation of the projector augmented-wave method. *Journal of Physics: Condensed Matter*, 22(25):253202, 2010.
- [68] A.H. Larsen, J.J. Mortensen, J. Blomqvist, I.E. Castelli, R. Christensen, M. Dulak, J. Friis, M.N. Groves, B. Hammer, C. Hargus, E.D. Hermes, P.C. Jennings, P.B. Jensen, J. Kermode, J.R. Kitchin, E.L. Kolsbjerg, J. Kubal, K. Kaasbjerg, S. Lysgaard, J.B. Maronsson, T. Maxson, T. Olsen, L. Pastewka, A. Peterson, C. Rostgaard, J. Schiøtz, O. Schütt, M. Strange, K.S. Thygesen, T. Vegge, L. Vilhelmsen, M. Walter, Z. Zeng, and K.W. Jacobsen. The atomic simulation environment—a Python library for working with atoms. *Journal of Physics: Condensed Matter*, 29(27):273002, 2017.
- [69] R. Fletcher. *Newton-Like Methods*, chapter 3, pages 44–79. John Wiley & Sons, Ltd, 2013.
- [70] C.J. Forst, J. Slycke, K.J.V. Vliet, and S. Yip. Point defect concentrations in metastable Fe-C alloys. *Phys. Rev. Lett.*, 96:175501, 2006.
- [71] T Frederiksen, M Paulsson, M Brandbyge, and A-P Jauho. Inelastic transport theory from first principles: Methodology and application to nanoscale devices. *Phys. Rev. B*, 75:205413, May 2007.
- [72] Z.S. Basinski, W. Hume-Rothery, and A.L. Sutton. The lattice expansion of iron. *Proceedings of the Royal Society of London. Series A, Mathematical and Physical Sciences*, 229(1179):459–467, 1955.
- [73] A Togo and I Tanaka. First principles phonon calculations in materials science. *Scr. Mater.*, 108, Nov 2015.
- [74] A.T. Dinsdale. SGTE data for pure elements. *Calphad*, 15(4):317 – 425, 1991.
- [75] K.K. Irikura. Experimental vibrational zero-point energies: Diatomic molecules. *Journal of Physical and Chemical Reference Data*, 36:389–397, 2007.

- [76] S. Smidstrup, A. Pedersen, K. Stokbro, and H. Jónsson. Improved initial guess for minimum energy path calculations. *The Journal of Chemical Physics*, 140(21):214106, 2014.
- [77] P. Lindgren, G. Kastlunger, and A.A. Peterson. Scaled and dynamic optimizations of nudged elastic bands. *Journal of Chemical Theory and Computation*, 15(11):5787–5793, 2019.
- [78] M. Andersen, C. Panosetti, and K. Reuter. A practical guide to surface kinetic monte carlo simulations. *Frontiers in Chemistry*, 7, Apr 2019.
- [79] M Leetmaa and N. V. Skorodumova. KMCLib: A general framework for lattice kinetic monte carlo (KMC) simulations. *Computer Physics Communications*, 185(9):2340 – 2349, 2014.
- [80] H. Jónsson, G. Mills, and K.W. Jacobsen. *Nudged elastic band method for finding minimum energy paths of transitions*, pages 385–404.
- [81] E. Bitzek, P. Koskinen, F. Gähler, M. Moseler, and P. Gumbsch. Structural relaxation made simple. *Phys. Rev. Lett.*, 97:170201, 2006.
- [82] M.W. Chas. *NIST-JANAF thermochemical tables*. American Institute of Physics for the National Institute of Standards and Technology, 4th edition edition, 1998.
- [83] M.H. Wu, X.H. Liu, J.F. Gu, and Z.H. Jin. First-principles simulations of iron with nitrogen: from surface adsorption to bulk diffusion. *Modelling and Simulation in Materials Science and Engineering*, 21(4):045004, 2013.
- [84] R. Nazarov, T. Hickel, and J. Neugebauer. First-principles study of the thermodynamics of hydrogen-vacancy interaction in fcc iron. *Physical Review B*, 82:224104, 2010.
- [85] S.M. Kim and W.J.L. Buyers. Vacancy formation energy in iron by positron annihilation. *Journal of Physics F: Metal Physics*, 8(5):L103–L108, 1978.
- [86] T. Schuler, M. Nastar, and F. Soisson. Vacancy-induced dissolution of precipitates in out-of-equilibrium systems: A test case of Fe(x) (x = C, N, O) alloys. *Physical Review B*, 95:014113, 2017.
- [87] T. Schuler and M. Nastar. Transport properties of dilute α -Fe(x) solid solutions (x = C, N, O). *Phys. Rev. B*, 93:224101, Jun 2016.

- [88] S. Mändl and B. Rauschenbach. Concentration dependent nitrogen diffusion coefficient in expanded austenite formed by ion implantation. *Journal of Applied Physics*, 91(12):9737–9742, 2002.
- [89] D. Jiang and E.A. Carter. Carbon dissolution and diffusion in ferrite and austenite from first principles. *Phys. Rev. B*, 67:214103, 2003.
- [90] K Ferasat, Y N. Osetsky, A V. Barashev, Y Zhang, and Z Yao. Accelerated kinetic monte carlo: A case study; vacancy and dumbbell interstitial diffusion traps in concentrated solid solution alloys. *The Journal of Chemical Physics*, 153(7):074109, 2020.
- [91] B Puchala, M L. Falk, and K Garikipati. An energy basin finding algorithm for kinetic monte carlo acceleration. *The Journal of Chemical Physics*, 132(13):134104, 2010.
- [92] C Daniels and P Bellon. Hybrid kinetic monte carlo algorithm for strongly trapping alloy systems. *Computational Materials Science*, 173:109386, 2020.
- [93] M. Leetmaa and N.V. Skorodumova. Mean square displacements with error estimates from non-equidistant time-step kinetic monte carlo simulations. *Computer Physics Communications*, 191:119–124, 2015.
- [94] B.J. Lee, T.H. Lee, and S.J. Kim. A modified embedded-atom method interatomic potential for the fe–n system: A comparative study with the fe–c system. *Acta Materialia*, 54(17):4597–4607, 2006.
- [95] J.H. Bott, H. Yin, S. Sridhar, and M. Auinger. Theoretical and experimental analysis of selective oxide and nitride formation in fe-al alloys. *Corrosion Science*, 91:37–45, 2015.
- [96] M. Nikolussi, A. Leineweber, and E.J. Mittemeijer. Nitrogen diffusion through cementite layers. *Philosophical Magazine*, 90(9):1105–1122, 2010.
- [97] B Lawrence, C W Sinclair, and M Perez. Carbon diffusion in supersaturated ferrite: a comparison of mean-field and atomistic predictions. *Modelling and Simulation in Materials Science and Engineering*, 22(6):065003, 2014.
- [98] J. Aufrecht, A. Leineweber, J. Foct, and E.J. Mittemeijer. The structure of nitrogen-supersaturated ferrite produced by ball milling. *Philosophical Magazine*, 88(12):1835–1855, 2008.

- [99] R.S.E. Schneider. 9 - Austenitic nitriding and nitrocarburizing of steels. In *Thermochemical Surface Engineering of Steels*, pages 373–400. Woodhead Publishing, Oxford, 2015.
- [100] V.G. Gavriljuk and H. Berns. *High Nitrogen Steels: Structure, Properties, Manufacture, Applications*. Engineering Materials. Springer Berlin Heidelberg, 2013.
- [101] Arthur Bramley, Frederick Wardle Haywood, Arthur Thomas Cooper, and John Thomas Watts. The diffusion of non-metallic elements in iron and steel. *Trans. Faraday Soc.*, 31:707–734, 1935.
- [102] T. Christiansen, K. V. Dahl, and M. A. J. Somers. Nitrogen diffusion and nitrogen depth profiles in expanded austenite: experimental assessment, numerical simulation and role of stress. *Materials Science and Technology*, 24(2):159–167, 2008.
- [103] R. Hales and A. C. Hill. The diffusion of nitrogen in an austenitic stainless steel. *Metal Science*, 11(7):241–244, 1977.
- [104] K.M.Winter, J.Kalucki, and D.Koshel. 3 - Process technologies for thermochemical surface engineering. In *Thermochemical Surface Engineering of Steels*, pages 141–206. Woodhead Publishing, Oxford, 2015.
- [105] B. Hammer, L. B. Hansen, and J. K. Nørskov. Improved adsorption energetics within density-functional theory using revised Perdew-Burke-Ernzerhof functionals. *Phys. Rev. B*, 59:7413–7421, Mar 1999.
- [106] J. Heyd and G.E. Scuseria. Efficient hybrid density functional calculations in solids: Assessment of the heyd–scuseria–ernzerhof screened coulomb hybrid functional. *The Journal of Chemical Physics*, 121(3):1187–1192, 2004.
- [107] D. Sichen. 9 - improving process design in steelmaking. In Seshadri Seetharaman, editor, *Fundamentals of Metallurgy*, Woodhead Publishing Series in Metals and Surface Engineering, pages 369–398. Woodhead Publishing, 2005.
- [108] W. Newell. Application of oxygen to steel-making. *Nature*, 162:518–519, 1948.
- [109] M.Y. Solar and R.I.L. Guthrie. Kinetics of the carbon-oxygen reaction in molten iron. *Metallurgical and Materials Transactions B*, 3:713–722, 1972.